

South Dakota State University

# Open PRAIRIE: Open Public Research Access Institutional Repository and Information Exchange

---

Electronic Theses and Dissertations

---

2016

## Nanoscale Study of Perovskite Solar Cells for Efficient Charge Transport

Nirmal Adhikari  
*South Dakota State University*

Follow this and additional works at: <https://openprairie.sdstate.edu/etd>



Part of the [Electrical and Computer Engineering Commons](#)

---

### Recommended Citation

Adhikari, Nirmal, "Nanoscale Study of Perovskite Solar Cells for Efficient Charge Transport" (2016). *Electronic Theses and Dissertations*. 1029.  
<https://openprairie.sdstate.edu/etd/1029>

This Dissertation - Open Access is brought to you for free and open access by Open PRAIRIE: Open Public Research Access Institutional Repository and Information Exchange. It has been accepted for inclusion in Electronic Theses and Dissertations by an authorized administrator of Open PRAIRIE: Open Public Research Access Institutional Repository and Information Exchange. For more information, please contact [michael.biondo@sdstate.edu](mailto:michael.biondo@sdstate.edu).

NANOSCALE STUDY OF PEROVSKITE SOLAR CELLS FOR EFFICIENT  
CHARGE TRANSPORT

BY

NIRMAL ADHIKARI

A dissertation submitted in partial fulfillment of the requirements for the

Doctor of Philosophy

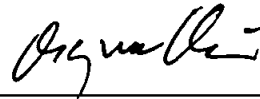
Major in Electrical Engineering

South Dakota State University

2016

NANOSCALE STUDY OF PEROVSKITE SOLAR CELLS FOR EFFICIENT  
CHARGE TRANSPORT

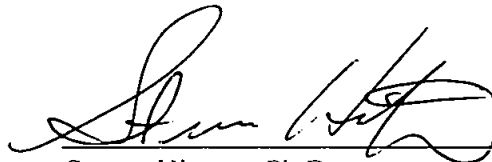
This dissertation is approved as a credible and independent investigation by a candidate for the Doctor of Philosophy in Electrical Engineering and is acceptable for meeting the dissertation requirements for this degree. Acceptance of this dissertation does not imply that the conclusions reached by the candidate are necessarily the conclusions of the major department.



Qiquan Qiao, Ph.D.  
Dissertation Advisor

8/12/16

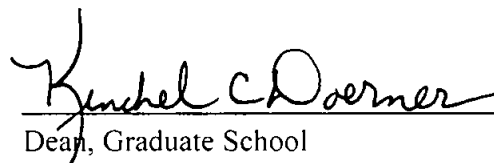
Date



Steven Hietpas, Ph.D.  
Head, Department of Electrical  
Engineering and Computer Science

8/12/16

Date



Dean, Graduate School

12 Aug 2016

Date

## ACKNOWLEDGEMENTS

The work presented in this dissertation was benefited from the grants including NASA EPSCoR (NNX13AD31A and NNX15AM83A), Pakistan-US Science and Technology Cooperation Program, and NSF MRI (grant no. 1229577 and 1428992), EE PhD program by the State of South Dakota.

I would like to express my sincere gratitude to Dr. Qiquan Qiao and Dr. David Galipeau for giving me an opportunity to work as a graduate research assistant at the Center for Advanced Photovoltaics, South Dakota State University. Dr. Qiao's guidance and encouragement have been crucial throughout the course of my research work and in improving the quality of this dissertation.

I would also like to thank Dr. Parashu Kharel, Dr. Zhengtao Zhu and Dr. Cody Wright, my dissertation committee members, for their time and consideration on reviewing my dissertation. Special thanks to Ashish Dubey, Swaminathan Venkatesan, Hytham Elbahy, Devendra Khatiwada, Bjorn Vagensmith, Khan Mamun Reza, Behzad Bahrami, Md Hasan Nazmul, Sally Mabrouk, Sudhan Sigdel, Abu Mitul and all my group members for support and encouragement during research period.

Finally, I would like to thank my family and friends for their love and support. To my lovely wife Shailu, who inspired me and provided constant encouragement during the entire process, as well as continuously proof reading my document.

## TABLE OF CONTENTS

LIST OF FIGURES .....	viii
LIST OF TABLES .....	xiv
ABSTRACT .....	xvi
Chapter 1 Introduction .....	1
1.1 Background .....	1
1.2 Previous work .....	9
1.3 Motivation .....	19
1.4 Objective .....	19
Chapter 2 Theory .....	21
2.0 Theory of Solar Cells .....	21
2.1 Silicon Solar Cells .....	21
2.2 Electrical Model of Solar Cells .....	25
2.3 Solar Cell Parameters .....	26
2.4 External Quantum Efficiency .....	27
2.5 Perovskite Solar Cells .....	28
2.6 Device Structures and Working Principle of Perovskite Solar Cells .....	29
2.7 Operating Principles of Characterization Techniques .....	31
2.7.1 Atomic Force Microscopy .....	31
2.7.2 Kelvin Probe Force Microscopy .....	33

2.7.3 X-ray Diffraction .....	37
2.7.4 Transient Photoconductivity Spectroscopy .....	39
2.7.5 Transient Photovoltage Spectroscopy .....	39
2.7.6 Transient Photocurrent Spectroscopy .....	40
Chapter 3 Experimental Procedures.....	43
3.1 Materials .....	43
3.2 Fabrication of Perovskite Solar Cells.....	43
3.2.1 One Step Deposition Method .....	44
3.2.2 Sequential Deposition Method .....	45
3.2.3 TiO <sub>2</sub> -Perovskite Interface .....	46
3.3 Materials Characterizations .....	46
3.3.1 UV-Vis Absorption Spectra.....	46
3.3.2 XRD Spectrum .....	47
3.3.3 Atomic Force Microscopy .....	48
3.3.3 Kelvin Probe Force Microscopy.....	49
3.3.4 Current Sensing Atomic Force Microscopy .....	51
3.4 Device Characterization.....	51
3.4.1 Current Density vs Voltage (J-V) Measurements.....	51
3.4.2 External Quantum Efficiency Measurements.....	52
3.4.3 Transient Photocurrent/Photovoltage Spectroscopy.....	55

Chapter 4: Results and Analysis .....	58
4.1 Effect of Temperature on Performance of Perovskite Solar Cell prepared from Single Step and Sequential Deposition Method .....	58
4.1.1 XRD Spectra of Perovskite films annealed at 100°C for different time.....	58
4.1.2 SEM images of Perovskite film prepared from Single Step and Sequential Deposition Method .....	60
4.1.3 Topography and KPFM images of TiO <sub>2</sub> -Perovskite interface Single Step Method.....	61
4.1.4 Surface Potential distribution of Perovskite film from Single Step Method ....	65
4.1.5 Topography and KPFM images of perovskite film from sequential deposition method .....	67
4.1.6 Recombination mechanism between Perovskite-TiO <sub>2</sub> interface .....	70
4.1.7 Topography and KPFM images of TiO <sub>2</sub> - Perovskite interface Sequential Deposition Method .....	71
4.1.8 Current Voltage curve of Sequential Deposition and Single Step Method .....	74
4.1.9 Charge carrier life time, charge transport time and total charge carrier density of Perovskite solar cell from Sequential Deposition Method.....	78
4.2 Effect of adding water in CH <sub>3</sub> NH <sub>3</sub> I solution for the preparation of Perovskite Solar Cell from Sequential Deposition Method .....	81
4.2.1 UV-Vis spectra of annealed Perovskite films.....	81
4.2.2 SEM images of Perovskite film.....	83

4.2.3 XRD spectra of annealed Perovskite films.....	84
4.2.4 XRD pattern of unannealed Perovskite films.....	87
4.2.5 AFM topographic images of annealed Perovskite films .....	89
4.2.6 AFM topographic images of unannealed Perovskite film.....	92
4.2.7 Surface potential distribution of annealed Perovskite film .....	94
4.2.8 Current density-voltage (J-V) curves of Perovskite Solar Cells.....	97
4.2.9 Charge carrier lifetime and charge transport time .....	100
4.3 Effect of humidity on the performance of Perovskite Solar Cells .....	103
4.3.1 UV-VIS spectrum of Perovskite film.....	103
4.3.2 XRD spectrum of Perovskite film .....	105
4.3.3 Topography and KPFM images of Perovskite film.....	107
4.3.4 Surface potential line profile of Perovskite film .....	109
4.3.5 Current sensing AFM imaging of Perovskite film .....	110
4.3.6 Current density-voltage (J-V) curves of Perovskite Solar Cells.....	112
4.3.7 Grain boundary model of perovskite solar cells.....	115
4.3.8 Transient photoconductivity measurement.....	116
Chapter 5 Summary and Conclusions.....	118
5.1 Summary .....	118
5.2 Conclusions .....	121
References.....	123



## LIST OF FIGURES

Figure 1.1 Efficiency evolution of perovskite solar cells from 2006 to 2016. ....	4
Figure 2.1 Light illumination for photoexcitation in silicon[74].....	21
Figure 2.2 Photoexcited charge carriers in valence and conduction bands of silicon[74].....	22
Figure 2.3 Band diagram of a p-n junction (modified from reference [75]).....	24
Figure 2.4 Equivalent circuit of solar cells with parasitic resistance.....	25
Figure 2.5 Illuminated J-V and power curve of typical solar cells.....	26
Figure 2.6 Crystal structure of perovskite structure $ABX_3$ .....	28
Figure 2.7 (a) n-i-p (b) p-i-n Perovskite solar cell structures .....	29
Figure 2.8 Energy band diagram of n-i-p Perovskite solar cell structure .....	30
Figure 2.9 Schematic of an atomic force microscopy.....	32
Figure 2.10 Force vs distance curve between tip and sample [81] .....	33
Figure 2.11 Electronic energy levels of the sample and AFM tip (a) tip and sample with separation d (b) tip and sample with electrical contact (c) tip and sample with external dc bias. ....	35
Figure 2.12 Schematic of KPFM measurements[85].....	37
Figure 2.13 Schematic of X ray diffraction from sample .....	38
Figure 2.14 (a) Schematic of transient photovoltage (TPV) measurement and (b) TPV decay .....	40
Figure 2.15 (a) Schematic of transient photocurrent and (b) transient photocurrent decay .....	41

Figure 3.1 Schematic of UV-VIS spectroscopy.....	47
Figure 3.2 Picture showing X-ray diffractometer located in DEH 056 lab .....	48
Figure 3.3 Picture of atomic force microscope located in DEH 053 lab .....	49
Figure 3.4 Schematic of JV measurement setup.....	52
Figure 3.5 Schematic of external quantum efficiency measurements .....	54
Figure 3.6 Picture of EQE measurement setup located in DEH 011 Lab.....	54
Figure 3.7 Schematic diagram of transient photoconductivity measurement system.....	56
Figure 4.1 XRD spectra of perovskite films annealed at 100°C for different time prepared by (a) single step and (b) sequential deposition method, respectively.....	59
Figure 4. 2 SEM images of perovskite films from single step method (a) un-annealing, (b) 15 min and from sequential deposition method (c) un-annealing, and (d) 15 min annealing at 100°C. ....	61
Figure 4.3 (a-d) 2D topography and (e-h) 2D surface potential of the perovskite-TiO <sub>2</sub> interface by depositing perovskite films on TiO <sub>2</sub> layer from single step method with un-annealing and annealing for 15 min, 30 min, and 60 min at 100°C. ....	62
Figure 4.4 Surface potential line profiles across the perovskite-TiO <sub>2</sub> interface from single step method for (a) un-annealing, (b) 15 min, (c) 30 min, and (d) 60 min annealing at 100°C. ....	63
Figure 4.5 Surface potential distribution of perovskite films prepared by single step method at different conditions of unannealing and annealing at 100°C for 15 min, 30 min, and 60 min. ....	65

Figure 4.6 (a-d) 2D topography and (e-h) 2D surface potential images of perovskite films prepared by single step method at different conditions of unannealing and annealing at 100°C for 15 min, 30 min, and 60 min. ....	66
Figure 4.7 (a-d) 2D topography and (e-h) 2D surface potential images of perovskite films prepared by sequential deposition method at different conditions of unannealing and annealing at 100°C for 15 min, 30 min, and 60 min.....	69
Figure 4. 8 Formation of PbI <sub>2</sub> prevents back recombination between electrons from TiO <sub>2</sub> and holes from perovskite. ....	71
Figure 4.9 (a-d) 2D surface potential mapping and (e-h) surface potential line profile of the perovskite-TiO <sub>2</sub> interface by depositing Perovskite films on TiO <sub>2</sub> layer from sequential deposition method with un-annealing and annealing for 15 min, 30 min, and 60 min at 100°C.....	73
Figure 4.10 J-V characteristics of perovskite solar cells with and without annealing of absorber layer from sequential deposition method in forward scan. ....	75
Figure 4.11 J-V characteristics of Perovskite solar cell with and without annealing of absorber layer from single step method (a) forward scan (b) forward and reverse scan for pervoskite solar cells prepared from annealing at 100°C for 15 min .....	77
Figure 4.12 (a) Transient photovoltage decay and (b) transient photocurrent decay of Perovskite solar cells from sequential deposition method. The values in the parenthesis show charge carrier lifetime and charge carrier transport time obtained by fitting the decay function with mono-exponential equation with fitting error less than 10 <sup>-7</sup> sec in (a) open circuit condition and (b) short circuit condition. ....	79

Figure 4.13 (a) Intensity dependence and (b) charge carrier density dependence life time in perovskite solar cells for different annealing time (15, 30 and 60 min) from sequential deposition method.....	81
Figure 4.14 UV-Vis spectra of annealed perovskite films prepared from 0%, 1%, 3%, 5%, and 7% water in MAI solution, respectively.....	82
Figure 4.15 SEM images of Perovskite film prepared from 0%, 1%, 3%, 5% and 7% water in MAI solution from sequential deposition method .....	83
Figure 4.16 XRD spectra of annealed perovskite films prepared from 0%, 1%, 3%, 5%, and 7% water in the MAI solution .....	86
Figure 4.17 XRD pattern of unannealed perovskite films prepared from 0%, 1%, 3%, 5%, and 7% water in MAI solution .....	88
Figure 4.18 AFM images of annealed Perovskite films prepared from (a) 0%, (b) 1%, (c) 3%, (d) 5%, and (e) 7% water in the MAI solution; and (f) average particle size vs water concentration. ....	90
Figure 4.19 Topography line profile of annealed perovskite film prepared from 0% and 5% water in MAI solution from sequential deposition method .....	91
Figure 4.20 (a) – (e) AFM images of unannealed perovskite films prepared from 0%, 1%, 3%, 5% and 7% water in the MAI solution, (f) average particle size vs water concentration in the MAI solution. ....	93
Figure 4. 21 Topography line profile of unannealed perovskite film prepared from 0% and 5% water in MAI solution from sequential deposition method .....	94
Figure 4.22 Nanoscale surface potential distribution of perovskite films prepared from 0%, 1%, 3%, 5%, and 7% water in the MAI solution.....	95

Figure 4.23 Surface potential images of perovskite films prepared from 0%, 1%, 3%, 5% and 7% water in MAI solution from sequential deposition method. ....	96
Figure 4.24 Current density-voltage (J-V) characteristics of annealed perovskite solar cells prepared from 0%, 1%, 3%, 5%, and 7% water in the MAI solution .....	97
Figure 4.25 JV curves of perovskite solar cells prepared from 0%, 1%, 3%, 5% and 7% water in MAI solution in forward and reverse scan from sequential deposition method.....	99
Figure 4.26 Transient photocurrent of annealed perovskite solar cells prepared from 0%, 1%, 3%, 5% and 7% water in the MAI solution.....	101
Figure 4. 27 Transient photovoltage of annealed perovskite solar cells prepared from 0%, 1%, 3%, 5% and 7% water in the MAI solution.....	102
Figure 4.28 UV-VIS spectrum of perovskite film inside the glove box (0% RH) and exposed to 25%, 45%, 55%, 65% and 75% RH for 5 hrs.....	104
Figure 4.29 XRD spectrum of perovskite film inside the glove box and exposed to 25%, 45%, 55%, 65% and 75% RH for 5 hrs.....	106
Figure 4.30 AFM topography (a - f) and surface potential images (g - l) of perovskite films inside the glove box (a & g) and exposed to 25% (b &h), 45% (c &i), 55% (d &j), 65% (e &f) and 75% (f&k) RH for 5 hrs, respectively.....	108
Figure 4.31 . Surface potential line scanning of Perovskite film (a) inside the glove box and exposed to (b) 25%, (c) 45%, (d) 55%, (e) 65% RH and (f) 75% RH for 5 hrs .....	110
Figure 4.32 CS-AFM imaging of perovskite film (a) inside the glove box and exposed to (b) 25 %, (c) 45 %, (d) 55 %, (e) 65 % RH for 5 hrs; and (f) 75 % RH.....	111

Figure 4.33 Current density-voltage (J-V) characteristics of perovskite solar cells prepared from perovskite film inside the glove box and exposed to 45%, 55%, 65% and 75% RH for 5 hrs .....	113
Figure 4.34 Schematic diagram of nanoscale potential distribution around grain boundary in Perovskite solar cell.....	115
Figure 4.35 Transient photocurrent decay of perovskite solar cells prepared from perovskite film inside the glove box and exposed to 45%, 55%, 65% and 75% RH for 5 hrs. ....	117

## LIST OF TABLES

Table 3.1 Materials used as different layers in perovskite solar cells. ....	43
Table 4.1 Energetic barriers for back recombination between holes in perovskite layer and electrons in ETL layer measured by KPFM. The films were prepared from single step method annealed at 100°C for different time.....	64
Table 4.2 Average grain boundary potential of perovskite films prepared from sequential deposition method annealed at 100°C for different time. ....	70
Table 4.3 Energetic barriers for back recombination between holes in perovskite layer and electrons in ETL layer measured by KPFM. The films were prepared from sequential method annealed at 100°C for different time. ....	74
Table 4.4 Photovoltaic parameters of the perovskite solar cells annealed at 100°C for different time of 15 min, 30 min and 60 min respectively from sequential deposition method.....	76
Table 4.5 Photovoltaic parameters of the perovskite solar cells annealed at 100°C for different time from single step method.....	78
Table 4.6 Full width half maximum (FWHM) and peak intensity of annealed perovskite films prepared from 0%, 1%, 3%, 5%, and 7% water in the MAI solution obtained from XRD spectra. ....	87
Table 4.7 Full width half maximum (FWHM) and peak intensity of unannealed perovskite films prepared from 0%, 1%, 3%, 5% and 7% water in the MAI solution obtained from XRD.....	89
Table 4.8 Photovoltaic parameters for annealed perovskite solar cells made under different concentration of water in the MAI solution.....	100

Table 4.9 Charge transport time for annealed perovskite solar cells made under different concentration of water in the MAI solution. ....	102
Table 4.10 Charge transport time for annealed perovskite solar cells made under .....	103
Table 4.11 Photovoltaic parameters for perovskite solar cells exposed to different humidity .....	114
Table 4.12 Dopant density and density of charged trap states of Perovskite film inside the glove box and exposed to 45% and 65% for 5 hrs .....	116



ABSTRACT

NANOSCALE STUDY OF PEROVSKITE SOLAR CELLS FOR EFFICIENT  
CHARGE TRANSPORT

NIRMAL ADHIKARI

2016

The effect of temperature, humidity and water on the grain boundary potential and charge transport within the grains of perovskite films prepared by sequential deposition technique. Grain boundary potential of perovskite films exhibited variation in electrical properties with humidity level, temperature and water concentration in methyl ammonium iodide solution. X-ray diffraction (XRD) indicates the formation of  $\text{PbI}_2$  phase in perovskite film with increasing temperature, humidity and adding larger quantity of water in methyl ammonium iodide solution. It is found that optimum amount of lead iodide helps for the passivation of perovskite film. Spatial mapping of surface potential in the perovskite film exhibits higher positive potential at grain boundaries compared to the surface of the grains. Back recombination barrier between  $\text{TiO}_2$ - perovskite increases to 378 meV for perovskite film annealed at 100 °C for 15 min. Grain boundary potential barrier were found to increase from ~35 meV to 80 meV for perovskite film exposed to 75% RH level compared to perovskite film kept inside glove box. Optimum amount of water which increases the solar cell performance by increasing the crystallinity of perovskite film was found to be 5% by volume of IPA. Results show strong correlation between temperature, humidity level, electronic grain boundary properties and device performance of perovskite solar cells.

## Chapter 1 Introduction

### 1.1 Background

Humanity has already faced consequences of wide use of non-renewable natural resources such as coal, oil, etc. Global warming and ozone depletion, caused by the emission of greenhouse gases during burning of fossil fuels, as well as air pollution and soil erosions, are only several examples of irreversible changes in the environment. This clearly highlights the need of a pollution free, renewable source of energy to minimize the adverse impacts to the earth, likely in the near future. Some renewable energy sources such as wind, hydro, biomass, geothermal, and solar are replacing the conventional fossil fuel technology. However, these resources have certain limitations such as low wind strength, increase in methane gas, which is harmful to the ozone layer. So the search for more environmentally friendly, sustainable and inexpensive renewable energy has led researchers and the industry interest towards photovoltaic solar energy.

The total solar energy reaching to the surface of the earth per year is estimated to be about 6700 times the annual world primary energy consumption. Therefore, harvesting the energy supplied by sun in easy means is a key approach to produce sustainable energy. Photovoltaic (PV) technology that converts solar energy to electricity will be an effective way for clean energy production. The advantages of photovoltaics over conventional fossil fuels are non-polluting, low maintenance cost. Solar panels can be placed with loads reducing the transmission loss. It can also be placed to those areas where national grid are unavailable such as hilly regions in developing countries.

Generally solar cell can be classified as (i) first generation solar cells (mono crystalline and poly crystalline silicon), (ii) second generation solar cells [amorphous

silicon (a-Si), microcrystalline silicon, copper indium gallium selenide (CIGS), and cadmium telluride (CdTe)] and (iii) third generation solar cells (polymer solar cells, oligomers, dye synthesized solar cells (DSCs), and organic/inorganic hybrid perovskite solar cells). The silicon solar cell has huge market which is over 95% of all the solar cells produced worldwide. The disadvantage of a-Si, and CIGS or CdTe solar cells are light induced degradation. They are also not earth abundant materials. These limitations have prevented these technologies to compete with c-Si solar cells. However, c-Si cell technology requires high temperature and high vacuum processes which are costly. Also, c-Si requires a few hundred microns thick film to absorb sufficient light due to its relatively poor light absorbance.

Unlike silicon solar cells, perovskite solar cells are solution processable with material diversity, abundance and large scale manufacturing. In addition, they have advantages including mechanical flexibility, light weight, low material consumption, semi-transparency, color tuning and less toxicity. However, poor stability of perovskite solar cells to temperature and moisture has made its major limitations. To overcome these limitations, different groups have studied the role of moisture and temperature on the performance of perovskite solar cells.

Perovskites are any material with the same type of crystal structure as calcium titanium oxide (CaTiO<sub>3</sub>), known as the perovskite structure, or  $X^{II}A^{2+}VI B^{4+}X^2$  with the oxygen in the face centers. Later, organo-metallic halides with a formula of ABX<sub>3</sub>, where A is an organic cation, B is a metal cation and X is a halide atom is being widely studied for photovoltaic applications. Single halide methylammonium lead triiodide (MAPbI<sub>3</sub>, CH<sub>3</sub>NH<sub>3</sub>PbI<sub>3</sub>) is the most widely studied perovskite composition. However, doping of

other non-iodine halides (Cl, Br) in MAPbI<sub>3</sub> perovskite has been reported to obtain mixed halide perovskite with much improved properties. In addition to widely used methylammonium (MA), other organic cations such as formamidinium (FA) and phenylammonium (PhA) have also been explored in perovskite. Methylammonium lead iodide perovskite is attracting immense interest in the field of photovoltaics as a promising material for achieving optimum standard for PV technology. It is simple to process with outstanding optoelectronic properties. Perovskite materials have advantages including broad spectrum light absorption and low-cost solution processing [5-8]. Perovskite absorber layer is a direct band gap semiconductor with large absorption coefficient ( $5.7 \times 10^4 \text{ cm}^{-1}$  at 600 nm), high carrier mobility, long range ambipolar charge carrier diffusion length, low exciton binding energy and high dielectric constant. These properties make perovskite a prospective candidate for the fabrication of highly efficient solar cells [9]. Figure 1.1 shows the efficiency evolution of state-of-the-art perovskite solar cells from 2006 to 2016. The current record PCE of 22.1% was obtained for single junction perovskite solar cells[1] . The carrier pathways in perovskite solar cells can be manipulated by controlling perovskite thin films, electron transport layer (ETL), hole transport layer (HTL) and their interfaces. Perovskite solar cells can be made in both planar and bulk hetero interface structures with high performance. More study has been done to find the best device structure in terms of robustness and stability. Therefore, deeper understanding of the electrostatic potential within the device can guide device optimization [2, 3].

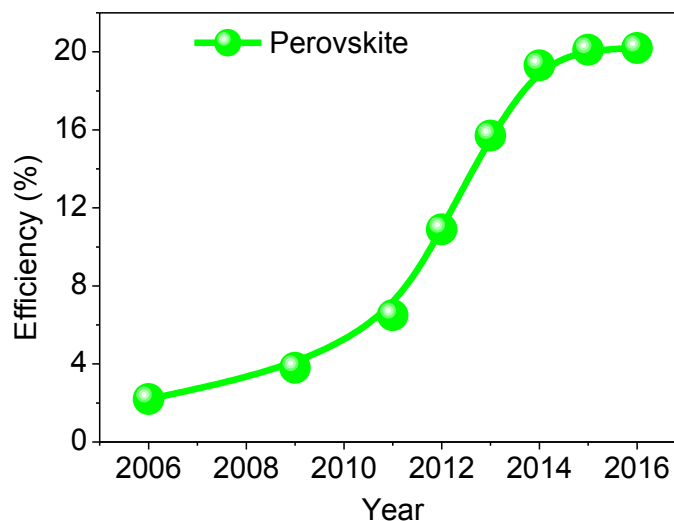


Figure 1.1 Efficiency evolution of perovskite solar cells from 2006 to 2016.

Moreover, electrons need to transfer from perovskite to ETL, while holes transfer to HTL without any significant energy loss for achieving high performance solar cells [2]. Kelvin probe force microscopy (KPFM) is a method to determine interface energetics, which can be used for fundamental understanding to select ETL and HTL for high performance devices. Grain boundaries and grains play a critical role for Perovskite solar cell performance. Grain boundary in copper indium gallium selenide (CIGS), copper-zinc-tin-sulfur/selenium (CZTS/Se) and cadmium telluride (CdTe) solar cells has been found an important factor for high efficiency. Electric field developed near grain boundaries separates the charges and enhances the collection of minority carriers i.e. electrons in p-type absorbing materials. Furthermore holes are repelled and thus the recombination at grain boundary is suppressed. Photogenerated electrons are attracted towards grain boundaries, transferred to the ETL, and finally collected to the end electrode enhancing short circuit current density of the device [3]. The density of states

(DOS) analysis shows that GBs do not generate any deep level trap states in the bandgap of perovskite solar cells making grain boundary properties benign [4].

Previous study shows that contact potential difference (CPD) of GBs in perovskite films is higher than within the grains and decreases after illumination. In addition, GB potential can be controlled through passivation [5, 6]. Recent study has shown that GBs play a beneficial role and has higher surface potential along GBs [7]. It has also been demonstrated from the current sensing – atomic force microscopy (CS-AFM) measurement that higher short circuit current is collected near GBs compared to interior grains. However, the effect on photogenerated charges at the perovskite-ETL interface and at GBs with annealing conditions remains unclear, which is one of the critical parameters to minimize carrier recombination.

There are different perovskite film preparation and crystallization methods [8-12]. These include vapor-assisted solution processing (VASP), physical vapor deposition (PVD), single step method and sequential deposition method [8, 13-16]. It had shown power conversion efficiency (PCE) exceeding 20% recently [17] and outperform other solar cells based on DSCs [16, 18-21], small molecules [22-24] and polymer solar cells [23, 25-30]. Among solution processed methods, single-step deposition of the perovskite film uses a mixture of  $\text{PbX}_2$  and  $\text{CH}_3\text{NH}_3\text{X}$  ( $\text{X} = \text{Cl}, \text{Br}$  or  $\text{I}$ ) from a common solvent such as  $\gamma$ -butyrolactone, dimethylformamide (DMF) or dimethylsulphoxide (DMSO). This method results in poor surface coverage and uncontrolled morphological variations which led to low photovoltaic performance. Therefore, sequential deposition method was developed to gain a better control of crystal formation and growth mechanism of perovskite phase [31]. In this method, lead iodide ( $\text{PbI}_2$ ) is first deposited by spin coating

from dimethylformamide onto a mesoporous TiO<sub>2</sub> film and then dipped in a solution of methyl ammonium iodide (MAI) (CH<sub>3</sub>NH<sub>3</sub>I) in isopropanol which led to the formation of the perovskite film penetrating the mesoporous TiO<sub>2</sub> film. However, the morphology of the perovskite film depends upon the reaction kinetics between PbI<sub>2</sub> and CH<sub>3</sub>NH<sub>3</sub>I while crystallization of perovskite happens simultaneously [10, 29]. Local concentration of MAI, crystallization temperature and pre-wetting have a great impact on the perovskite crystal size, which can be used to control the grain size and roughness of the perovskite film prepared from sequential method.

The morphology of the perovskite film is one of the critical factors for device performance [32, 33]. The perovskite morphology can be changed using additives or post treatment by exposing perovskite film in moisture and controlling the reaction kinetics between lead iodide and methyl ammonium iodide. It was reported that water molecules with controlled humidity during the fabrication of the perovskite films assist the growth of a larger grain with less defect density for higher device performance [34-40]. However, there are also reports which show that water molecules are detrimental to perovskite films. Water dissociates perovskite (CH<sub>3</sub>NH<sub>3</sub>PbI<sub>3</sub>) into lead iodide and methyl ammonium iodide which decreases the photovoltaic performance [2, 41]. Therefore, water is an important factor in perovskite film formation with dual roles. Depending on the amount of water molecules, they can assist growth, but also can cause degradation in the perovskite phase. It is necessary to study the role of water molecules and find the optimal condition of water in perovskite film formation in order to further improve perovskite solar cell efficiency.

The commercial use of the organo lead halide perovskite based solar cell is challenging because of its poor stability with moisture despite its promising efficiency[42, 43]. Recently, a protective hole transport material (HTM) has been used to shield moisture from atmosphere to perovskite film to enhance stability [19, 44]. However, such a protective HTM depends upon its inherent properties such as permeability, hydrophobicity and molecular density. In addition, the use of protective layer has drawbacks such as interfacial defects and changes in interfacial atomic and electronic structures [45-47]. Therefore, the mechanism of degradation is critical to provide materials design principles and engineering strategies to achieve long-term stability.

The degradation mechanism is an issue to debate in the field of perovskite solar cells. To understand the effect of humidity, there are reports with post treatment of perovskite film by exposing in controlled humidity conditions [36, 40, 45, 48-50]. It was reported that moisture during the fabrication of the perovskite films assists the growth of a larger grain with less defect density for higher device performance. However, it is also reported that moisture dissociates  $\text{CH}_3\text{NH}_3\text{PbI}_3$  into lead iodide and methyl ammonium iodide which reduces photovoltaic performance [51, 52]. The presence of water further breaks down the methyl ammonium iodide into methylamine ( $\text{CH}_3\text{NH}_2$ ) and hydrogen iodide (HI), leading to the formation of  $\text{I}_2$ (solid) and  $\text{H}_2$ (gas) after exposure to ambient atmosphere (i.e. oxygen and sunlight)[53].

It was also suggested that water could penetrate into the perovskite along grain boundaries and that irreversible decomposition occurs when a grain boundary has completely converted in to the dihydrate [20]. The proposed hydration of grain



boundaries due to water induced from moisture is not fully understood and will benefit from nanoscale potential distribution (NPD) measurements when exposed to humidity. The SPM technique measures the change in surface potential due to the presence of hydrated phases and defects in perovskite films with high spatial resolution. A potential change indicates the presence of charged defects within the perovskite films [8, 9].

Generally, grain boundary is a defect in a semiconductor which separates two adjacent crystallites of the same crystal structure and chemical composition, but of different orientation and acts as a trap center for charge carrier recombination. Crystal defects and impurities in grain boundaries create localized energy states within the band gap. These mid band gap states act as a recombination centers and capture electrons and holes from bulk material and decrease illumination current density. There are reports that show grain boundary in Perovskite materials act as conduction paths for photo-generated electrons suppressing the recombination. However, others [50] have shown detrimental role of grain boundary reducing the PCE of the perovskite devices.

The factors that lead to high efficiency of perovskite solar cells include ultra-smooth film, large grain size, high crystallinity, perovskite layer thickness, precursor ratio, annealing temperature, and crystal growth. Optimization of all these parameters leads to change in perovskite electronic properties (e.g., charge carrier lifetime, trap states, charge transport time, etc.), which largely affects the performance of solar cells. These desirable properties have been obtained by optimizing processing conditions for perovskite deposition. A fundamental understanding of the physical behaviors in single and mixed halide perovskite is required and will provide a promising pathway to tune the material property in order to achieve highly efficient device performance.

## 1.2 Previous work

Photovoltaic effect was first reported by Alexandre Edmund Becquerel in 1839 where solar energy was directly converted to electricity by inserting an electrolyte between two metal electrodes [54]. The first crystalline silicon (c-Si) solar cell has efficiency of 6%. It was invented by Chapin et al. in 1954 at Bell Laboratories, [55] which was a critical achievement in solar photovoltaic technology. This efficiency was further improved to 12.4 % by increasing the purity of crystalline silicon in 1972 by Gereth et al. [56].

In 1976, amorphous-Si solar cell with a thickness of ~1 micron was developed with a PCE of 2.4% [24]. This type of solar cell has limitation of light induced degradation and decrease in dark conductivity and photoconductivity [9, 25]. Efficiencies of c-Si cells, multi-crystalline Si cells, and a-Si cells were improved to 25% by Sun power in 2014, 20.4% by Fraunhofer Institute of Solar Energies in 2004 and ~13.4% by LG electronics in 2013, respectively [11].

In 1986, the concept of donor-acceptor heterojunction bi-layer organic solar cell was reported by Tang with a PCE of 1% [57, 58]. The efficiency of bilayer polymer solar cell was low. Therefore, the concept of bulk heterojunction solar cell was first introduced by Yu et al. in 1995 [59]. Shaheen et al. in 2001 achieved PCE of 2.5% in bulk heterojunction solar cells [60]. By then, the efficiencies quickly reached to 9.2% and 10.6% for single junction by He et al. in 2012 and tandem structure by You et al. in 2013, respectively [61, 62].

In 1987, the concept of dye-sensitization was introduced by Moser with an experimental demonstration showing that photocurrent was slightly enhanced by dye-

sensitizing halogenated silver (Ag) plates. In 1991, Brian O'Regan and Michael Grätzel developed dye sensitized solar cells (DSCs) with an efficiency of 7.9% in simulated solar light and 12% PCE in diffused sunlight [63]. The breakthrough was seen in efficiency after the combination of the mesoporous titanium dioxide ( $\text{TiO}_2$ ) as photoanode material and the electrolyte containing iodide/triiodide redox shuttle.

In 2009, Miyasaka et al. reported the first perovskite solar cell with an efficiency of 3.8% [64-66]. In this structure, they replaced the dyes with perovskite absorber that has broader absorption, ambipolar charge transport and long carrier diffusion length [67]. Methylammonium lead iodide ( $\text{CH}_3\text{NH}_3\text{PbI}_3$ ) was used as perovskite absorber layer and iodide/triiodide as redox couple. This solar cell structure has stability issue due to dissolution of perovskite with liquid electrolyte.

In 2012, Kim et al. used spiro-MeOTAD and mesoporous (mp)- $\text{TiO}_2$  as the hole transport (HTM) and electron transport (ETM) materials and obtained a PCE of 9.7% for the first reported perovskite based solid-state mesoscopic heterojunction solar cell. This was an evolutionary jump which used perovskite as primary photo-absorber layer to prepare solid state meso-superstructured perovskite solar cells [68]. Before this solid state device, the  $\text{CH}_3\text{NH}_3\text{PbI}_3$  perovskite nanoparticles in liquid cells were unstable due to rapid dissolution in iodide-contained liquid electrolyte. They showed the long term stability of the device till 500 hours when exposed to ambient air without encapsulation.

In 2013, Lee et al. replaced mesoporous  $\text{TiO}_2$  with mesoporous Aluminum Oxide ( $\text{Al}_2\text{O}_3$ ) and achieved an efficiency of 10.9% [66].  $\text{Al}_2\text{O}_3$  is an insulator with a wide band gap (7 - 9 eV) and acts as a "scaffold" where a thin layer of perovskite absorber material is coated. They found that the charge transport time for electrons much faster in  $\text{Al}_2\text{O}_3$

than in n-type TiO<sub>2</sub>. The open circuit voltage was found to increase with insulating Al<sub>2</sub>O<sub>3</sub> scaffold by a few hundred millivolts under simulated AM1.5 solar irradiation. The limiting factor in efficiency of these devices was found to arise from misbalance between series and shunt resistances. The perovskite absorber has conductivity of 10<sup>-3</sup> S cm<sup>-3</sup> and causes short circuit between the silver electrode and the perovskite absorber through voids with a thin capping layer of p-type spiro-OMeTAD. However increasing the thickness of spiro-OMeTAD (conductivity~10<sup>-5</sup> S cm<sup>-1</sup>), resulted in high series resistance. Thus, a balance was needed between the adjacent layer thicknesses which lowered the efficiency.

In 2013, Smith et al. fabricated planar structured perovskite solar cells with vapor-deposited perovskite layer and obtained PCE over 15% with an open circuit voltage of 1.07 V without using any mesoporous layers [65]. The vapor-deposited films are extremely uniform, appear to be crystalline features on the length scale of hundreds of nanometers. In contrast, the solution-processed films appear to coat the substrate only partially, with crystalline ‘platelets’ on the length scale of tens of micrometers. The voids between the crystals in the solution-processed films appear to extend directly to the compact TiO<sub>2</sub>-coated FTO coated glass. However, this technique requires high vacuum that consumes high energy and hinders mass production.

At the end of 2013, the optimized device structures of meso-superstructured solar cell (MSSC) resulted PCE of 15.9% with short circuit current density (J<sub>sc</sub>) of 21.5 mA/Cm<sup>2</sup>, open circuit voltage (V<sub>oc</sub>) of 1.02 V and fill factor of 0.71. This was the highest reported efficiency in 2013. This fabrication was done using low temperature processing (<150 °C) of anatase TiO<sub>2</sub> with diameter < 5 nm to use as compact layer. The

conductivity of this TiO<sub>2</sub> was 100 times higher conductivity than that of conventional TiO<sub>2</sub> fabricated from high temperature route. The ensuing all-low-temperature processed MSSC outperform the previous state-of-the-art devices, delivering a maximum full sun PCE of 15.9 %.

In 2014, Yang et al. achieved an efficiency of 19.3% by fabricating perovskite solar cell under controlled humidity conditions ( $30 \pm 5\%$  relative humidity) with solution processing [69]. They fabricated perovskite film in controlled humidity and found a decrease in carrier recombination. They also modified the work function of the ITO and enhanced the carrier concentration by doping the TiO<sub>2</sub> electron transport layer. These changes produced a PCE of 19.3%.

In 2015, Yang et al. achieved an efficiency of 20.2 % using formamidinium lead iodide (FAPbI<sub>3</sub>) which has broad absorption compared to conventional methyl ammonium lead iodide [70]. In 2016, Saliba et al. showed a stabilized efficiency of 21.1% and 18% after 250 hours under standard operational conditions. They used mixture of Cs/MAPbI<sub>3</sub>/FAPbI<sub>3</sub> cation. It was shown that adding Cs to MAPbI<sub>3</sub>/FAPbI<sub>3</sub> suppressed the yellow phase impurities and induced uniform perovskite grains extending from the electron to the hole collecting layer consistent with seed-assisted crystal growth. These triple cation perovskites are also found to be more robust to subtle variations during the fabrication process. These devices were highly reproducible and PCEs more than 20% were obtained on a regular basis. Later the efficiency rose to 22.1% as shown in NREL char[1].

In 2012, Yin et al. showed from the first principle calculation that the grain boundaries in perovskite solar cells are benign in nature and help for charge transport [4].

However, others [50] have shown detrimental role of grain boundary reducing the PCE of the perovskite devices. Edri et al. reported higher work function at the GBs than within the grains with a small potential barrier reducing the charge transport within the grains [71]. Chen et al. reported that the grain boundary potential can be lowered from 50 mV to 30 mV by annealing the perovskite film [18]. Yun et al. reported the effect of illumination in contact potential difference (CPD) at the GBs and found that the CPD at GBs becomes higher than within grains at illumination and vice versa [19]. Kim et al. showed that the grain boundary potential is higher for  $\text{CH}_3\text{NH}_3\text{Pb}(\text{I}_{0.88},\text{Br}_{0.12})_3$  than  $\text{CH}_3\text{NH}_3\text{PbI}_3$  film by 100 mV [2].

In 2015, Yun et al. showed the beneficial role of organic-inorganic halide planar perovskite solar cells. They found that the photo-generated charge carriers are more efficiently separated and transported along grain boundaries. Similar results were also shown using cs-AFM where high current collection was found near grain boundary. On the basis of these results, they proposed that downward band bending was obtained at grain-grain boundary in perovskite film and subsequently transported photogenerated electrons along the grain boundary core [7].

In 2015, Li et al. performed the microscopic investigation of grain boundary in both typical and inverted organolead halide perovskite solar cells. They also found the downward band bending at the GBs and formed a lower barrier which attracted electron under illumination. They found major current flow through the grains and negligible current through grain boundary at 0V bias. However, when the bias overcame the barrier of the GBs, the photocurrents at the GBs became much higher than those of the grains. They demonstrated that the enhanced photoinduced electron collections at GBs.

Therefore, grain boundary acted as effective charge dissociation interfaces and photocurrent transduction pathways [72].

At the same time in 2015, Jiang et al. studied the ambipolar property (n-type or p-type) and the potential distribution across the device stack by monitoring the potentials in the cross-section of lead-based perovskite using nanoscale Kelvin Probe Force Microscopy (KPFM). The potential profiling obtained from KPFM images show that device physics of perovskite solar cells resembles that of the traditional inorganic polycrystalline PV devices, where a p-n junction is located at the TiO<sub>2</sub>/perovskite interface with free-carrier concentration of 10<sup>16</sup>-10<sup>17</sup> cm<sup>-3</sup> on both planar and porous devices [10].

In 2015, Wu et al. obtained 18% PCE by increasing the quality of the perovskite film. They found that the addition of small (2% by volume in PbI<sub>2</sub>/DMF solution) amount of water in PbI<sub>2</sub> affects the surface coverage of the PbI<sub>2</sub> and perovskite films prepared by sequential deposition method on PEDOT:PSS. The device performance of perovskite solar cells was found to increase from 0.0063 % to 18%. The PbI<sub>2</sub> film prepared from PbI<sub>2</sub>/DMF with 2 wt% water has smoothest film with largest grains. This high quality PbI<sub>2</sub> films gave compact and smoothest perovskite film when dipped in methyl ammonium iodide solution. This is due to the homogeneous precursor solution of PbI<sub>2</sub>/DFM by adding small amount of water. Since water is compatible with DMF, its polarity, dielectric constant and solubility parameter changes with addition of small amount of water. PbI<sub>2</sub> was totally dissolved in the mixed solvent as the solubility parameter of the DMF/H<sub>2</sub>O mixture is close to that of PbI<sub>2</sub>. This helped to obtain smooth

perovskite film without voids and gaps. They showed that the perovskite film prepared from 2% water in  $\text{PbI}_2/\text{DMF}$  has compact and largest grain size [33].

In 2015, Gong et al. controlled the crystallization of mixed halide perovskite film ( $\text{CH}_3\text{NH}_3\text{PbI}_{3-x}\text{Cl}_x$ ) using water as solvent additive for perovskite solution precursor. The crystallization of perovskite thin films with good coverage and film morphology was obtained by adding small amount (2%) of deionized water in DMF solution. The efficiency was increased from 12.13% to 16.06% by adding water as additives in DMF solution. They also found that the water doped devices were more stable in ambient conditions due to the formation of stable perovskite hydrates by incorporating the water additive during the solution process. They found the hydrated phase of  $\text{CH}_3\text{NH}_3\text{PbI}_{3-x}\text{Cl}_x \cdot n\text{H}_2\text{O}$  which resists the corrosion of perovskite film by water molecules to some limit. These hydrated phases were found to be generated during annealing process. The DMF-only based perovskite films shows many small pin holes and voids resulting in poor charge transport and weak light absorption in perovskite films. The increase in grain size and disappearance of voids were found using small amount of water as additive in DMF solution. The continuous perovskite film with less grain boundary area was found using 2%  $\text{H}_2\text{O}$  in DMF solution during perovskite film formation [34].

In 2015, Eperon et al. used controlled humidity to fabricate perovskite solar cells and showed increase in device performance. They used humidity-controlled chamber, with spincoater and hotplate inside. They used separate accurate humidity and temperature sensors and averaged them to measure humidity and temperature for particular fabrication. The high humidity condition was achieved by heating water bubbler to increase evaporation. The pressure was controlled by using arm-holes in the



chamber. Eperon et al. has shown the critical role of moisture exposure during metal halide perovskite thin film fabrication. Moisture exposure results in increase in performance of the perovskite solar cells due to increase in open-circuit voltage, photoluminescence and longer photoluminescence lifetimes. This is due to reduction in trap state density which may be due to the partial dissolution of the methylammonium component with water induced from moisture exposure [8].

In 2015, Christians et al. also observed the formation of a hydrated product after exposing  $\text{CH}_3\text{NH}_3\text{PbI}_3$  to moisture [47]. However, the XRD was not able to identify this phase. So, they synthesized  $(\text{CH}_3\text{NH}_3)_4\text{PbI}_6 \cdot 2\text{H}_2\text{O}$  compound and captured the video showing the formation of these hydrated phase in water. It was observed that the XRD pattern of this compound was similar to  $\text{CH}_3\text{NH}_3\text{PbI}_3$  film exposed to 90% RH for 7 days. The perovskite film exposed to 90% RH showed strong peaks at  $2\theta$  values of  $8.42^\circ$  and  $10.46^\circ$ . This gave a direct evident of formation of this intermediate hydrated compound when  $\text{CH}_3\text{NH}_3\text{PbI}_3$  was exposed to water. They also show that the charge carrier dynamics was not affected for short period due to formation of this hydrated phase however, significant decrease in absorption was found. The authors proposed that the formation of the hydrated compound depends on the relative strength of the hydrogen bonding interaction between cation ( $\text{CH}_3\text{NH}_3^+$ ) or  $\text{H}_2\text{O}$  with  $\text{PbI}_6$ . Therefore, strengthening the bond between the cation and metal halide can improve the degradation of perovskite film due to moisture [47].

In 2016, Yang et al. studied the effect of moisture with custom built humidity control setup to measure the decomposition rate of perovskite films. They used relative humidity (RH) controller instrument with precise flow controller. The saturated water

vapor was mixed with diluent carrier gas and its flow was controlled to achieve desired relative humidity. The actual humidity in the perovskite solar cell was monitored using RH sensor placed on custom built sample holder. In addition, this arrangement also provided a way to measure *in situ* UV-Vis absorbance during the decomposition of perovskite phases. They found that the hole transport layer played significant role to protect the underneath layer of perovskite from decomposition and enhanced device lifetimes and resistance to humidity. They found formation of a hydrated intermediate compound containing isolated  $\text{PbI}_6^{4-}$  octahedral as the first step in the decomposition process using *in situ* Grazing Incidence X-ray Diffraction (GIXRD). The degradation of perovskite film occurs extremely quickly for the 98% RH and the absorption was found to reduce to half of its original value just in 4 hours. However, when the film was exposed to lower RH (20%) value, the degradation of the perovskite film was estimated to be 10,000 hours by extrapolating the observed data. These results helped to understand the fundamental decomposition pathways in organolead halide perovskite films [73].

In summary, the charge transport in perovskite solar cells strongly depend on humidity and annealing conditions. Kelvin probe force microscopy (KPFM) is a method to study the nanoscale potential distribution along grain and grain boundaries. Cs-AFM in conjugation with kelvin probe force microscopy can be used to study the local charge transport properties in perovskite solar cells. Hence, KPFM determines interface energetics, which can be used for fundamental understanding to select electron transport layer (ETL) and hole transport layer (HTL) to suppress back recombination for high performance devices. Previous reports showed that contact potential difference (CPD) of GBs in perovskite films is higher than within the grains and decreases after illumination.

In addition, GB potential can be controlled through passivation. Recent study has shown that GBs played a beneficial role and had higher surface potential along GBs. It has also been demonstrated from the CS-AFM measurement that higher short circuit current is collected near GBs compared within interior grains. However, the effect on photogenerated charges at the perovskite-ETL interface and at GBs with annealing conditions remains unclear, which is one of the critical parameters to minimize carrier recombination.

Humidity also plays important role in perovskite solar cell fabrication. Therefore, water induced from moisture is considered as the main factor for the instability of perovskite film. Water molecules with controlled humidity during the fabrication of the perovskite film have been shown to assist in the growth of a larger grain with lower defect density, resulting in higher device performance. Water molecules can penetrate across the perovskite structure to form partly reactive phases [ $\text{CH}_3\text{NH}_3\text{PbI}_3 \cdot \text{H}_2\text{O}$  and  $(\text{CH}_3\text{NH}_3)_4\text{PbI}_6 \cdot 2\text{H}_2\text{O}$ ]. These reactive phases are metastable that then spontaneously dehydrates in air forming perovskite phases. Water can improve the growth of Perovskite films from the interaction between  $\text{H}_2\text{O}$  and  $\text{MAPbI}_3$ , such as hydrogen bonding interaction. However, there are also reports which show that water is detrimental to perovskite film which dissociates  $\text{CH}_3\text{NH}_3\text{PbI}_3$  into lead iodide ( $\text{PbI}_2$ ) and (MAI) methyl ammonium iodide ( $\text{CH}_3\text{NH}_3\text{I}$ ), diminishing photovoltaic performance. It is shown that water plays a dual role and helps to increase film crystallinity and quality (smooth and void free) when an optimum amount of water is added, and dissociates the perovskite if a higher content of water is used.

The commercial use of the organo lead halide perovskite based solar cell is challenging because of its poor stability with moisture despite its promising efficiency. The mechanism of degradation is critical to provide materials design principles and engineering strategies to achieve long-term stability. The degradation mechanism is an open debate in the field of perovskite solar cells. It is also suggested that water could penetrate into the perovskite along grain boundaries and irreversible decomposition occurs when a grain boundary has completely converted to the dihydrate perovskite phase. The proposed hydration of grain boundaries due to water induced from moisture is not fully understood and will benefit from nanoscale potential distribution (NPD) measurements when exposed to humidity. The SPM technique measures the change in surface potential due to the presence of hydrated phases and defects in perovskite films with high spatial resolution.

### 1.3 Motivation

There is a need to understand the role of annealing temperature, water and humidity on charge transport and device performance of perovskite solar cells

### 1.4 Objective

The objective of this work is to understand the effect of annealing temperature, water and humidity on charge transport and device performance of perovskite solar cells

The following tasks are performed to achieve the objective: (1) Study role of annealing conditions in perovskite solar cells to suppress charge carrier recombination (2) Improve crystallinity of perovskite film for high performance solar cells with addition of water in perovskite precursors and (3) Obtain grain boundary potential  $< 25$  meV for

efficient charge transport by exposing the perovskite film in varying humidity during fabrication.

## Chapter 2 Theory

### 2.0 Theory of Solar Cells

#### 2.1 Silicon Solar Cells

Semiconductor can be classified in to intrinsic (pure) or extrinsic (doped) types. Silicon is intrinsic by nature and is doped for solar cell applications. The number of excited electrons and holes are equal in intrinsic silicon (i-type). Crystallographic defects and excited electrons are the main factors for the electrical conduction in intrinsic semiconductor. The intrinsic semiconductor can be doped with either p-type or n-type material. The type of conductivity depends upon the dopant. In p-type conductivity the dopant produces extra vacancy and in n-type of conductivity the dopant produces extra electrons. Therefore in n-type silicon, electrons are the majority charge carriers while in p-type silicon holes are the majority carriers. Group V elements are used for n-type doping and group III elements are used for p-type doping [52, 53].

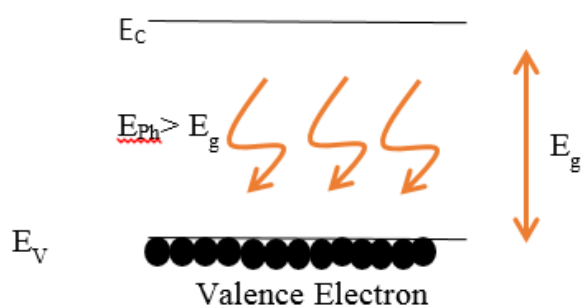


Figure 2.1 Light illumination for photoexcitation in silicon[74]

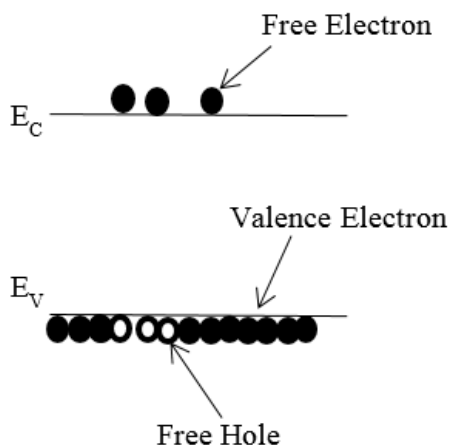


Figure 2.2 Photoexcited charge carriers in valence and conduction bands of silicon[74]

Crystalline silicon has a band gap of 1.1 eV corresponding to 1127 nm and absorbs all the wavelengths shorter than 1127 nm. When light is illuminated in silicon, the photons with energy larger than its band gap are absorbed by the material as shown in Figure 2.1 and 2.2. Silicon is a cheap and abundant material with less processing issue, therefore it is the most common materials for photovoltaic applications.

Figure 2.3 shows the energy band diagram of P-N junction exhibiting the formation of space charge region. When the n-type semiconductor material is in contact with p-type semiconductor. The concentration gradient is formed which diffuses electrons from n-type semiconductor to p-type semiconductor. Electrons diffuse from n-side to p-side and holes diffuse from p-side to n-side. The diffused electrons from the n-side recombine with holes from the p-side near the junction and holes from the p-side recombine with electrons from the n-side, thus forming a space charge region depleted of free carriers and consists of positive (n-side) and negative bound charges (p-side) on either side. This region is called depletion region or space charge region. These positive

and negative bound charges act as opposite charge in parallel plate capacitor and set up an electric field right at the junction between the n-type and p-type material. The direction of electric field is from n-side to p-side and accelerates the electron from p-type to n-type. Thus, the built in electric field causes some of the electrons and holes to flow in the opposite direction to the flow of carriers caused by diffusion. In the depletion region, bending of the conduction band and valence band occurs such that fermi energy levels of the n-side and p-side are aligned.

When photons are incident at the p- or n- type side, electrons from the valence side are excited to conduction band. These separated electrons and holes are swept towards cathode and anode by built in electric field and contribute to the electrical power.

The depletion width of the p-n junction is given by

$$W = \sqrt{\frac{2\varepsilon V_{bi}}{q} \left( \frac{1}{N_A} + \frac{1}{N_D} \right)} \quad 2.1$$

where  $\varepsilon$  is the dielectric permittivity of the semiconductor,  $q$  is the elementary charge having value of  $1.602 \times 10^{-19}$  C and  $V_{bi}$  is the built in potential between the quasi Fermi levels of p and n layers.

The free carriers will transport in the semiconductor before recombination. The average distance that the minority carriers travel through majority carriers before recombination is called diffusion length. The diffusion length for electrons in p-type and holes in n-type is given by

$$L_n = \sqrt{D_n \tau_n} \quad 2.2$$

$$L_p = \sqrt{D_p \tau_p} \quad 2.3$$



where  $D_n$  and  $D_p$  are diffusion coefficient for electron and hole, respectively;  $\tau_n$  and  $\tau_p$  are recombination lifetimes of electron and hole in p side and n side, respectively.

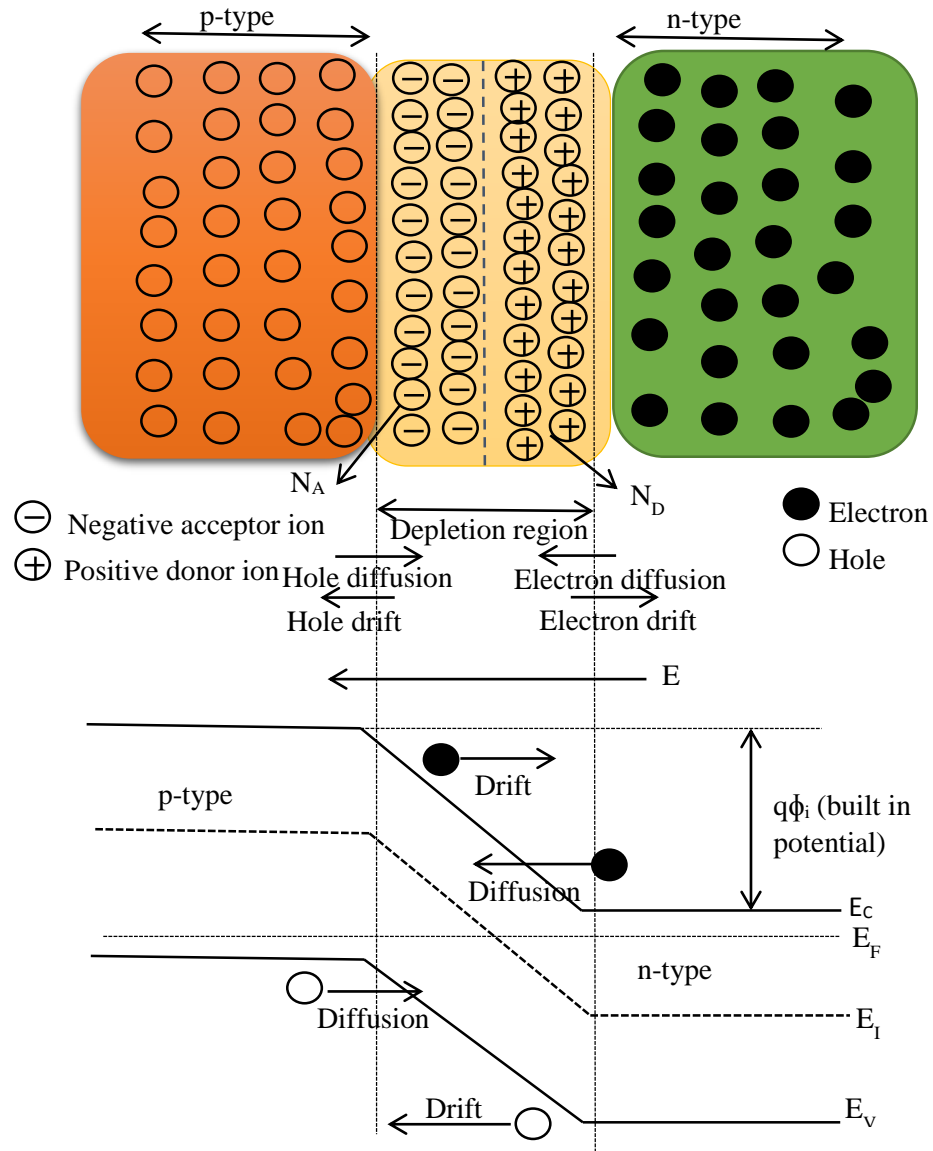


Figure 2.3 Band diagram of a p-n junction (modified from reference [75])

## 2.2 Electrical Model of Solar Cells

Figure 2.4 shows the equivalent diagram of solar cells with parasitic resistance. A solar cell can be modelled with a p-n junction diode having resistors in series ( $R_s$ ) and parallel ( $R_{sh}$ ).

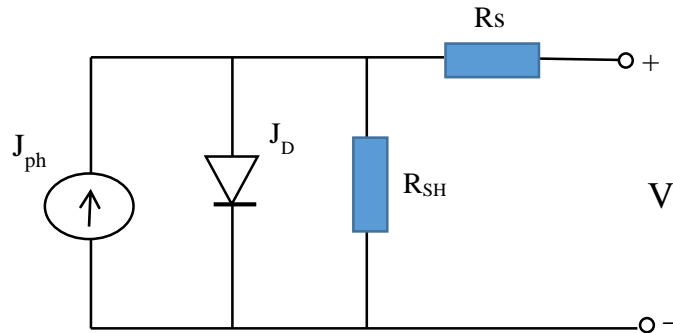


Figure 2.4 Equivalent circuit of solar cells with parasitic resistance

When an external load is connected to the solar cell, a potential difference ( $V$ ) develops across the load which drives the diode in forward bias and the current flows in the opposite direction of illuminated photocurrent ( $J_{ph}$ ). This reverse current gives rise to dark current,  $J_{dark}$ . In the dark, an ideal solar cell can be modeled by a diode and the dark (diode) current as [74],

$$J_{dark} = J_0 \left( e^{\frac{qV}{K_B T}} - 1 \right), \quad 2.4$$

where,  $J_0$  is reverse saturation current density,  $K_B$  is the Boltzmann's constant, and  $T$  is the absolute temperature.

The net current  $J(V)$  through the solar cell is

$$J(V) = J_{dark}(V) - J_{ph}, \quad 2.5$$

Solving equation 2.4 and 2.5,

$$J(V) = J_0 \left( e^{qV/K_B T} - 1 \right) - J_{ph}, \quad 2.6$$

The current through the solar cell is called short circuit current density ( $J_{sc}$ ) when load resistance is zero ( $V = 0$ ),

$$\text{At } V = 0, J = J_{sc} \quad 2.7$$

'V' across the load is maximum under open-circuit condition ( $J = 0$ ) and this voltage is called the open circuit voltage ( $V_{OC}$ ) of the solar cell, which is obtained after solving equation 2.6 as,

$$V_{OC} = \frac{KT}{q} \ln\left(\frac{J_{ph}}{J_0} + 1\right), \quad 2.8$$

### 2.3 Solar Cell Parameters

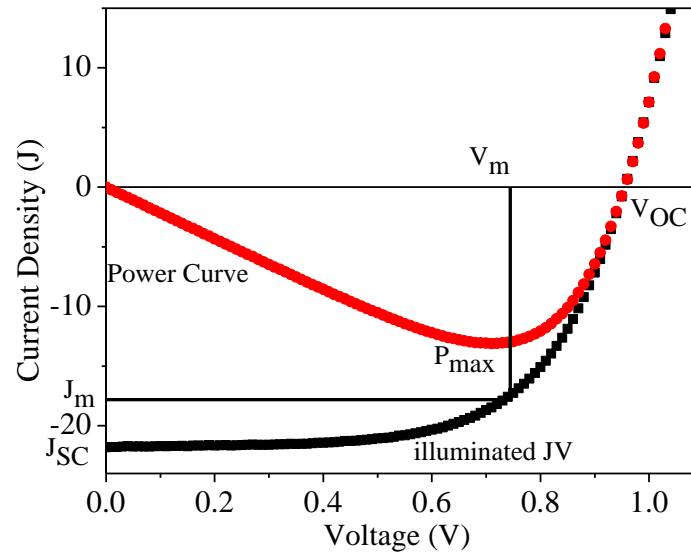


Figure 2.5 Illuminated J-V and power curve of typical solar cells

Figure 2.5 shows the JV curve and power curve of typical solar cells. The fill factor of the solar cell is defined as the ratio of maximum power to product of short circuit current density and open circuit voltage and is given by

$$FF = \frac{P_{max}}{J_{sc}V_{oc}}, \quad 2.9$$

Where maximum power is given by

$$P_{max} = J_M V_M, \quad 2.10$$

Therefore, fill factor can also be expressed as

$$FF = \frac{J_M V_M}{J_{sc} V_{oc}}, \quad 2.11$$

The efficiency of the solar cell is defined as the ratio of electrical output to optical input and is given by

$$\eta = \frac{P_{max}}{P_{in}}, \quad 2.12$$

#### 2.4 External Quantum Efficiency

External quantum efficiency of solar cell is defined as the ratio of number of charge carriers collected to the number of incident photon of a given energy in solar cells. The internal quantum efficiency (IQE, with respect to absorbed photons) of perovskite solar cells are affected by internal resistance, series resistance, recombination, back contact quality and surface states. But, the external quantum efficiency are mainly affected by reflection and external loss of photons [76].

$$EQE = \frac{\text{number of electrons collected}}{\text{number of incident photons}}, \quad 2.13$$

The  $J_{sc}$  is related to the incident light spectrum through EQE as,

$$J_{sc} = q \int b(E) \cdot EQE(E) \cdot dE, \quad 2.14$$

where,  $q$  is the electronic charge, and  $b(E)$  is the incident photon flux density which is the number of photons of energy between  $E$  and  $E+dE$  per unit area per second incident on the solar cell.

## 2.5 Perovskite Solar Cells

Perovskites are a family of materials with the crystal structure  $ABX_3$  of calcium titanate and named after Russian mineralogist L.A. Perovski (1792-1856) [46]. There are wide applications of this structure based on thermoelectric, insulating, semiconducting, piezoelectric, conducting, antiferromagnetic, and superconducting properties.  $ABX_3$  is the crystal structure of perovskite types of materials, where A and B are cations and X is an anion of different dimensions with A being larger than X [77]. The Crystal structure of perovskites is shown in Figure 2.6. In methylammonium based perovskite materials, A is organic cation methylammonium ( $CH_3NH_3^+$ ), Anion X is a halogen and B is a cation (Pb, Sn). Therefore, the standard compound methylammonium lead triiodide ( $CH_3NH_3PbI_3$ ), with mixed halides  $CH_3NH_3PbI_{3-x}Cl_x$  and  $CH_3NH_3PbI_{3-x}Br_x$  are being studied for solar cell applications. The perovskite solar cells is prepared by using single halide ( $CH_3NH_3PbI_3$ ) or mixed halide ( $CH_3NH_3PbI_{3-x}Cl_x$  and  $CH_3NH_3PbI_{3-x}Br_x$ ) in different structures i.e. n-i-p and p-i-n structures.

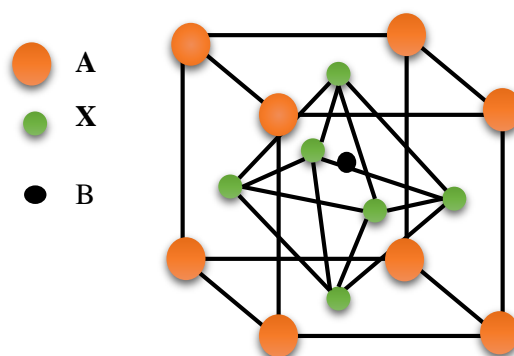


Figure 2.6 Crystal structure of perovskite structure  $ABX_3$

## 2.6 Device Structures and Working Principle of Perovskite Solar Cells

The functions of perovskite was considered to be similar to the dye in dye sensitized solar cell (DSSC) and was first employed as ‘sensitizers’ on mesoporous TiO<sub>2</sub> structures. Perovskite crystals absorbs the light and excites electrons in conduction band of TiO<sub>2</sub>. This electron is transported to the external circuit by electrode by solar cells. The holes remaining on the perovskite crystals are then transferred to a solid-state hole-conductor or a redox active electrolyte and subsequently transported out of the solar cell. Later on, it is reported that perovskite can work as ambipolar property and can transport both electron and holes and few hundred nanometer thick solid perovskite film can sustain charge generation and transport [78]. Figure 2.7a and 2.7b shows n-i-p and p-i-n structures where perovskite is sandwiched between p and n type materials. This simple architecture is applicable to a broad range of manufacturing approaches for commercializing this technology [79].

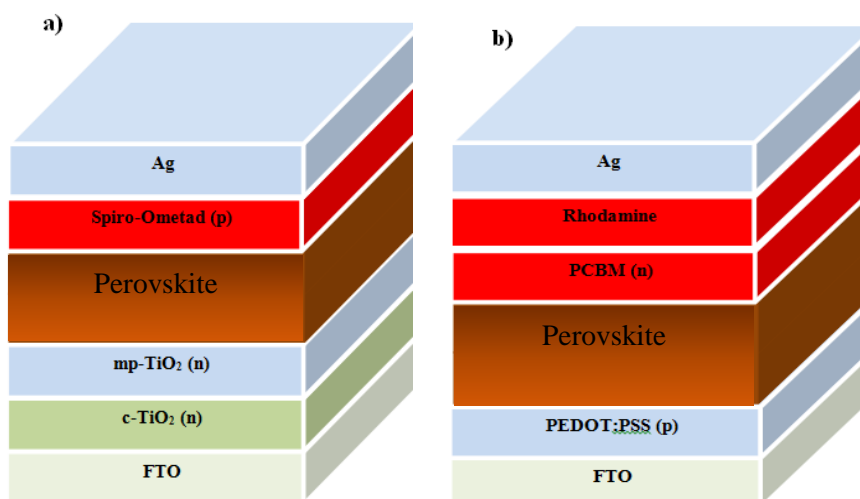


Figure 2.7 (a) n-i-p (b) p-i-n Perovskite solar cell structures

Several device architectures have been designed and fabricated for mesoporous and planar structured perovskite thin films. The interfacial layers of perovskite consist of

electron transport layer (ETL) and hole transport layer (HTL). The ETLs include titanium dioxide ( $\text{TiO}_2$ ), Tin dioxide ( $\text{SnO}_2$ ), copper thiocyanate ( $\text{CuSCN}$ ), zinc oxide ( $\text{ZnO}$ ) nanorod, and PCBM. The HTLs include polymer, spiro-MeOTAD, and PEDOT:PSS. In n-i-p structures (fig 2.7a), perovskite layer is deposited on top of mesoporous  $\text{TiO}_2$  followed by Spiro-Ometad as HTL. While in p-i-n structures (fig 2.7b), perovskite is deposited on top of PEDOT:PSS followed by PCBM as ETL. Finally silver is used as top electrode in both the cases. In both the structures, electrons are collected from ETL and holes from HTL. Figure 2.8 shows the energy band diagram of n-i-p perovskite solar cell where the separated electrons reach to FTO electrode by moving from conduction band of  $\text{TiO}_2$  and holes are transported to silver electrode by moving from valence band of Spiro-MeOTAD.

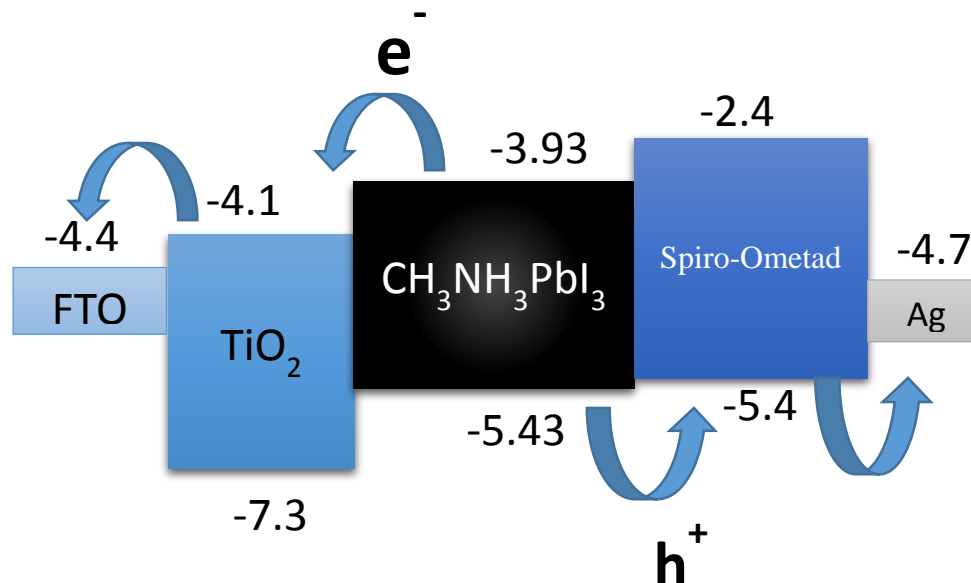


Figure 2.8 Energy band diagram of n-i-p Perovskite solar cell structure

## 2.7 Operating Principles of Characterization Techniques

### 2.7.1 Atomic Force Microscopy

The atomic force microscope (AFM) is a type of scanning probe microscope (SPM). SPMs can measure local, electrical and magnetic properties, such as height, friction, surface potential, magnetism, with suitable probe [80]. The SPM raster-scans the probe over a small area of the sample measuring the local property simultaneously to generate an image. AFMs measures the force between a probe and the sample. The dimensions of the probe is a 3-6  $\mu\text{m}$  tall pyramid with 15-40 nm end radius depending upon the applications. The lateral and vertical resolution of AFM are 30 nm and 0.1 nm due to some convolution.

AFMs measure the vertical and lateral deflections of the cantilever by using the optical lever to generate the required image resolution. Figure 2.9 shows the general schematic of atomic force microscopy. The optical lever reflects the laser beam that falls on the tip of cantilever. The reflected laser beam strikes a position-sensitive photo-detector consisting of four-segment photo-detector. The differences between the segments of photo-detector of signals indicate the position of the laser spot on the detector and thus the angular deflections of the cantilever (frictional measurement). Output of photo-detector is fed to the controller and tip to sample distance is maintained by controller thus maintaining constant force between tip and sample. Hence, a topographic image of the sample is obtained from the deflection of the cantilever.



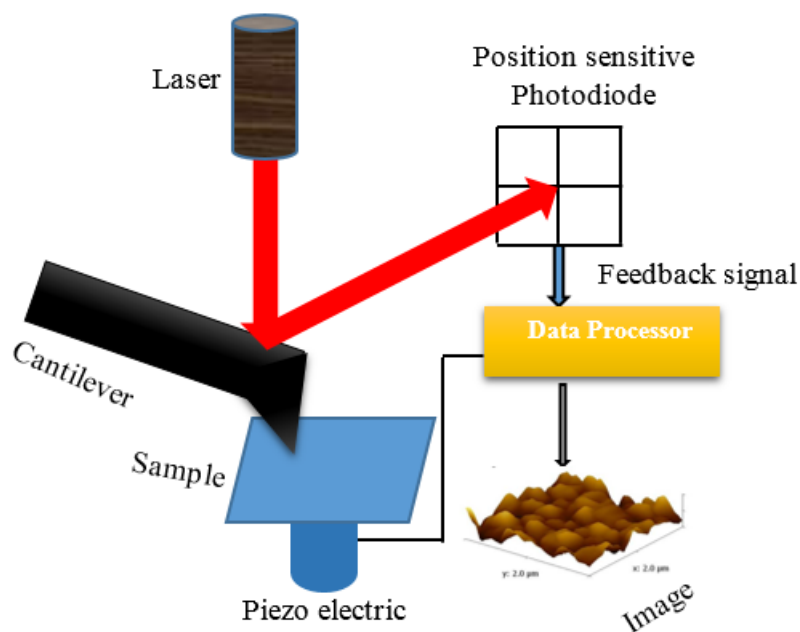


Figure 2.9 Schematic of an atomic force microscopy

There are three modes of AFM imaging, i) contact mode, ii) tapping mode, and iii) non-contact mode. Figure 2.10 shows Force Vs distance curve between tip and sample given by Lennard Jones like potential. This model characterizes the interaction of repulsive and attractive forces and explains the force regimes for various imaging techniques. When the tip is very far away from the sample, there is no interaction. After bringing the tip close to sample, weak attractive forces exists between tip and sample and imaging in this regime is termed as non-contact mode. After bringing the tip-sample more closely, the repulsive van der Waals force predominates and imaging is in intermittent contact regime. When the distance between tip and sample is just a few angstroms, the forces balance, and the net force drops to zero. But, when the total force becomes positive i.e. repulsive, the atoms are in the “contact” regime. In tapping mode and non-contact mode, cantilever is externally oscillated at or close to its resonance frequency. Tip-sample interaction lead to change in oscillation amplitude and resonance frequency.

These change in amplitude and frequency with respect to the reference amplitude and frequency are used as feedback signal to controller for imaging.

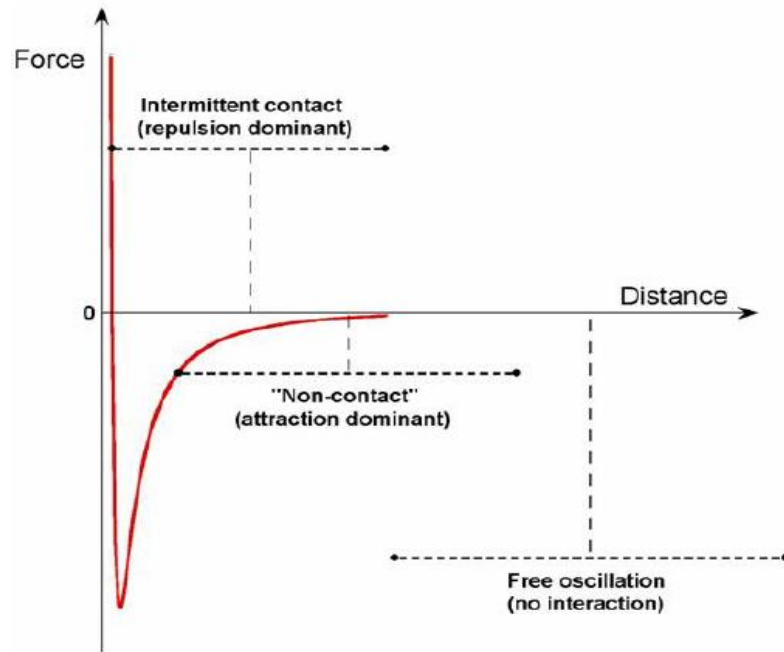


Figure 2.10 Force vs distance curve between tip and sample [81]

### 2.7.2 Kelvin Probe Force Microscopy

Kelvin probe force microscopy (KPFM) is a scanning probe microscopy technique to map the local surface potential of a sample with high spatial resolution. The imaging is done in non-contact regime and minimizes the electrostatic interaction between tip and sample. KPFM can be done by either amplitude modulation or frequency modulation technique. In these techniques, the electrostatic force or the electrostatic force gradient are minimized by applied external bias voltage.

The KPFM combines the non-contact AFM with the Kelvin probe technique. The Kelvin probe microscopy technique was developed by Lord Kelvin in 1898 for the measurement of surface potentials [82]. The measurement is based on the parallel plate

capacitor where sample works as one of the plate and probe i.e., tip with known work function works as another plate of the capacitor. If one of the plate is vibrated at frequency  $w$ , the capacitance changes due to change in distance and results in alternating current in the circuit connecting the plates. This current is reduced to zero by applying a dc-voltage to one of the plates. This voltage corresponds to the contact potential difference (CPD) of the two materials.

The KPFM works on the same principle where a dc-voltage is applied to compensate the CPD between the tip and the sample. However, the electrostatic force is used instead of the current as the controlling parameter. This technique is highly sensitivity for the CPD measurement. The cantilever of an AFM is a very sensitive force probe. Therefore, very smaller size of the capacitor formed by the tip and the sample can be detected.

Mathematically, contact potential difference,  $V_{CPD}$ , between AFM tip and sample is defined as [83]:

$$V_{CPD} = \frac{\phi_t - \phi_s}{-e} \quad 2.15$$

where  $\phi_t$  and  $\phi_s$  are work functions of AFM tip and sample respectively.

Figure 2.11a shows energy levels of the tip and sample surface with different fermi level separated by finite distance without any electrical contacts. In this conditions, both the sample and tip has same vacuum level. When sample and tip are in electrical contact (fig. 2.11b), equilibrium requires Fermi levels to align at steady state. Electrons flow from lower work function to higher work function to reach equilibrium state. A contact potential difference (CPD) will be developed between sample and AFM tip due to charging of sample surface. This contact potential difference can be measured by

applying an external bias such that the external bias had opposite direction than that of contact potential difference and varying the external bias until the contact potential difference gets nullified. The amount of applied external bias (fig. 2.11c) that nullifies the electrical force due to contact potential difference (VCPD) is equal to the work function difference between tip and sample. This is the fundamental principle for measurement of contact potential difference by Kelvin Probe Force Microscopy.

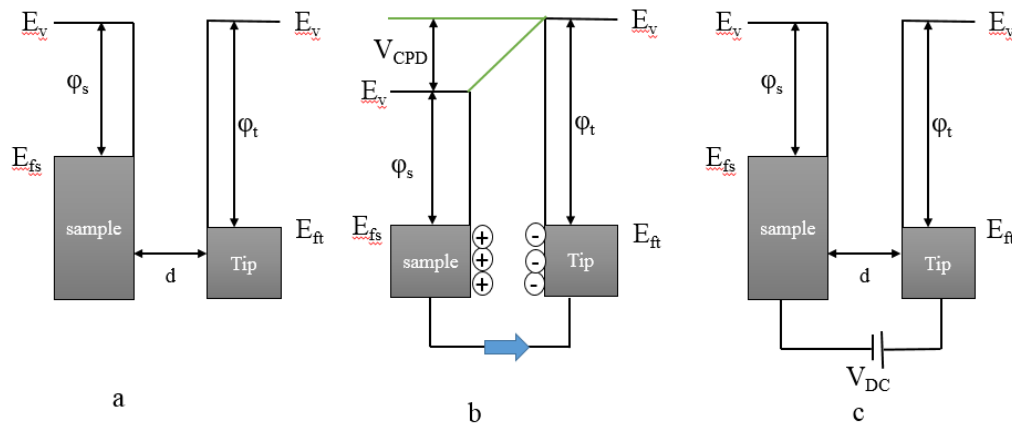


Figure 2.11 Electronic energy levels of the sample and AFM tip (a) tip and sample with separation  $d$  (b) tip and sample with electrical contact (c) tip and sample with external dc bias.

An AC-voltage  $V_{ac}\sin(\omega t)$  added to the dc-voltage ( $V_{dc}$ ) is applied between tip and sample.

Voltage applied to the tip,  $V_{tip}$ , is given by,

$$V_{tip} = V_{DC} + V_{AC} \sin(\omega t) \quad 2.16$$

The resulting oscillating electrostatic force induces an oscillation of the cantilever at the frequency  $\omega$ .  $V_{DC}$  nullifies the oscillating electrical forces originated from contact

potential difference between tip and sample surface. Electrostatic force between tip and the sample,  $F(z)$ , is given by [43]:

$$F(z) = -\frac{1}{2} \Delta V^2 \frac{dC(z)}{dz} \quad 2.17$$

where  $z$  is the direction normal to the sample surface,  $\Delta V$  is the difference between  $V_{CPD}$  and the voltage applied to the tip and  $\frac{dC(z)}{dz}$  is the gradient of the capacitance between AFM tip and sample surface.  $\Delta V$  is given by,

$$\Delta V = V_{tip} \pm V_{CPD} = (V_{DC} \pm V_{CPD}) + V_{AC} \sin(\omega t) \quad 2.18$$

where  $\pm$  sign depends whether the bias is applied to sample (+) or the tip(-).

Equations 2.17 and 2.18 can be combined to yield,

$$F(z) = -\frac{1}{2} [(V_{DC} \pm V_{CPD}) + V_{AC} \sin(\omega t)]^2 \frac{dC(z)}{dz} \quad 2.19$$

Further simplification of Equation 2.19 yields three different force components:

$$F_{DC} = -\frac{1}{2} \frac{dC(z)}{dz} (V_{DC} \pm V_{CPD})^2 \quad 2.20$$

$$F_{\omega} = -\frac{dC(z)}{dz} (V_{DC} \pm V_{CPD}) V_{AC} \sin(\omega t) \quad 2.21$$

$$F_{2\omega} = \frac{1}{4} \frac{dC(z)}{dz} V_{AC}^2 (\cos(2\omega t) - 1) \quad 2.22$$

To measure contact potential difference, force component of eq. 2.19 with frequency  $\omega$  is used. Figure 2.12 shows a schematic of KPFM measurements. AC signal of  $V_{AC} \sin(\omega t)$  with DC signal,  $V_{DC}$ , is applied to tip. Here we can get topography along with surface potential signal. KPFM can be done in two modes either in amplitude modulation or in frequency modulation. Amplitude modulation gives rise to error due to crosstalk between topography and KPFM signal and also the amplitude modulation account for the capacitance formed between sample and not only with tip but also with

cantilever. This problem can be addressed in two ways: either selecting two different off resonance frequency in amplify modulation or performing KPFM in frequency modulation which takes the force gradients and avoids the error in measurement.

The cross talk between KPFM signal and topography signal was minimized by using two different frequency. In figure 2.12, signals with frequency  $\omega_1$  and  $\omega_2$  are used for topography and KPFM imaging respectively. To extract the electrical force component with specific frequency, a lock-in amplifier is employed. The output signal of the lock-in amplifier for KPFM imaging is directly proportional to the difference between  $V_{CPD}$  and  $V_{DC}$ .  $V_{CPD}$  is measured by applying  $V_{DC}$  such that output signal of the lock-in amplifier is nullified and  $F_{\omega}$  equals zero. Hence, value of  $V_{CPD}$  is acquired for each point on the sample surface, composing a map of the contact potential difference or surface potential of the whole sample surface area [84].

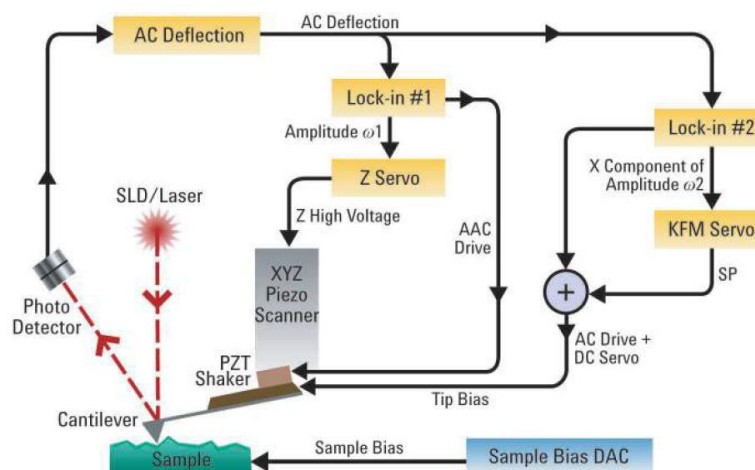


Figure 2.12 Schematic of KPFM measurements[85]

### 2.7.3 X-ray Diffraction

X-ray diffraction (XRD) measurement is used to examine perovskite crystalline structure. It can give quantitative information about lattice spacing, crystalline fraction

and crystallographic orientation of materials. When x-rays are incident on crystallographic planes of the materials, it gets diffracted according to the arrangement of atoms. The diffracted x-rays undergo constructive interference to produce increased intensity along a particular direction based on the periodic spacing between atomic layers. XRD consists of four major components: X-ray source, goniometer, sample holder, and detector. The sample and detector are rotated to adjust proper angle meanwhile the detector counts the number of X-ray photons diffracted by the sample.

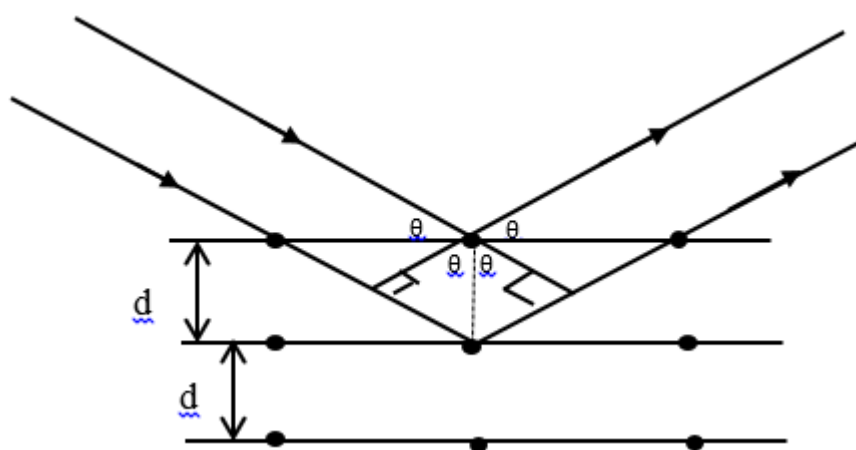


Figure 2.13 Schematic of X ray diffraction from sample

Bragg's law is used to explain the interference pattern of X-rays scattered by crystals. Bragg's Law was derived by the English physicists Sir W.H. Bragg and his son Sir W.L. Bragg in 1913 to explain why the cleavage faces of crystals appear to reflect X-ray beams at certain angles of incidence ( $\theta$ ,  $\lambda$ ). Figure 2.13 schematic of x-ray diffraction. It is given by

$$2d\sin\theta = n\lambda \quad 2.23$$

where  $2d\sin\theta$  is the path difference between the ray of light incident and scattered from the crystal planes,  $d$  is the spacing between the crystal layer,  $\lambda$  is the wavelength of

the X-ray,  $\theta$  is the incident angle, which is the angle between incident ray and the scatter plane and  $n$  is an integer.

#### 2.7.4 Transient Photoconductivity Spectroscopy

Transient photoconductivity is a technique to study the kinetics of sweep-out and recombination in low mobility materials. Recombination causes a reduction in device efficiency due to decrease in  $J_{sc}$  and FF. Therefore, to increase the performance of device, carrier collection by sweep-out to the electrodes (characteristic time,  $\tau_d$ ) with internal electric field must occur prior to carrier recombination within the cell (characteristic time,  $\tau_1$ ). The resolution of the transient measurements depends upon the resistor capacitor (RC) time constant of the device. However, if the thickness is very low transient measurement need to be performed in nanosecond resolution to measure the charge collection and recombination. The transient photoconductivity study also gives the quantitative measurement of charge carrier density, charge carrier mobility, recombination order and bimolecular recombination coefficient. Therefore, the characterization of the photoconductivity provides insight into the physical mechanisms of the solar cells and may help to interpret the different transient experiments.

#### 2.7.5 Transient Photovoltage Spectroscopy

Transient photovoltage (TPV) is a photoconductivity technique in which the device is held at open circuit (using high impedance of oscilloscope  $1M\Omega$ ) with a small short-lived perturbation under steady state conditions. A certain level of illumination is applied in the device whose intensity can be varied. The lifetime of the charge carrier in the device can be calculated using TPV. Figure 2. 14 (a) & (b) shows the schematic of TPV measurement and its decay curve obtained through  $1M\Omega$  resistance.



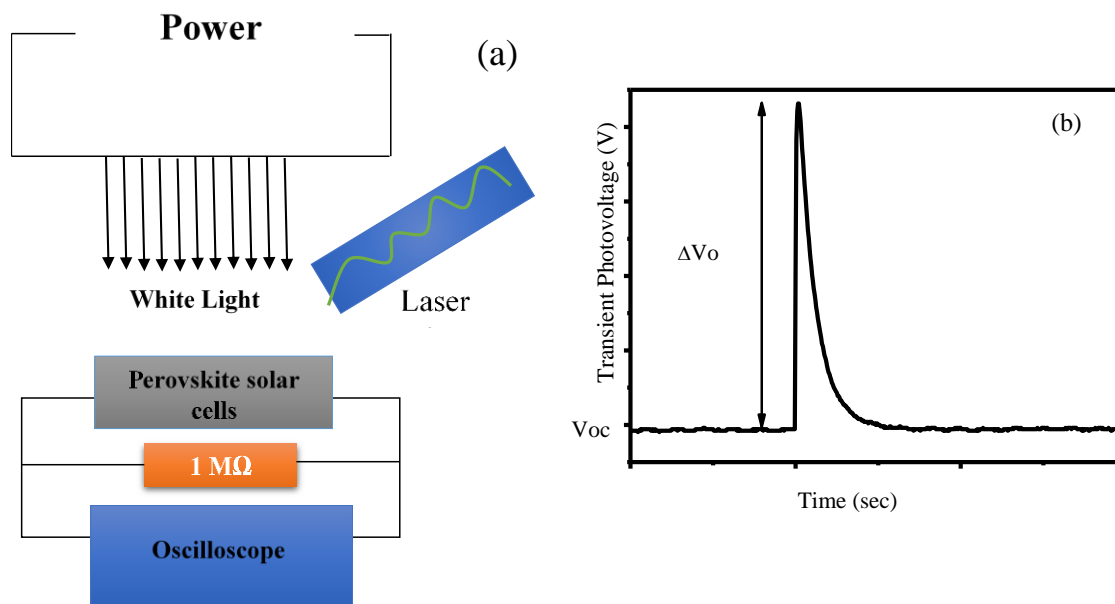


Figure 2.14 (a) Schematic of transient photovoltage (TPV) measurement and (b) TPV decay

The voltage decay in TPV is given by

$$\Delta V = \Delta V_0 \exp(-t/\tau) \quad 2.24$$

This equation was fitted with mono-exponentially decaying function to calculate the loss time  $\tau$  of the device.

### 2.7.6 Transient Photocurrent Spectroscopy

Transient photocurrent (TPC) is a method where the device is held at short circuit condition with short pulse applied to generate excess carrier across the device. TPC gives the collection time of the carriers that are generated with short pulse. The number of total charge carrier density can be calculated by using TPC in conjunction with TPV. The transient current is obtained by calculating the current that flows through the small resistance using ohm's law. Figure. 2.15 shows the TPC setup and transient photocurrent decay produced across the  $50 \Omega$  resistor.

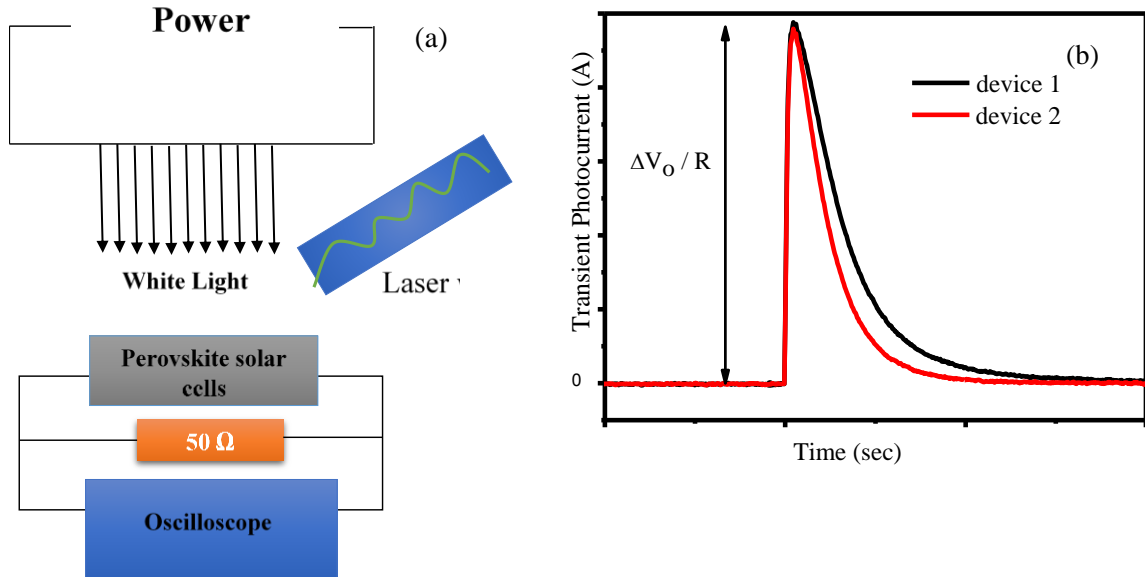


Figure 2.15 (a) Schematic of transient photocurrent and (b) transient photocurrent decay

The transient current decay in TPV is given by

$$\Delta I = \Delta I_0 \exp(-t/\tau) \quad 2.25$$

The value of  $\Delta I_0$  is found by using  $\Delta I_0 = \frac{\Delta V_0}{R}$ . The total charges that are generated can be calculated by integrating the current that is produced during TPC technique.

$$\Delta Q = \int I dt \quad 2.26$$

The total charge carrier density is calculated by using the differential capacitance which is defined as

$$dc = \frac{\Delta Q}{\Delta V_0} \quad 2.27$$

where  $\Delta Q$  is obtained from TPC analysis while  $\Delta V_0$  is the amplitude of TPV transient under different illumination condition.

The total number of charge carrier density under certain illumination condition is given by

$$n = \frac{1}{Aed} \int_0^{V_{oc}} c dV \quad 2.28$$

where  $e$  = elementary charge,  $A$  and  $d$  are the area and thickness of the device.

The diffusion length of the carrier can also be calculated from TPV and TPC analysis as

$$L = \sqrt{D_n \tau_e} \quad 2.29$$

where  $D_n$  = diffusion coefficient and  $\tau_e$  is the recombination time obtained from TPV analysis. The generation time, recombination time, diffusion length and total number of charge carrier density of the respective device will help to identify the performance of the solar cell.

## Chapter 3 Experimental Procedures

### 3.1 Materials

Methylammonium iodide ( $\text{CH}_3\text{NH}_3\text{I}$ ), mesoporous  $\text{TiO}_2$  and compact  $\text{TiO}_2$  were purchased from Dyesol. Lead iodide ( $\text{PbI}_2$ ) was ordered from Acros organics. Spiro-ometad was purchased from Lumtec. FTO coated glass substrates were purchased from Hartford Glass Company.

Table 3.1 Materials used as different layers in perovskite solar cells.

Layer	Material
Cathode	Fluorine tin oxide (FTO)
Electron transport layer (ETL)	Compact $\text{TiO}_2$ , mp- $\text{TiO}_2$
Active layer	Perovskite ( $\text{CH}_3\text{NH}_3\text{PbI}_3$ )
Hole transport layer (HTL)	Spiro-ometad
Anode	Silver (Ag)

### 3.2 Fabrication of Perovskite Solar Cells

Devices were fabricated on fluorine doped tin oxide (FTO) coated glass. FTO layer was etched using zinc powder and diluted hydrochloric acid (HCl). Substrates were subsequently rinsed with DI water. All etched substrates were then cleaned by detergent water, DI water, acetone and isopropanol by sonication for 20 min each. Substrates were then dried, followed by plasma cleaning for 20 min in presence of oxygen.

All cleaned substrates were coated by a compact layer of  $\text{TiO}_2$  from its precursor (titanium diisopropoxide bis(acetylacetonate), 75 wt.% solution in 2-propanol) solution

of 0.15 M and 0.3 M, by spin coating each layer at 4500 rpm for 30 sec. Compact layer of TiO<sub>2</sub> coated substrates were then annealed at 450 °C for 30 min. The substrates were cooled down to room temperature. 1 g of TiO<sub>2</sub> (Dyesol 18NRT with particle size 20 nm) was diluted with 4.436 ml of ethanol and the mixed solution was spin coated at 3000 rpm on top of the compact layer of TiO<sub>2</sub>. The thickness of the mesoporous TiO<sub>2</sub> is approximately 600 nm. The thick substrates were annealed at 450 °C for 30 min, and then cooled down to room temperature. Substrates were then treated by dipping them in TiCl<sub>4</sub> (25 mM) solution for 30 min at 70 °C, followed by rinsing with DI water, ethanol and then annealed at 450 °C for 30 min. Finally, substrates were then transferred inside glove box for depositing perovskite layer using one step spin coating process and two-step sequential deposition method, respectively.

### 3.2.1 One Step Deposition Method

CH<sub>3</sub>NH<sub>3</sub>I (0.1975 g) and PbI<sub>2</sub> (0.5785 g) were mixed in 1ml  $\gamma$ -butyrolactone and stirred for 12 hours. TiO<sub>2</sub> coated substrates were then spin coated with above mixed solution at 2000 rpm for 60 sec, and 3000 rpm for another 60 sec, resulting in a black color film. Black color perovskite (CH<sub>3</sub>NH<sub>3</sub>PbI<sub>3</sub>) films were then annealed at 100 °C for 15, 30 and 60 min, respectively. Spiro-OMeTAD was used as hole transport layer, which was prepared by mixing 72.3 mg of (2,2',7,7'-tetrakis(N,N-di-p-methoxyphenylamine)-9,9-spirobifluorene) (spiro-MeOTAD), 28.8  $\mu$ L of 4-tert-butylpyridine, 17.5  $\mu$ L of a stock solution of [520 mg/mL lithium bis-(trifluoromethylsulfonyl)imide in acetonitrile] in 1 mL of chlorobenzene. Spiro-OMeTAD was spin coated on top of perovskite layer at 2000 rpm for 40 sec. Silver (Ag) was then finally deposited through mask as top electrode in a high vacuum chamber using thermal evaporation.

### 3.2.2 Sequential Deposition Method

PbI<sub>2</sub> solution (462 mg/ml in DMF) was prepared by overnight stirring at 70 °C. The solution was then spin coated on top of the mesoporous TiO<sub>2</sub> layer at 4000 rpm for 90 sec followed by annealing at 70 °C for 30 min. To form perovskite films, the PbI<sub>2</sub> films were pre-wetted in isopropanol and then dipped in CH<sub>3</sub>NH<sub>3</sub>I solution (10 mg/ml in Isopropanol) for 50 sec, followed by immediate spin coating at 6000 rpm for 10 sec. The films were then annealed at 100 °C for different times. Spiro-OMeTAD was used as another hole transport layer, which was prepared by mixing 72.3 mg of (2,2',7,7'-tetrakis(N,N-di-p-methoxyphenylamine)-9,9-spirobifluorene) (spiro-OMeTAD), 28.8 µL of 4-tert-butylpyridine, 17.5 µL of a stock solution of [520 mg/mL lithium bis-(trifluoromethylsulfonyl)imide in acetonitrile] in 1 mL of chlorobenzene. Spiro-OMeTAD was spin coated on top of perovskite layer at 2000 rpm for 40 sec. Silver (Ag) was then finally deposited as top electrode in a high vacuum chamber using thermal evaporation.

To study the effect of doping water in perovskite film, the above PbI<sub>2</sub> films were dipped in CH<sub>3</sub>NH<sub>3</sub>I solution (10 mg/ml in IPA) with 0%, 1%, 3%, 5%, and 7% water without prewetting, followed by immediately spin coating at 5000 rpm for 10 sec outside the glove box. The films were then annealed at 100 °C for 15 min. Similarly, the perovskite film to study the role of humidity in charge transport property, the prepared perovskite film from sequential deposition method has been exposed to different humidity conditions (25% RH, 45% RH, 55% RH, 65% RH and 75% RH) for 5 hrs. The humidity was controlled using Espec SH 240 humidity controller.

### 3.2.3 TiO<sub>2</sub>-Perovskite Interface

To investigate the TiO<sub>2</sub> - perovskite interface with different annealing conditions, a thin layer of compact layer (c-TiO<sub>2</sub>) was spin coated at 4500 rpm for 40 sec and annealed at 450 °C for 30 min. Methylammonium lead iodide (CH<sub>3</sub>NH<sub>3</sub>PbI<sub>3</sub>) solution was spin coated on one corner of the TiO<sub>2</sub> film at 2000 rpm for 60 sec and 3000 rpm for 60 sec; and annealed at 100 °C for different time with the same condition as used for Perovskite solar cell device fabrication. To form the TiO<sub>2</sub>-perovskite interface for sequential deposition technique, the PbI<sub>2</sub> films were deposited at 4000 rpm for 90 sec and annealed at 70 °C for 30 min. These films were pre-wetted in isopropanol and then dipped in CH<sub>3</sub>NH<sub>3</sub>I solution (10 mg/ml in Isopropanol) for 50 sec, followed by spin coating at 6000 rpm for 10 sec on top of c-TiO<sub>2</sub> immediately.

## 3.3 Materials Characterizations

### 3.3.1 UV-Vis Absorption Spectra

Agilent 8453 spectrophotometer was used to determine UV-Vis absorption spectrometer with chem station software. This instrument has tungsten lamp for visible and near infrared (NIR) region and mercury lamp for ultraviolet (UV) region. The schematic of the UV-Visible absorption spectra is shown in figure fig 3.1.

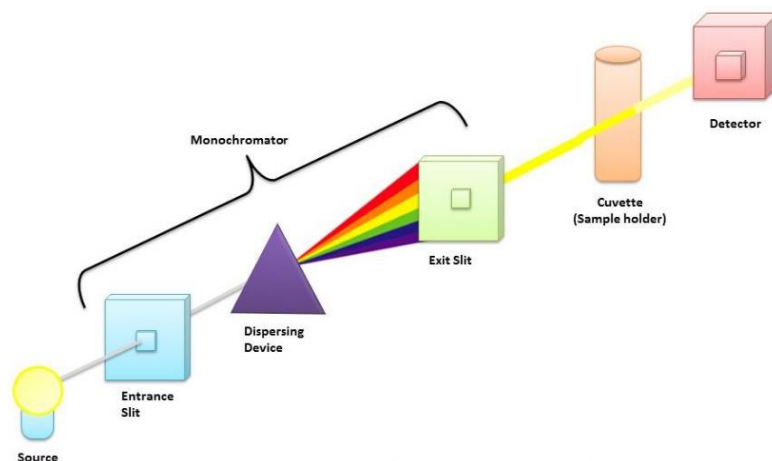


Figure 3.1 Schematic of UV-VIS spectroscopy

Initially, a glass/FTO/TiO<sub>2</sub> substrate was loaded at sample holder for measurements. In this case Blank mode must be chosen. The halogen and filament lamps were turned ON to cover the whole spectra from NIR to UV illuminating on glass substrate. Later a glass/FTO/TiO<sub>2</sub> /perovskite sample treated in different processing conditions were loaded and characterized in automatic mode. The software automatically subtracted the absorption of the glass substrate (what was measured in blank mode) from the total absorption of new loaded samples to gain the absorption spectra of perovskite film.

### 3.3.2 XRD Spectrum

X-ray diffraction (XRD) spectra were recorded from a Rigaku Smartlab system (fig 3.2). The samples were scanned from 5 deg to 60 deg with X-ray of wavelength 1.54 Å from copper source. The generation of X-ray is turn on when the applied tube voltage and current reaches to 40 KV and 44 mA current. The measurement of perovskite film was done in PB/PSA medium resolution with proper optical and sample alignment with step size of 0.01 degree. The perovskite sample is placed on flat surface where the x-ray falls from source and detector is rotated by goniometer along z-axis. The peak intensity is



recorded as a function of  $2\theta$ . Since perovskite samples degrade quickly when exposed to ambient conditions, XRD spectrum of perovskite film were gathered as fast as possible.

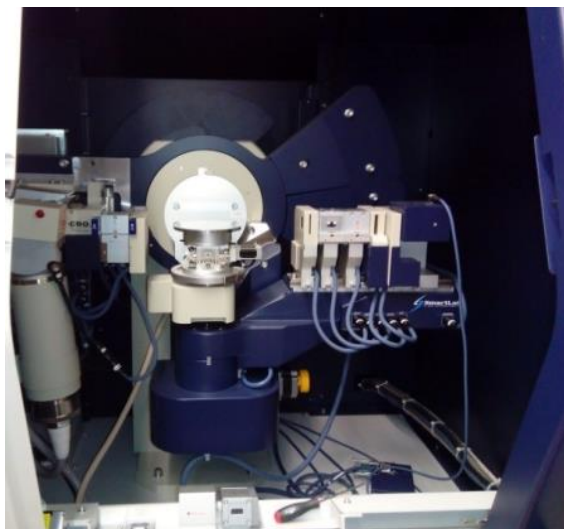


Figure 3.2 Picture showing X-ray diffractometer located in DEH 056 lab

### 3.3.3 Atomic Force Microscopy

Topography images were taken using Agilent 5500 SPM (fig 3.3) in tapping mode. Silicon tip (Budget Sensors, Multi75 Eg) of spring constant  $\sim 1-4$  N/m and tip normal radius of  $\sim 1\text{A}^\circ$  coated with Cr/Pt having a resonance frequency  $\sim 75$  KHz was used. An off-resonance of 100-200 Hz was applied to the resonance peak of cantilever to achieve the required resolution. The operating regime of the tip-sample interaction can be changed from attractive to repulsive either by applying small positive or negative off-resonance. Perovskite sample with different annealing time, exposed to different humidity conditions and prepared by adding different water concentration from 1% to 7% in methyl ammonium iodide solution were used. The obtained images were processed with Gwyddion software.

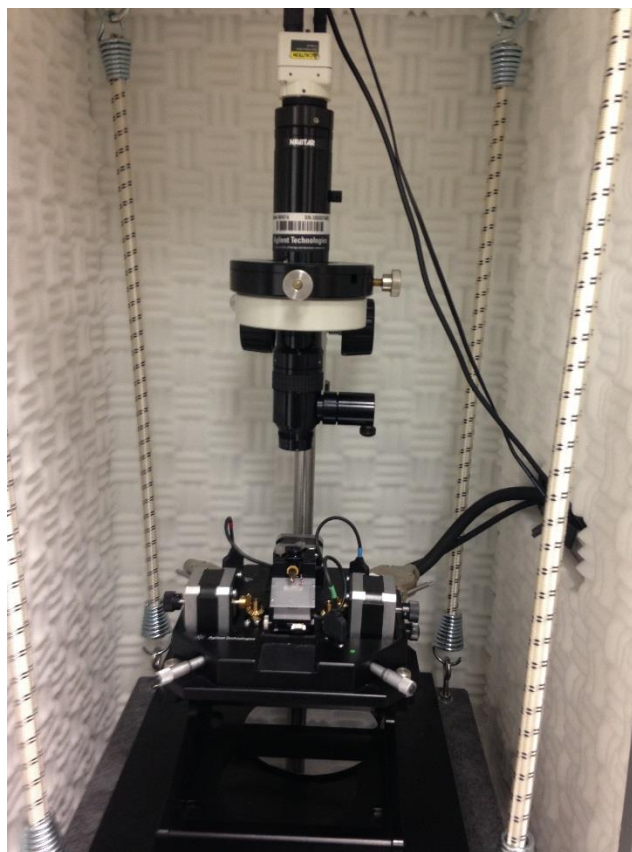


Figure 3.3 Picture of atomic force microscope located in DEH 053 lab

### 3.3.3 Kelvin Probe Force Microscopy

Kelvin probe force microscopy (KPFM) is a non-contact atomic force microscopy method which uses a conducting tip as a Kelvin probe to measure surface potential. It uses a feedback loop that adjusts DC potential which nullifies the force component experienced in the tip, giving rise to surface potential [3, 86, 87]. KPFM is an important tool to obtain back recombination barrier between electron transport layer and the perovskite layer, and within the grains of the perovskite layer. The device performance in terms of energetics of the transport layers i.e. energy positions of electronic bands and their alignment with energy levels of the perovskite layer at different annealing conditions has been determined.

The CPD between the tip and sample was measured together with topography. The tip was excited with an electrical oscillation that induces an electrostatic force between the tip and sample. This electrostatic force was nullified by applying the direct-voltage (dc) offset on the scanning tip at every pixel on the sample. This potential is actually the CPD between the tip and sample, which is their work function difference. Agilent SPM 5500 atomic force microscope equipped with a MAC III controller (comprising three lock-in amplifiers) was used to map surface potential at TiO<sub>2</sub>-perovskite interface and within the perovskite layer. A Budget Sensors Multi 75-EG tip having a platinum/iridium conductive coating was used. The tip's first resonance ( $f_1$ ) frequency of 67 kHz was fed into the first lock-in amplifier (LIA<sub>1</sub>). The vertical tip-sample separation was controlled from LIA<sub>1</sub> which provided the error in the amplitude signal at  $f_1$  to the servo. This first lock in amplifier was used for topographic and phase imaging, while the second frequency ( $f_2$ ) at 5 kHz using a second lock-in amplifier (LIA<sub>2</sub>) gave KPFM measurement. LIA<sub>2</sub> provided an electrical oscillation to the tip at 5 KHz with a certain dc offset to induce an electrostatic force between the tip and sample. This electrostatic amplitude was attained with a dc offset of -3 V and the drive percentage of LIA<sub>2</sub> was approximately 15% to attain amplitude of 0.2 V. In KPFM, an external dc servo was used that nullified the electrostatic interaction by applying a certain dc bias to the tip. This dc bias recorded at each point gave the local CPD or surface potential and hence the images of KPFM were constructed using the pixel coordinates. The AFM and KPFM setup is inside the glovebox. All the KPFM measurements were carried out inside the glove box with O<sub>2</sub> and H<sub>2</sub>O level < 0.1 ppm in order to ensure that the phase of perovskite is not affected by the moisture and oxidation that can complicate the analysis.

The KPFM was done in interface between  $\text{TiO}_2$  -MAPbI<sub>3</sub> on planar samples. The samples were prepared by spin coating Methylammonium lead iodide ( $\text{CH}_3\text{NH}_3\text{PbI}_3$ ) solution on one corner of the  $\text{TiO}_2$  coated substrates. This will give a step interface between  $\text{TiO}_2$  and perovskite. To avoid the topography interference with surface potential measurement we performed SP vs. z spectroscopy. The constant SP at different Z values reveals the independence of SP on surface topography.

### 3.3.4 Current Sensing Atomic Force Microscopy

The nanoscale current distribution of perovskite on the active area of the solar cells was studied using an Agilent 5500 scanning probe microscope installed inside a glove box and equipped with a MAC-III controller. CS-AFM was measured in contact mode using a Pt/Ir coated Si tip (BudgetSensors ContE-G; radius B 20 nm; force constant of 0.2 N/m; resonance frequency of 14 kHz). The CS-AFM cantilever with a small force constant allowed repeated imaging of the perovskite surface without modification. The conducting probe makes contact with the perovskite thin film and measures the current variation across the surface with fixed bias. The holes were injected from a conducting Pt/Ir coated AFM tip into perovskite film and collected at the grounded FTO electrode. The hole current was measured using an in-built preamplifier with 1 nA V<sup>-1</sup> sensitivity. The images were taken at 0.3 V bias to avoid tip induced local oxidation/reduction and impurities on the surface of the film.

## 3.4 Device Characterization

### 3.4.1 Current Density vs Voltage (J-V) Measurements

The current density (J) and voltage (V) were measured using Agilent 4155C under illumination of a solar simulator (Xenon lamp, Newport) with an intensity of ~100

mW/cm<sup>2</sup> (AM 1.5). Agilent 4155C semiconductor parameter analyzer equipped with current and voltage source meters was used for voltage sweep with 10 mV as step voltage and corresponding value of current was simultaneously calculated at each step voltage. The intensity of illumination was calibrated using a National Renewable Energy Laboratory (NREL) photodetector (S1133 14-01) to set distance between the solar cell and solar simulator. Figure 3. 4 shows the schematic of JV measurement set up. All the solar cells with area of 0.16 cm<sup>2</sup> were characterized in the same conditions with 0.5 V/sec scan rate in forward with 0 to 1 V and reverse scan sweeping from 1 to 0.1 V at a relative humidity of 40% in ambient conditions. The cells were characterized both in forward and reverse scan due to the JV hysteresis and degradation of the devices while switching the voltage [88].

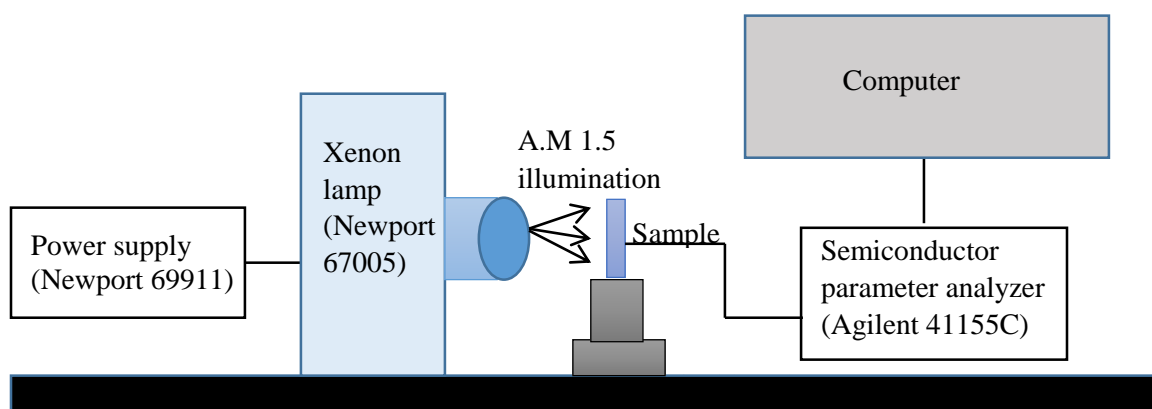


Figure 3. 4 Schematic of JV measurement setup

### 3.4.2 External Quantum Efficiency Measurements

External quantum efficiency (EQE) was measured using Newport IPCE measurement kit (fig 3.5 & 3.6). A xenon lamp was used to simulate sunlight for this experiment. A xenon lamp was used in conjunction with a monochromator, focusing lenses, and an amplifier in order to find the EQE of the solar cell. The reference cell was

again used to determine the correct focusing distance before measuring the EQE of the given solar cell. The semiconductor parameter analyzer then recorded measurements of the given solar cell in order to determine the EQE response.

The Xenon arc lamp (Newport 67005) was focused to S1133 photo detector through the monochromator (Oriel Monochromator 74001) and two focusing lenses. Monochromator was used to pass the light of a certain frequency at a time. Monochromator was programmed using a PC to produce the light of wavelength from 350 nm to 800 nm at an interval of 5 nm. The light from Trans-impedance amplifier was used to amplify the current from the photo detector to voltage ( $V_{ref}$ ), which is recorded using semiconductor parameter analyzer (Agilent 4155C). The photo detector was replaced by the perovskite solar cell to be tested. Similarly, the output voltage of solar cell ( $V_{sample}$ ) at each wavelength was recorded. The EQE of solar cell under test can be calculated as:

$$EQE_{sample} = (V_{sample} * EQE_{ref}) / (V_{ref}) \quad 3.1$$

Since the perovskite film has longer diffusion length, if the light from monochromator is scattered by small amount, the carrier from neighboring regions can also be collected. This leads to more than 100% EQE. To overcome, this problem, we have used red laser at 650 nm whose spot size has been narrowed and the EQE of sample with red laser at 650 nm has been calculated. By using red laser, the correction factor for EQE at 650 nm has been determined accordingly:

$$EQE_{sample \text{ at } 650 \text{ nm}} = (V_{sample \text{ at } 650 \text{ nm}} * EQE_{ref \text{ at } 650 \text{ nm}}) / (V_{ref \text{ at } 650 \text{ nm}}) \quad 3.2$$

$$R \text{ (correction factor)} = EQE_{sample \text{ at } 650 \text{ nm}} / EQE_{sample} \quad 3.3$$

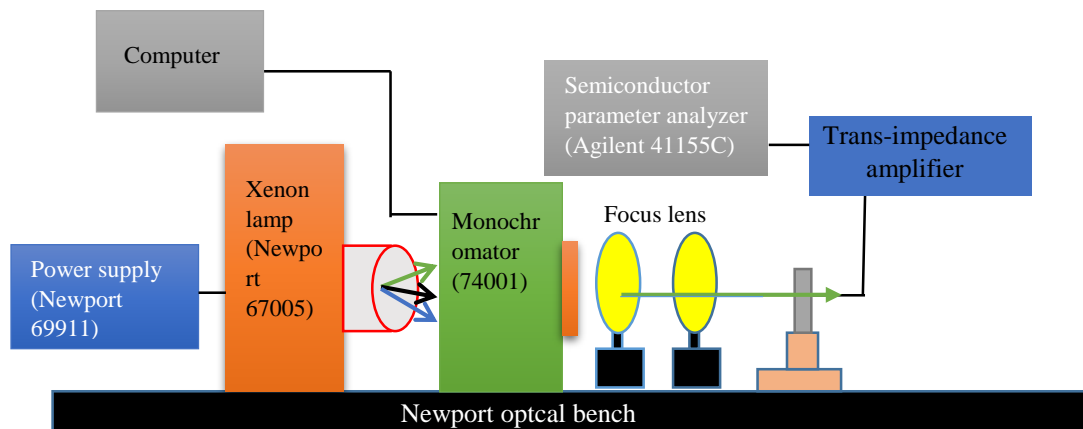


Figure 3. 5 Schematic of external quantum efficiency measurements

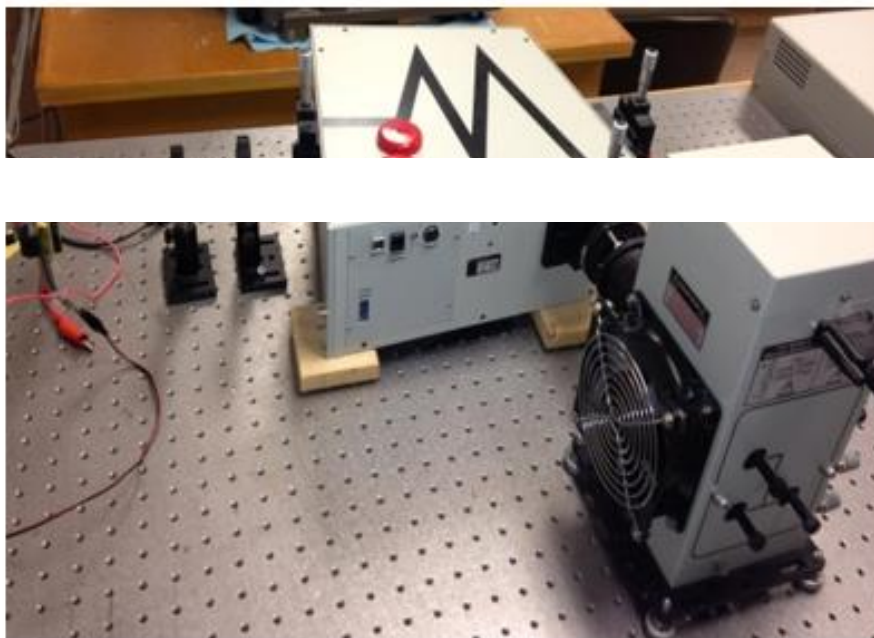


Figure 3. 6 Picture of EQE measurement setup located in DEH 011 Lab

### 3.4.3 Transient Photocurrent/Photovoltage Spectroscopy

Figure 3.7 shows the layout of the experimental set up to measure transient response of the solar cells. The dye laser coupled with the nitrogen laser was used to generate pulses at specific wavelength to create a short transient decay in the cell. The splitter is used to pass the laser on the solar cell and photodiode simultaneously. The signal from the cell and photodiode are recorded in oscilloscope. The transient optical excitation was achieved by focusing a pump laser pulse on the device generated by Model 1011 dye laser (repetition rate  $\sim 4$  Hz, pulse duration  $< 1$  ns) which is excited by OBB's Model OL-4300 Nitrogen Laser (delivers a crisp pulse at 337 nanometers).

The wavelength of the pulse was selected as close to the absorption peak of the perovskite film to reach a uniform generation. The generated transients were recorded using Agilent MSO-X-4154A mixed oscilloscope (1.5 GHz, 5 Gsa/sec). The pulse width of the dye laser was measured on oscilloscope through the response of the photodiode (rise time less than 1 ns, spectral range 280- 1100 nm) as an excitation source to the device. The steady state condition was used by varying light intensity. The obtained data were fitted with mono-exponential decaying function to calculate the collection and loss time of the device.

The transient photocurrent decay was measured with small resistance of the oscilloscope which was  $50 \Omega$  in this case. A short laser pulse was incident in perovskite solar cell from FTO side and generated decay was captured by oscilloscope. Since, the TPC measurement is done in short circuit conditions, the obtained decay completely drops to its zero level. The TPC decay was fitted with mono-exponentially decaying function to find the charge transport time in the device.



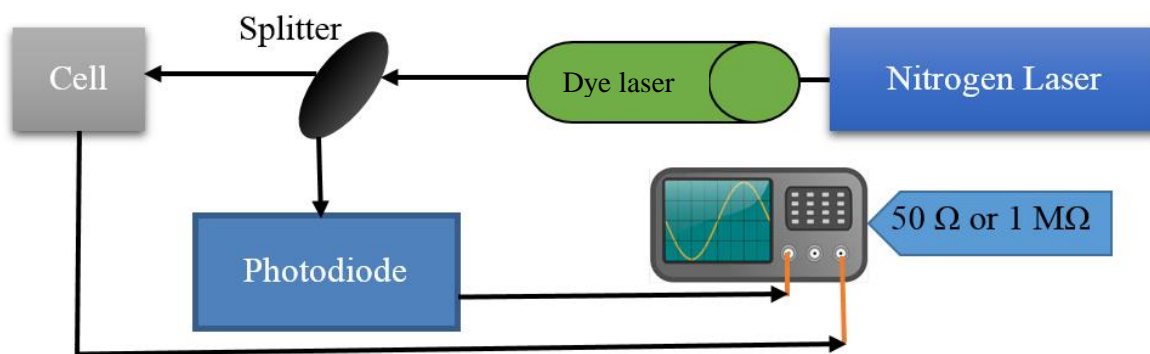


Figure 3.7 Schematic diagram of transient photoconductivity measurement system.

Transient photo-voltage measurements were done using the 1 M $\Omega$  input impedance of the oscilloscope to put the device in the open circuit conditions. During TPV measurements, an external light source with 1-2 sun conditions was illuminated in the device to obtain steady state conditions. The obtained decay was fitted with mono-exponentially decaying function to find the charge carrier life time in the device.

Intensity dependent transient measurements were performed by constantly illuminating an external halogen lamp source via varying the background white intensity from 0 suns to 1.5 suns with interval of 1/12 suns. The open circuit voltage level depends upon the solar cell illumination current density following the equation

$$V_{oc} = \frac{nkT}{q} \ln \left( \frac{J_L}{J_0} + 1 \right),$$

where n is ideality factor, k is Boltzmann constant, T is

temperature, q is elementary charge,  $J_L$  is illumination current density, and  $J_0$  is reversed saturation current density. The solar cell illumination current density depends on background light intensity. Therefore, the open circuit voltage level depends upon background light intensity. In this case when a short pulse (1 ns) of light is incident, the dependence of charge carrier lifetime on charge carrier concentration is obtained. The

charge carrier concentration was varied using different intensities (0 to 1.5 suns with interval of 1/12 suns) of the white light source. The charge carrier density concentration was correlated with the charge carrier lifetime.

## Chapter 4: Results and Analysis

The effect of temperature, water and humidity on the nanoscale charge transport in perovskite solar cells will be discussed in the following sections.

### 4.1 Effect of Temperature on Performance of Perovskite Solar Cell prepared from Single Step and Sequential Deposition Method

#### 4.1.1 XRD Spectra of Perovskite films annealed at 100°C for different time

Figure 4.1 (a) and (b) show XRD spectra of perovskite film without annealing and with annealing at 100°C for 15 min, 30 min 60 min, respectively by single step and sequential deposition method. Strong peaks at 14.09° (110), 28.37° (220) and 31.8° (312) indicate the formation of pure perovskite ( $\text{CH}_3\text{NH}_3\text{PbI}_3$ ) phase with high crystallinity. The peak at 12.65° corresponds to lead iodide ( $\text{PbI}_2$ ) phase.

In single step method, small amount of  $\text{PbI}_2$  phase is formed upon annealing perovskite film.  $\text{PbI}_2$  phase is formed upon annealing due to decomposition of perovskite phase upon annealing at 100 °C, where methyl ammonium iodide ( $\text{CH}_3\text{NH}_3\text{I}$ ) escaped from the perovskite film to form lead iodide ( $\text{PbI}_2$ ). In addition to this, the lead iodide phase in single step method may be due to residual phase from preparation which remains within the bulk of the material. However, a slight reduction in  $\text{PbI}_2$  phase is found after increasing the annealing time from 15 min to 30 min and 60 min. This may be due to the evaporation of loosely bonded  $\text{CH}_3\text{NH}_3\text{I}$  in perovskite film from heating for longer time.

In sequential deposition method, XRD spectrum (Fig 4.1b) shows increase in  $\text{PbI}_2$  phase as annealing time gets longer. In sequential method, the perovskite phase ( $\text{CH}_3\text{NH}_3\text{PbI}_3$ ) forms when dipping  $\text{PbI}_2$  layer in  $\text{CH}_3\text{NH}_3\text{I}$  solution, followed by annealing. In addition, the  $\text{PbI}_2$  layer may not be fully converted to perovskite due to

incomplete conversion which is also seen in XRD spectra of unannealed film. During the annealing,  $\text{CH}_3\text{NH}_3\text{I}$  can escape if annealed too long especially for some loosely bonded perovskite phases [11, 18].  $\text{PbI}_2$  resulting from decomposition of perovskite due to annealing in combination with incomplete conversion of  $\text{PbI}_2$  phase increases with increasing the annealing time in sequential deposition method. However, the  $\text{PbI}_2$  phase does not change significantly in single step method after annealing for longer time.

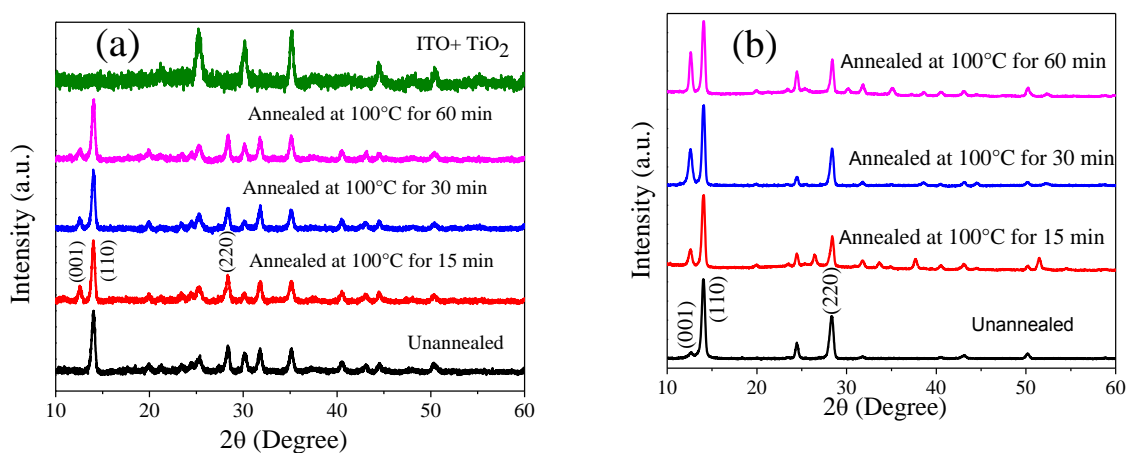


Figure 4.1 XRD spectra of perovskite films annealed at 100°C for different time prepared by (a) single step and (b) sequential deposition method, respectively

The possible reason is that in single step method, two precursor solutions ( $\text{CH}_3\text{NH}_3\text{I}$  and  $\text{PbI}_2$ ) were mixed together in a single solvent so that both  $\text{CH}_3\text{NH}_3\text{I}$  and  $\text{PbI}_2$  have better contact with each other to form perovskite  $\text{CH}_3\text{NH}_3\text{PbI}_3$ . Even after perovskite  $\text{CH}_3\text{NH}_3\text{PbI}_3$  decomposes when we apply heating/annealing, they will be readily re-form perovskite  $\text{CH}_3\text{NH}_3\text{PbI}_3$ .

Sequential deposition method was done by first coating the  $\text{PbI}_2$  layer and then dipping it in MAI ( $\text{CH}_3\text{NH}_3\text{I}$ ) solution to form perovskite film. This leaves some unconverted  $\text{PbI}_2$  within the bulk of the perovskite film which gives higher content of  $\text{PbI}_2$  in sequential deposition method compared to one step method where the two

precursors i.e.  $\text{PbI}_2$  and MAI are mixed together to form homogeneous solution. This solution is spin coated to form perovskite film which leaves lower amount of  $\text{PbI}_2$  in perovskite film due to complete miscibility between  $\text{PbI}_2$  and MAI.

#### 4.1.2 SEM images of Perovskite film prepared from Single Step and Sequential Deposition Method

Figure 4.2 shows SEM images of perovskite films prepared from single step and sequential deposition method. It is found that the morphology of the single step and sequential deposition method has huge difference. The surface coverage of perovskite layer in single step method is very poor. However, smooth and complete coverage of perovskite films were found in sequential deposition method. There is no visible change in morphology of SEM images for single step method after annealing for 15 min at  $100^\circ\text{C}$ . However, the morphology of the film becomes more compact without gaps after annealing the films at  $100^\circ\text{C}$  for 15 min in sequential deposition method. Therefore, device efficiency of perovskite film prepared from sequential deposition method is higher than single step methods.

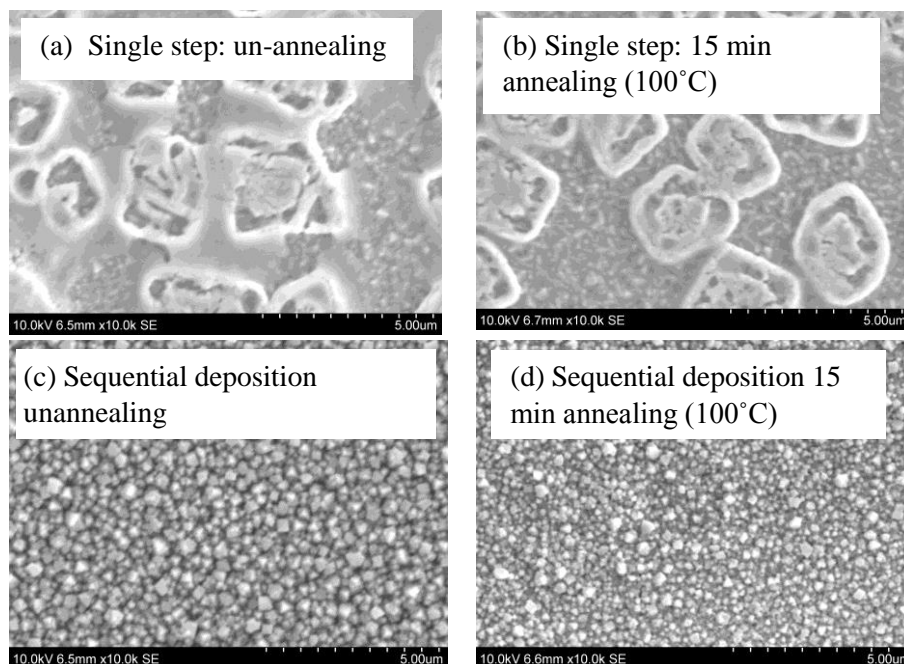


Figure 4. 2 SEM images of perovskite films from single step method (a) un-annealing, (b) 15 min and from sequential deposition method (c) un-annealing, and (d) 15 min annealing at 100°C.

#### 4.1.3 Topography and KPFM images of TiO<sub>2</sub>-Perovskite interface Single Step Method

Figure 4.3 shows topography and KPFM images of the TiO<sub>2</sub> - perovskite interface prepared by depositing perovskite films on TiO<sub>2</sub> layer with un-annealing and annealing at 100°C for 15 min, 30 min 60 min, respectively. The grain size of perovskite films decreases from 200 nm for un-annealing (Fig 4.3a) to 85-100 nm in the 30 min (Fig 4.3c) and 60 min (Fig 4.3d) annealing films. However, grain size does not change significantly for 15 min annealed sample (Fig 4.3b) at the interface between TiO<sub>2</sub> - perovskite. Figs. 4.3 (e-h) show the change of surface potential at the TiO<sub>2</sub> - perovskite interface upon the annealing time. The dark brown region in Figs. 4.3 (e-h) is perovskite and the light brown is TiO<sub>2</sub>. It was seen higher potential at the TiO<sub>2</sub> and lower potential in perovskite side.

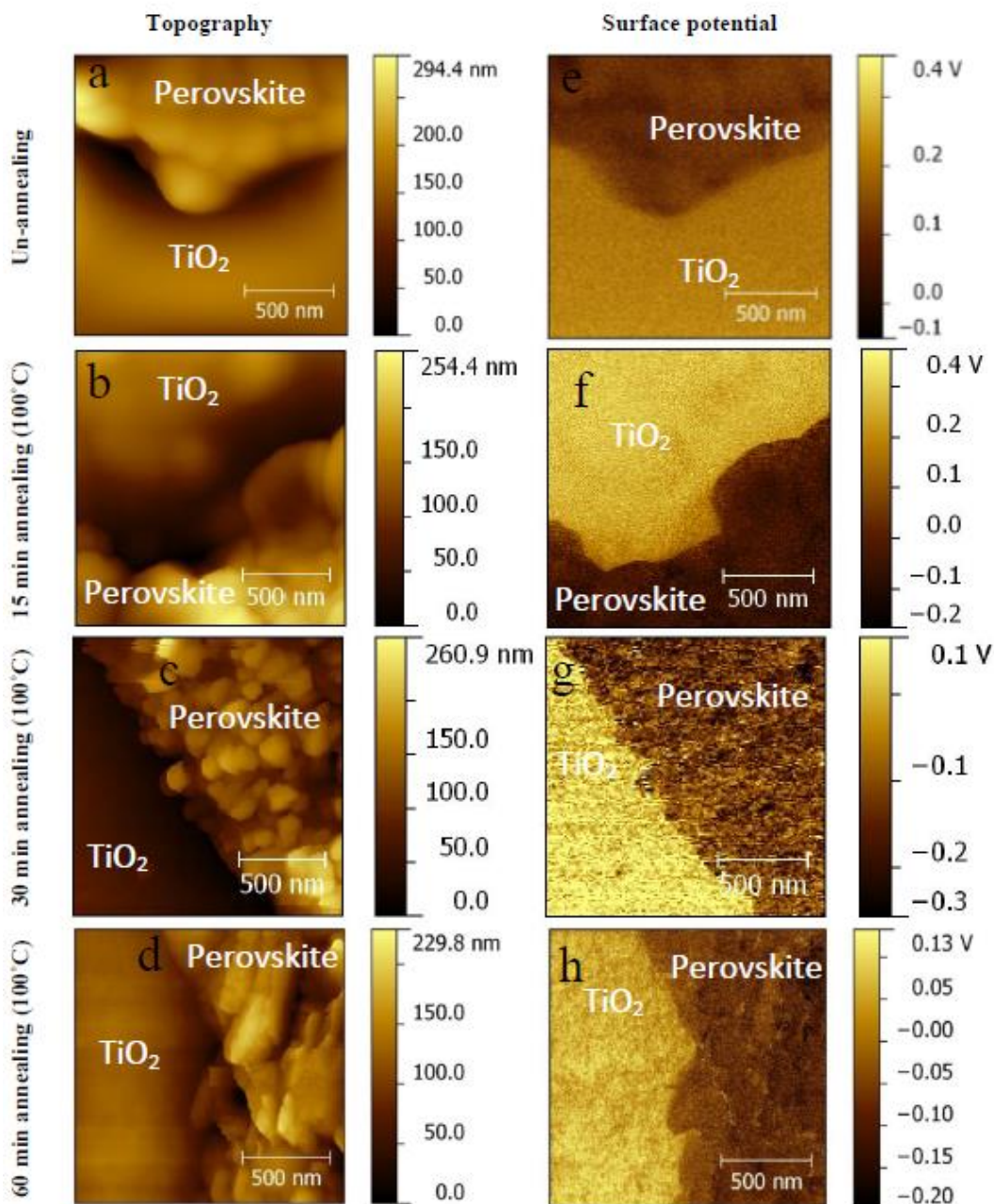


Figure 4.3 (a-d) 2D topography and (e-h) 2D surface potential of the perovskite-TiO<sub>2</sub> interface by depositing perovskite films on TiO<sub>2</sub> layer from single step method with un-annealing and annealing for 15 min, 30 min, and

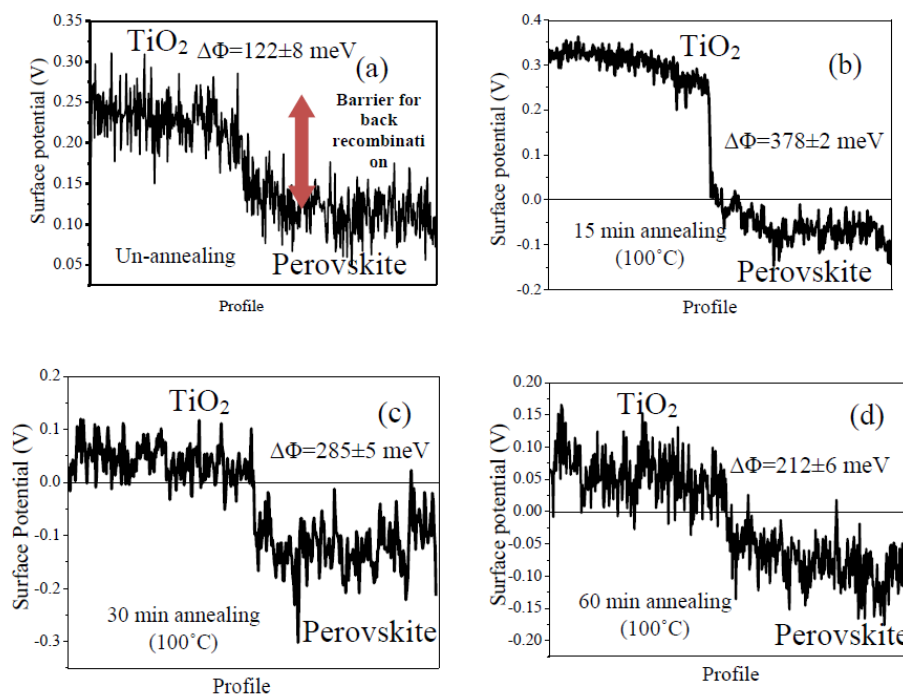


Figure 4.4 Surface potential line profiles across the perovskite-TiO<sub>2</sub> interface from single step method for (a) un-annealing, (b) 15 min, (c) 30 min, and (d) 60 min annealing at 100°C.

The difference in surface potential between TiO<sub>2</sub> – perovskite increases with annealing time. This is in agreement with the previously reported KPFM measurements of perovskite film which revealed the role of annealing to suppress the recombination. Figures 4.4 (a-d) shows the line scanning profile of surface potential at the perovskite-TiO<sub>2</sub> interface. The difference in surface potential between perovskite and TiO<sub>2</sub> is the energy barrier that an electron from TiO<sub>2</sub> and a hole from perovskite need to overcome for recombination. As the annealing time increases from un-annealing to 15 min, 30 min and 60 min at 100°C, the back recombination barrier increases.



Table 4.1 Energetic barriers for back recombination between holes in perovskite layer and electrons in ETL layer measured by KPFM. The films were prepared from single step method annealed at 100°C for different time.

<b>Perovskite film</b>	<b>Energetic barriers for back recombination</b>
Un-annealed	0.122 ±0.008 eV
15 min annealing	0.378± 0.002 eV
30 min annealing	0.285 ± 0.005 eV
60 min annealing	0.212 ± 0.005 eV

Table 4.1 summarizes the values of back recombination barrier at the TiO<sub>2</sub> - perovskite interface for different annealing time. For un-annealed samples, KPFM measurements reveal an energy barrier of 0.122 eV (Fig. 4.4a) between TiO<sub>2</sub> and perovskite. When annealed at 100°C for 15 min, 30 min and 60 min using the single step method, KPFM measurements exhibit that the back recombination barrier between TiO<sub>2</sub> and perovskite increases to 0.378 eV (Fig. 4.4b), 0.285eV (Fig. 4.4c) and 0.212 eV (Fig. 4.4d), respectively. This is much higher than 0.122 eV for unannealed samples. Such increased barriers upon annealing become more significant to prevent the back recombination between electrons from TiO<sub>2</sub> and holes from perovskite. This is also supported by the JV curves as open circuit voltage ( $V_{oc}$ ) increase significantly after annealing (Fig. 4.9 and table 4.5). The XRD spectra in Fig. 4.1a suggest that the annealing processing helps to form a thin layer of lead iodide (PbI<sub>2</sub>). This PbI<sub>2</sub> layer increases back recombination barrier, which was reported previously[18]. This is further confirmed by measuring TiO<sub>2</sub> – perovskite interface from sequential deposition method and will be discussed later.

#### 4.1.4 Surface Potential distribution of Perovskite film from Single Step Method

Figure 4.5 shows the surface potential distribution of perovskite film unannealed and annealed at 100°C for 15 min, 30 min and 60 min using the single step method. The surface potential distributions were acquired from KPFM images shown in Fig. 4.6. The surface potential of perovskite films annealed at 100°C for 15 min, 30 min and 60 min were higher compared to unannealed sample.

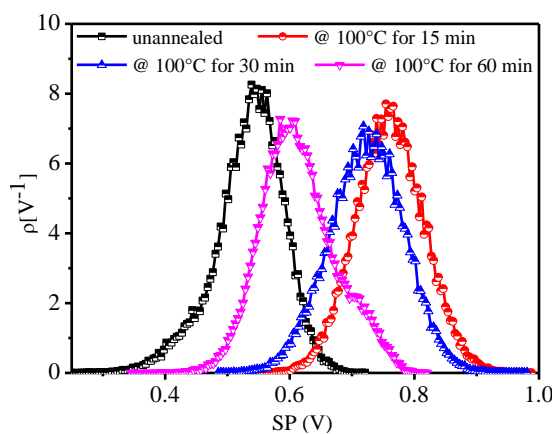


Figure 4. 5 Surface potential distribution of perovskite films prepared by single step method at different conditions of unannealing and annealing at 100°C for 15 min, 30 min, and 60 min.

The surface potential of perovskite film annealed at 100°C for 15 min shows highest surface potential which is mainly due to reduced surface defects caused by the dangling bonds. These dangling bond acts as a trap center for electrons. It is reported that the origin of dangling bonds is due to the exposed iodine atoms in perovskite film [13]. It is found that annealing the film at 100°C for 15 min helps for reconstruction of the

perovskite surface reducing the structural defects in the surface.

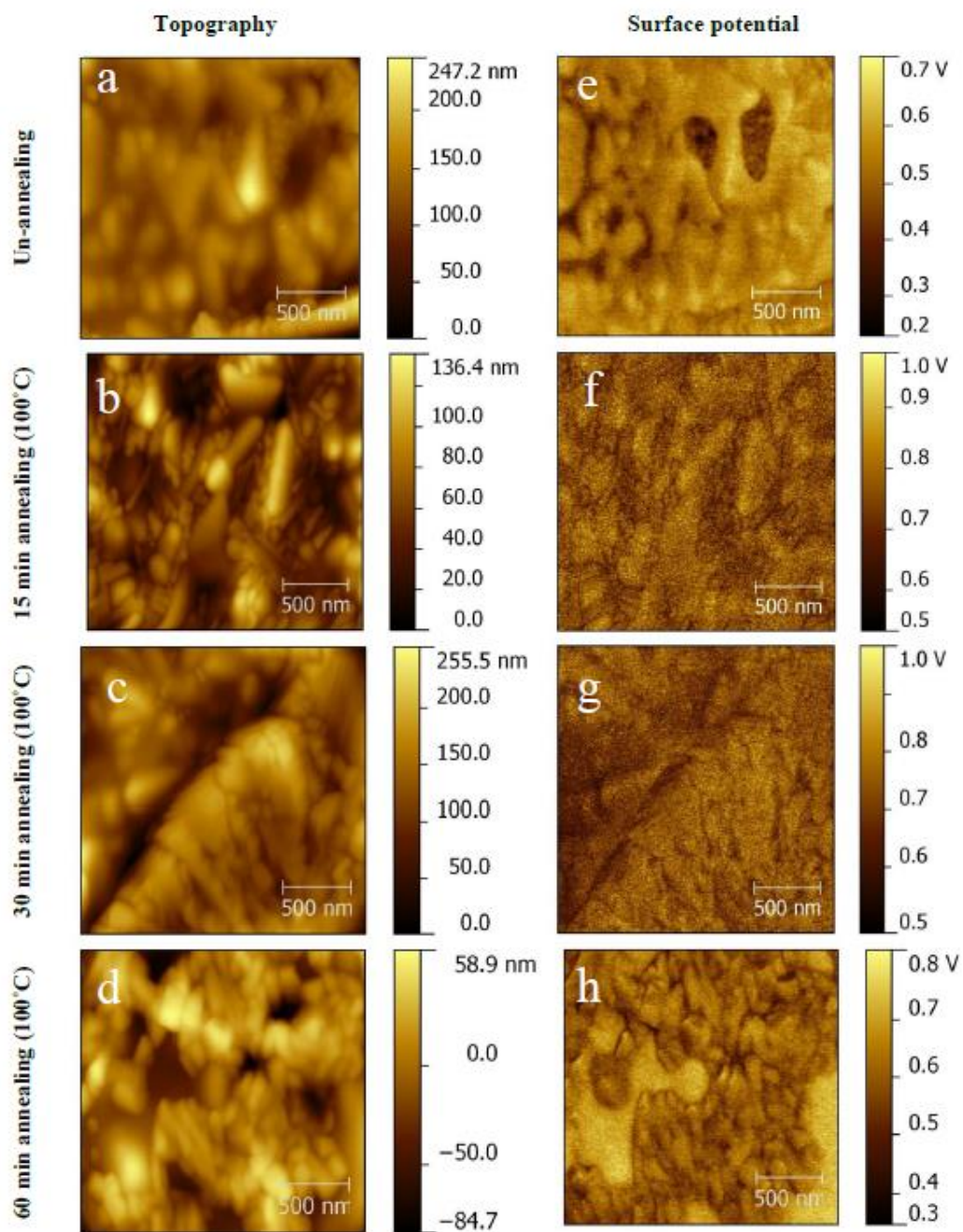


Figure 4.6 (a-d) 2D topography and (e-h) 2D surface potential images of perovskite films prepared by single step method at different conditions of unannealing and annealing at 100°C for 15 min, 30 min, and 60 min.

In addition, the reduced surface defects which act as electron traps also reduce hysteresis of the prepared device as surface trap states are considered as one of the sources for origin of the hysteresis. The decrease in potential for perovskite film annealed for longer time than 15 min can be attributed to the formation of surface defects from vacancies and intrinsic defects due to long term thermal annealing [14].

#### 4.1.5 Topography and KPFM images of perovskite film from sequential deposition method

Figures 4.7 (a-d) show 2D surface topography of perovskite films with un-annealing and annealing at 100°C for 15 min, 30 min 60 min, respectively from sequential deposition. The un-annealed films show larger grains with 500-800 nm in size as shown in Fig. 4.7a. Annealing of perovskite films led to fast evaporation of solvent molecules in the film and fast crystallization of perovskite films. This results in small particle size. However, the perovskite film without annealing forms the perovskite crystal with slower inter diffusion of  $\text{PbI}_2$  and MAI whereas the annealed films forms the perovskite crystal instantaneously due to thermal annealing leaving solvent to evaporate immediately. This led to slow crystallization of perovskite phase because the residual solvent molecules assisted the interdiffusion of  $\text{PbI}_2$  and MAI components to each other, leading to formation of large particles. The grain size decreases to ~75-250 nm upon annealing the perovskite film at 100°C for 15 min. However, the grain size remains similar after annealing at 100°C for 30 min. Slight increase in grain size (250 nm – 400 nm) was found after longer annealing time (100°C for 60 min). It is found that the film annealed at 100 °C for 15 min have compact and closely packed surface topography. Figure 4.7 (e-h) show 2D surface potential maps of perovskite films with un-annealing

and annealing at 100°C for 15 min, 30 min 60 min, respectively. KPFM of perovskite films demonstrates higher surface potential at the grain boundaries (GBs) than within grains. This corresponds to a downward band bending in the energy band diagram leading to the minority carriers electrons in p-type absorber layer to be attracted towards GBs.[3, 89, 90] It has been shown that the grain boundary in this type of materials enhance minority carrier collection and provides current path for minority carriers to reach to the n-type layers and enhances the overall performance of the device leading to better charge transport suppressing recombination.

Table 4.2 summarizes the average grain boundary potential for perovskite film with un-annealing and annealing at 100°C for 15 min, 30 min 60 min, respectively. The grain boundary potential decreases from 479 meV to 337 meV from unannealing to annealing at 100°C for 15 min. However, the grain boundary potential increases to 395 meV and 386 meV when annealed at 100°C for 30 min and 60 min respectively. The decrease in grain boundary potential helps to charge transport within the grains of the perovskite film by reducing the barrier between GBs. This decrease in grain boundary potential may be due to the formation of  $\text{PbI}_2$  upon annealing at 100 °C for 15 min as shown in XRD spectrum of fig 4.1 (b).

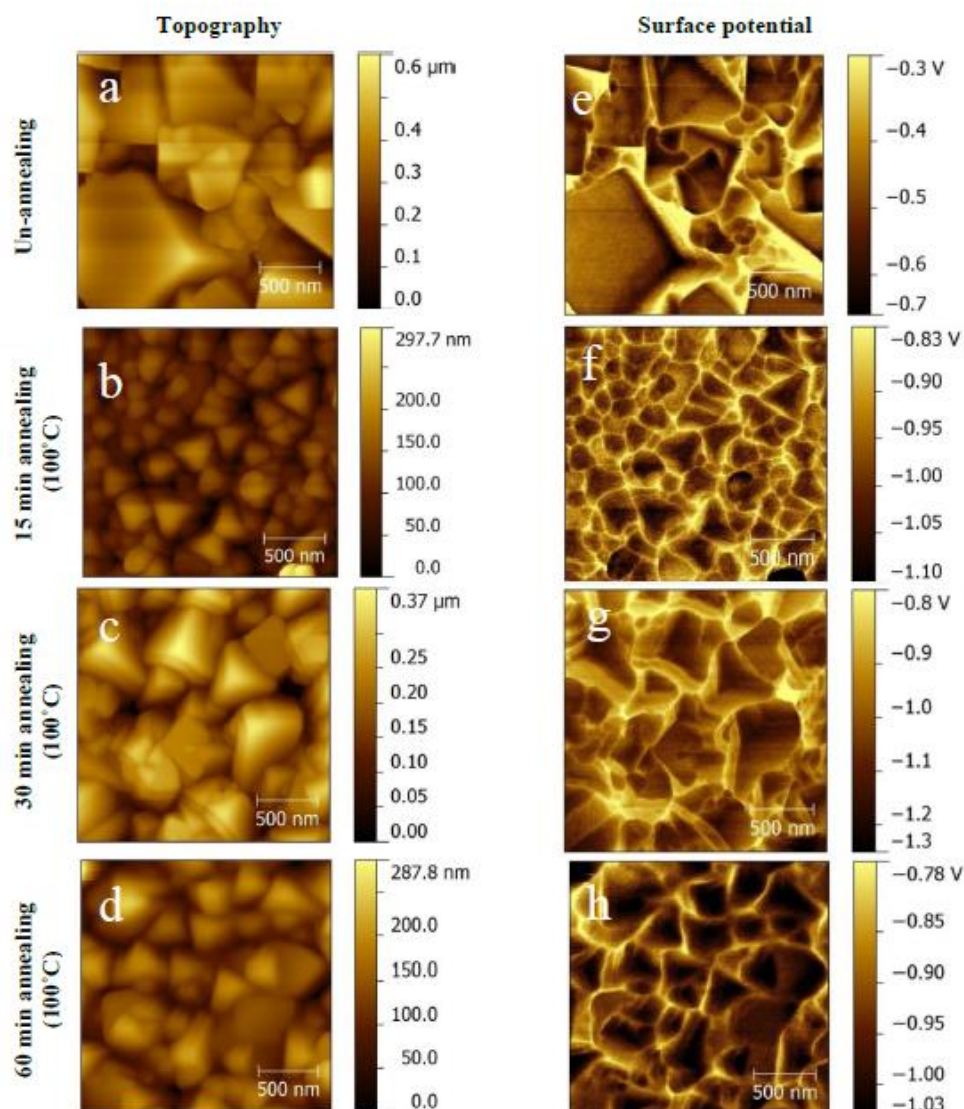


Figure 4.7 (a-d) 2D topography and (e-h) 2D surface potential images of perovskite films prepared by sequential deposition method at different conditions of unannealing and annealing at 100°C for 15 min, 30 min, and 60 min.

Sequential deposition method will leave some  $\text{PbI}_2$  together with  $\text{MAPbI}_3$ . A small amount of  $\text{PbI}_2$  is helpful for decreasing the recombination providing the beneficial role. This is one of the reasons for lowest grain boundary potential for perovskite film annealed at 100 °C for 15 min. However, further increasing the annealing time led to the

formation of MAPbI<sub>3</sub> grains with more PbI<sub>2</sub> shells which increase the inter-grain boundary potential reducing the charge transport. Grain boundary has vacancies and interstitials and the polarity of grain boundary may be different from grain interiors. In addition, grain boundary in perovskite oxides is found to be depleted and forms space charge regions due to formation of oxygen vacancies at grain boundary.[19] Grain boundary potential decreases by 142 mV upon annealing for perovskite film annealed at 100 °C for 15 mins with respect to unannealed samples.

Table 4.2 Average grain boundary potential of perovskite films prepared from sequential deposition method annealed at 100°C for different time.

<b>Perovskite film</b>	<b>Average grain boundary potential (meV)</b>
unannealed	479
15 min annealing (100 °C)	337
30 min annealing (100 °C)	395
60 min annealing (100 °C)	386

#### 4.1.6 Recombination mechanism between Perovskite-TiO<sub>2</sub> interface

Figure 4.8 shows the schematic of the role of lead iodide to reduce the recombination between electrons from TiO<sub>2</sub> and holes from perovskite. Optimum amount of PbI<sub>2</sub> will reduce recombination of electrons from TiO<sub>2</sub> and holes from perovskite layer by the introduction of lead iodide (PbI<sub>2</sub>) between TiO<sub>2</sub> and perovskite. TiO<sub>2</sub> contains dominating surface defects (Ti<sup>3+</sup> sites) at approximately 5.0 eV which act as deep electron-donating sites. Thus, the probability of recombining electrons from TiO<sub>2</sub> and holes from perovskite with energy level 5.43 eV is higher due to energy matching. Therefore, the wide band gap PbI<sub>2</sub> helps to reduce the recombination at the interface.

Thus, the highest back recombination barrier obtained for perovskite film annealed at 100°C for 15 min can be attributed to form during annealing. This is in agreement with the charge transport time and charge carrier life time obtained from transient measurement. The perovskite film annealed at 100°C for 15 min has fastest charge transport and longer carrier life time than unannealed sample (figure 4.12). It has been found that the back recombination decreases with optimum content of  $\text{PbI}_2$  in perovskite film which corresponds to annealing at 100°C for 15 min for both the single step and sequential deposition method. The inter grain boundary potential was found to be minimum for perovskite film annealed at 100°C for 15 min. So, It is conclude that a small amount of lead iodide helps to reduce recombination and increase open circuit voltage and charge transport. Therefore, the optimum amount of  $\text{PbI}_2$  at perovskite- $\text{TiO}_2$  is critical because excess amount of  $\text{PbI}_2$  may partially block the electron transport because of wideband gap.

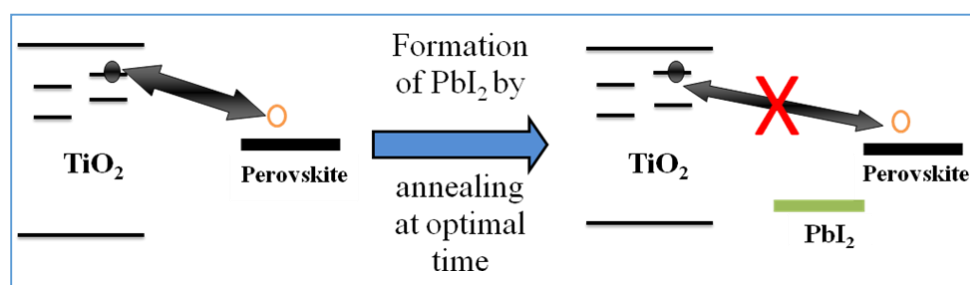


Figure 4. 8 Formation of  $\text{PbI}_2$  prevents back recombination between electrons from  $\text{TiO}_2$  and holes from perovskite.

#### 4.1.7 Topography and KPFM images of $\text{TiO}_2$ - Perovskite interface Sequential Deposition Method

Figures 4.9 (a-d) show 2D SP images and (e-h) represent the line scanning profile of surface potential at the perovskite- $\text{TiO}_2$  interface from sequential deposition method.



The largest difference in surface potential between perovskite-TiO<sub>2</sub> for film annealed at 100°C for 15 min (Fig. 4.9b) may be caused by the passivation of the perovskite defect states due to formation of PbI<sub>2</sub> as shown in XRD pattern (Fig. 4.1b). The back recombination barrier is the difference in surface potential between perovskite and TiO<sub>2</sub>. As the annealing time increases, the back recombination barrier for 15 min, 30 min and 60 min at 100°C, increases with respect to unannealed sample. This helps to increase open circuit voltage (V<sub>oc</sub>) after annealing (fig. 4.10 and table 4.5). However, it is interesting to note that the difference in surface potential between perovskite-TiO<sub>2</sub> becomes minimum after annealing for longer time.

This may be due to the formation of more than 50% PbI<sub>2</sub> phase as shown in XRD pattern. Therefore, an optimum amount of lead iodide helps to reduce the back recombination of holes from perovskite to electrons from TiO<sub>2</sub>. Excess amount of PbI<sub>2</sub> can cause additional blockade for electrons from perovskite to move to TiO<sub>2</sub> due to its wide band gap. Table 4.3 summarizes the values of back recombination barrier at the TiO<sub>2</sub> - perovskite interface for different annealing time. For un-annealed samples, KPFM measurements reveal an energy barrier of 0.060 eV (Fig. 4.9a) between TiO<sub>2</sub> and perovskite.

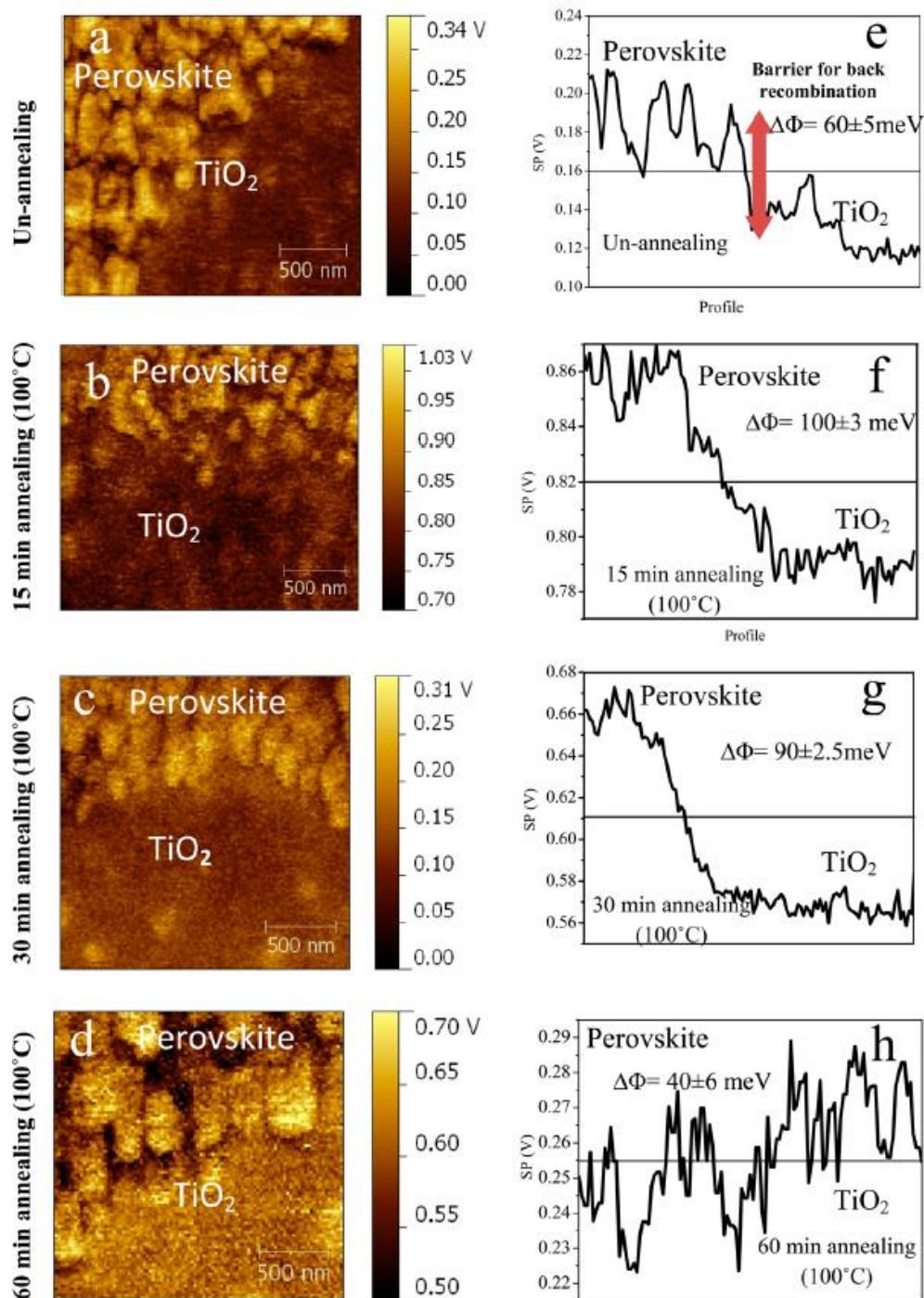


Figure 4.9 (a-d) 2D surface potential mapping and (e-h) surface potential line profile of the perovskite-TiO<sub>2</sub> interface by depositing Perovskite films on TiO<sub>2</sub> layer from sequential deposition method with un-annealing and annealing for 15 min, 30 min, and 60 min at 100°C.

When annealed at 100°C for 15 min, 30 min and 60 min using the sequential deposition method, KPFM measurements exhibit that the back recombination barrier between TiO<sub>2</sub> and perovskite increases to 0.100 eV (Fig. 4.9b), 0.090eV (Fig. 4.9c) and then decreases to 0.040 eV (Fig. 4.9d), respectively. Therefore, the optimum annealing time of 15 min at 100°C has significant barriers to prevent the back recombination between electrons from TiO<sub>2</sub> and holes from perovskite. This will help to increase open circuit voltage ( $V_{oc}$ ) of the device after annealing.

Table 4.3 Energetic barriers for back recombination between holes in perovskite layer and electrons in ETL layer measured by KPFM. The films were prepared from sequential method annealed at 100°C for different time.

<b>Perovskite film</b>	<b>Energetic barriers for back recombination</b>
Un-annealed	0.060±0.0005 eV
15 min annealing	0.100±0.0003 eV
30 min annealing	0.090±0.00025 eV
60 min annealing	0.040±0.0006 eV

#### 4.1.8 Current Voltage curve of Sequential Deposition and Single Step Method

The JV curves of sequential deposition method (Fig. 4.10) and single step method (Fig. 4.11) give highest device performance for perovskite films annealed at 100 °C for 15 mins with device area of 0.16 cm<sup>2</sup>. Tables 4.5 and 4.6 show that the increase in efficiency is mainly due to improvement in  $J_{SC}$  and  $V_{OC}$ . Increase in  $V_{oc}$  is due to decrease in recombination as back recombination barrier increases from 0.122 eV to 0.378 eV for single step method and from 0.06 eV to 0.10 eV for sequential deposition method.

The deviation of  $J_{sc}$ ,  $V_{oc}$  and FF in forward and reverse scan was calculated comparing with the corresponding average value of forward and reverse scan. One of the reasons for increased  $J_{sc}$  upon annealing may be the improved charge transport caused by decrease in grain boundary potential between the grains from 0.479 eV for un-annealed films to 0.337 eV in 15 min annealed films.

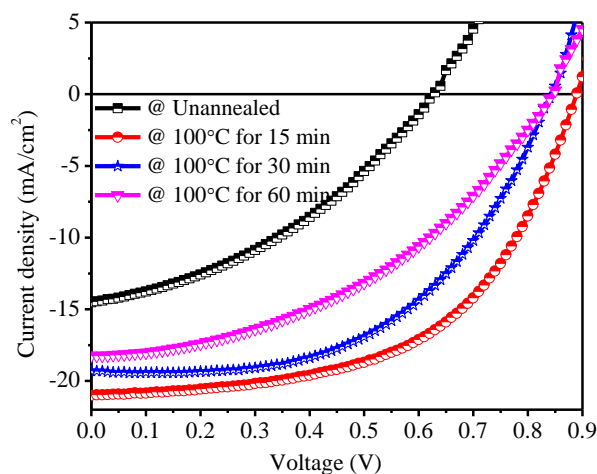


Figure 4.10 J-V characteristics of perovskite solar cells with and without annealing of absorber layer from sequential deposition method in forward scan.

This increase in barrier reduces the recombination of electrons from  $TiO_2$  and holes from perovskite layer by the introduction of lead iodide ( $PbI_2$ ) between  $TiO_2$  and perovskite. But, when further increasing annealing time to 30 min and 60 min, the grain boundary potential increases to 0.395 eV and 0.386 eV, respectively. This caused the decrease of solar cell performance when increasing annealing time to 30 min and 60 min.

Table 4.4 Photovoltaic parameters of the perovskite solar cells annealed at 100°C for different time of 15 min, 30 min and 60 min respectively from sequential deposition method

Device	J <sub>sc</sub>		V <sub>oc</sub>		FF		η%	
	Fwd	Rev	Fwd	Rev	Fwd	Rev	Fwd	Rev
0 min	14.51 ±0.15	14.21 ±0.15	0.63 ±0.02	0.58 ±0.02	0.37	0.44	3.45 ±0.10	3.65 ±0.10
15 min	21.00 ±0.44	21.88 ±0.44	0.89 ±0.01	0.91 ±0.01	0.55	0.57	10.35 ±0.52	11.39 ±0.52
30 min	19.44 ±0.35	20.14 ±0.35	0.84 ±0.01	0.87 ±0.01	0.53	0.52	8.71 ±0.26	9.23 ±0.26
60 min	18.23 ±0.15	18.54 ±0.15	0.85 ±0.03	0.79 ±0.03	0.42	0.42	6.6 ±0.21	6.17 ±0.21

(Fwd=forward scan and Rev= Reverse scan).

It is important to note that the perovskite composition may be different as the conversion time of PbI<sub>2</sub> to MAPbI<sub>3</sub> is different for bulk PbI<sub>2</sub> on top of compact TiO<sub>2</sub> compared to PbI<sub>2</sub> dispersed on mesoporous TiO<sub>2</sub>. Figure 4.10 and 4.11 shows J-V characteristics of perovskite solar cell with and without annealing of absorber layer from sequential deposition and single step method. The solar cell efficiency of perovskite film annealed at 100 °C for 15 min is highest among all devices (Table 4.4 and 4.5). Increase in performance is due to the reduced recombination of electrons from TiO<sub>2</sub> and holes from perovskite layer by the introduction of lead iodide (PbI<sub>2</sub>) between TiO<sub>2</sub> and perovskite. Perovskite (CH<sub>3</sub>NH<sub>3</sub>PbI<sub>3</sub>) films have defects in surface and within grain boundaries. Annealing for 15 min at 100°C will decompose the surface of perovskite (CH<sub>3</sub>NH<sub>3</sub>PbI<sub>3</sub>) films to form small amount of PbI<sub>2</sub> which reduces the recombination yielding high device efficiency.

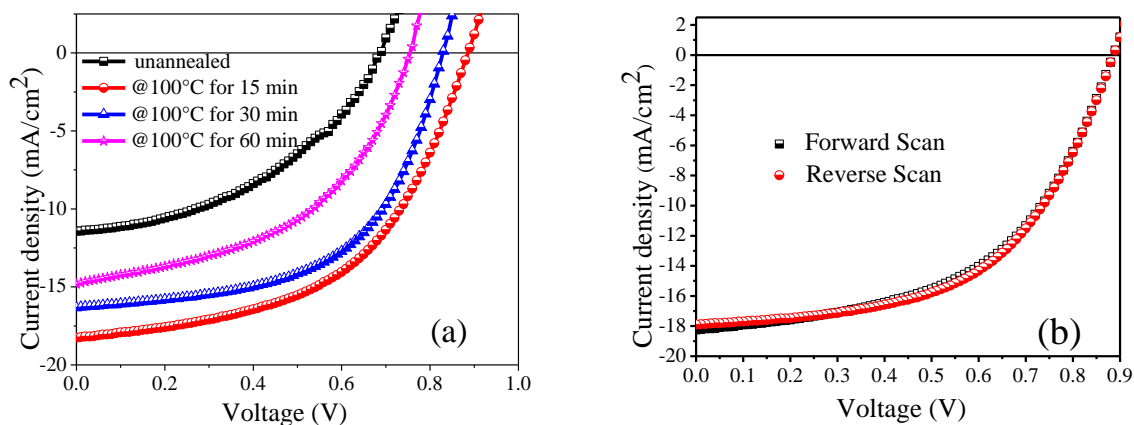


Figure 4.11 J-V characteristics of Perovskite solar cell with and without annealing of absorber layer from single step method (a) forward scan (b) forward and reverse scan for perovskite solar cells prepared from annealing at 100°C for 15 min

Figure 4.11 and Table 4.5 show the J-V characteristics of perovskite solar cells with and without annealing of absorber layer from single step method, in which similar trends were observed that device efficiency increases to 15 min annealed sample and then decreases for 30 min and 60 min annealing. It has been found that the unannealed sample with lower performance has larger hysteresis compared to the device annealed at 100°C for 15 min for both deposition techniques. The average low efficiency of perovskite film prepared from single step method is due to incomplete coverage of the film as shown in Fig. 4.2.

Table 4.5 Photovoltaic parameters of the perovskite solar cells annealed at 100°C for different time from single step method

Device	J <sub>sc</sub>		V <sub>oc</sub>		FF		η%	
	Fwd	Rev	Fwd	Rev	Fwd	Rev	Fwd	Rev
0 min	11.42 ±0.10	11.62 ±0.10	0.69 ±0.04	0.60 ±0.04	0.43	0.38	3.41 ±0.38	2.65 ±0.38
15 min	18.25 ±0.18	17.89 ±0.18	0.89 ±0.01	0.89 ±0.01	0.51	0.54	8.44 ±0.12	8.69 ±0.12
30 min	16.33 ±0.12	16.08 ±0.12	0.83 ±0.005	0.84 ±0.005	0.56	0.58	7.60 ±0.19	7.98 ±0.19
60 min	14.81 ±0.04	14.72 ±0.04	0.75 ±0.03	0.69 ±0.03	0.48	0.43	5.36 ±0.50	4.36 ±0.50

#### 4.1.9 Charge carrier life time, charge transport time and total charge carrier density of Perovskite solar cell from Sequential Deposition Method

Figure 4.12a shows transient photovoltage (TPV) measurements of perovskite solar cells with un-annealing and annealing at 100°C for 15 min, 30 min and 60 min, respectively from sequential deposition method. The cells were kept under open circuit conditions using high input impedance (1 MΩ). The cells were also constantly illuminated by the background light with intensity of 1.5 suns from an external halogen lamp source. As the background light intensity is at steady state at 1.5 suns, the TPV decay does not fall to zero level as shown in Fig. 4.12a. The reason that TPV does not decay to the same value in the normalized curves is that the different solar cells have different open circuit voltage at steady state conditions. Charge carrier life times of 32.2 μsec, 40 μsec, 1.4 μsec and 9.3 μsec were found for perovskite solar cells with un-annealing and annealing at 100°C for 15 min, 30 min and 60 min, respectively. Charge carrier life time is the longest at 40 μsec for 15 min annealing at 100°C, then decreases with longer annealing time. This is consistent with the highest J<sub>sc</sub> for 15 min annealing at

100°C. The voltage decay in transient photovoltage (TPV) acquired by using 1 M $\Omega$  input impedance of oscilloscope and is given by

$$\Delta V = V_{oc} + \Delta V_o \exp(-t/\tau) \dots\dots\dots(I)$$

Where  $\tau$  is the charge carrier life time and  $V_{oc}$  is the open circuit voltage.

Figure 4.12b shows transient photocurrent (TPC) measurements of perovskite solar cells with un-annealing and annealing at 100°C for 15 min, 30 min 60 min, respectively from sequential deposition method. In transient photocurrent technique, the charge collection time is measured by the short lived photogenerated charge carrier decay while keeping the cell under short circuit conditions.

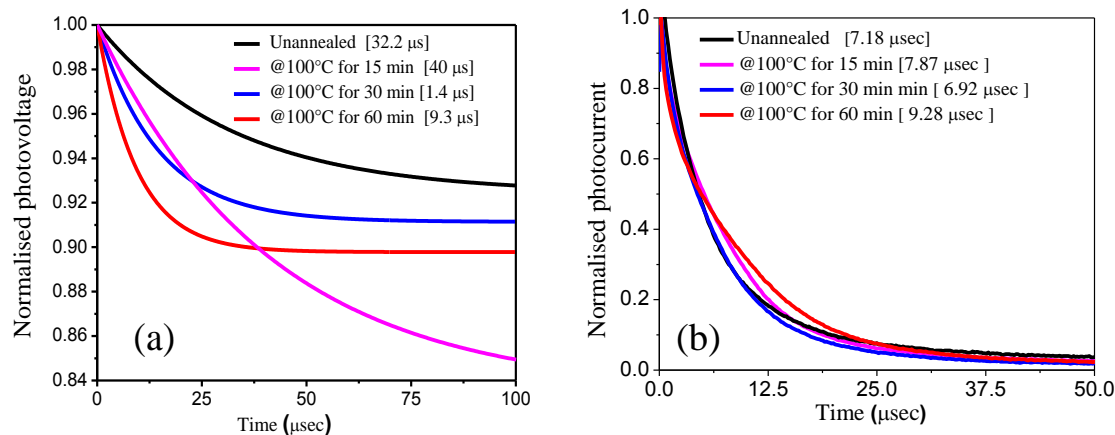


Figure 4.12 (a) Transient photovoltage decay and (b) transient photocurrent decay of Perovskite solar cells from sequential deposition method. The values in the parenthesis show charge carrier lifetime and charge carrier transport time obtained by fitting the decay function with mono-exponential equation with fitting error less than  $10^{-7}$  sec in (a) open circuit condition and (b) short circuit condition.

The short lived photocurrent is generated by a nanosecond pulse of a dye laser incident on solar cells under short circuit conditions (by shunting across a very low



resistor at 20  $\Omega$ ). No background light was applied while measuring TPC. This is the reason when pulse laser was off, the TPC decays reach to zero for all samples. It was found that the value of charge transport time of 7.18  $\mu\text{sec}$ , 7.87  $\mu\text{sec}$ , 6.92  $\mu\text{sec}$  and 9.28  $\mu\text{sec}$  for perovskite solar cells with un-annealing and annealing at 100°C for 15 min, 30 min 60 min, respectively. All the devices show shorter charge transport time than charge carrier life time (recombination time) making efficient charge extraction in the prepared perovskite solar cells.

Figure 4.13 shows (a) intensity dependence and (b) charge carrier density dependence with charge carrier life time in perovskite solar cells for different annealing time (e.g., 15, 30 and 60 min) from sequential deposition method. Intensity dependent transient measurements were performed by constantly illuminating an external halogen lamp source via varying the background white intensity from 0 suns to 1.5 suns with interval of 1/12 suns. In this case, when a short pulse (1 ns) of light is incident, the dependence of charge carrier lifetime on charge carrier concentration is obtained. The charge carrier concentration was varied using different intensities (0 to 1.5 suns with interval of 1/12 suns) of the white light source. The charge carrier density concentration was correlated with the charge carrier lifetime. At higher light intensity, more electrons and holes are generated, which increases the probability of recombination and decreasing carrier lifetime. The carrier lifetime is longer for 15 min annealing samples than 30 min and 60 min annealing films at different light intensity and charge carrier density. This is consistent with transient photovoltage measurements and JV curves, supporting that the highest performing cells were annealed at 100°C for 15 min.

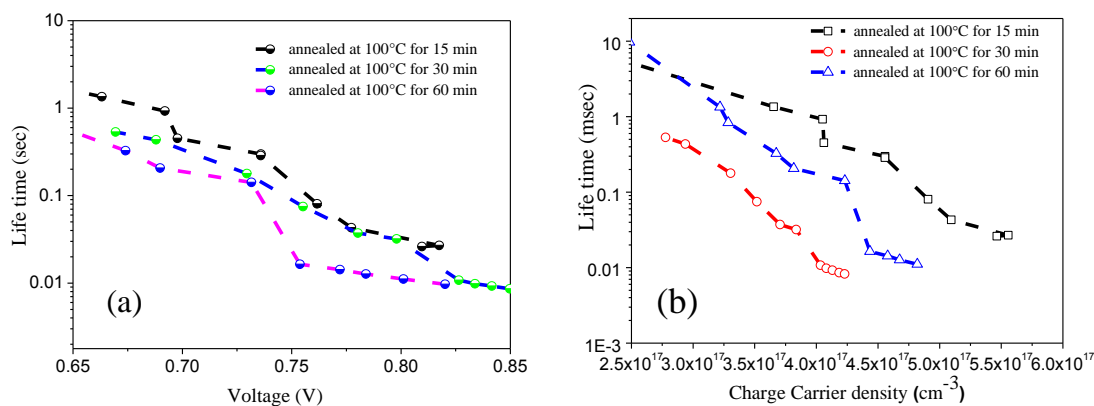


Figure 4.13 (a) Intensity dependence and (b) charge carrier density dependence life time in perovskite solar cells for different annealing time (15, 30 and 60 min) from sequential deposition method.

## 4.2 Effect of adding water in CH<sub>3</sub>NH<sub>3</sub>I solution for the preparation of Perovskite Solar Cell from Sequential Deposition Method

### 4.2.1 UV-Vis spectra of annealed Perovskite films

Figure 4.14 shows UV-Vis spectra of perovskite film prepared from 0%, 1%, 3%, 5%, and 7% water in a MAI solution. The films of lead iodide (PbI<sub>2</sub>) were coated onto a ca. 600 nm thick mesoporous TiO<sub>2</sub> layer from 462 mg/ml solution of PbI<sub>2</sub> in DMF. The PbI<sub>2</sub> coated films were dried at 70 °C for 30 min on a hot plate. After this, the films were dipped in a MAI solution with 0%, 1%, 3%, 5%, and 7% water for 50 sec. The as-casted films were annealed at 100 °C for 15 min. All the films were prepared in exactly the same condition as followed during the device fabrication. The CH<sub>3</sub>NH<sub>3</sub>PbI<sub>3</sub> film shows a broad absorption across the visible region with two prominent peaks at 470 nm and 790 nm in absorption spectra. The absorbance of perovskite film increases with increasing water

concentration in MAI solution from 0% to 1%, 3%, 5% and highest for 5% water in MAI solution. This could be attributed to the fact that 5% of water is just enough to solvate the methylammonium and provides great diffusion mobility to form perovskite phase. The absorbance of the perovskite film is the highest for films prepared from 5% water in MAI solution. Previous report showed that a crystallization of perovskite happens when exposed to moisture as the water solvates the methylammonium and provides high diffusion mobility to form the perovskite phase [43, 91]. To further understand the role of water in the MAI solution, the concentration of water was further increased from 5% to 7% and the absorbance decreased significantly. The reason is that the excess amount (> 5%) of water in MAI solution can dissociate  $\text{CH}_3\text{NH}_3\text{PbI}_3$  into  $\text{PbI}_2$  and  $\text{CH}_3\text{NH}_3\text{I}$ . This is further confirmed by the measurements of XRD and AFM that will be discussed later.

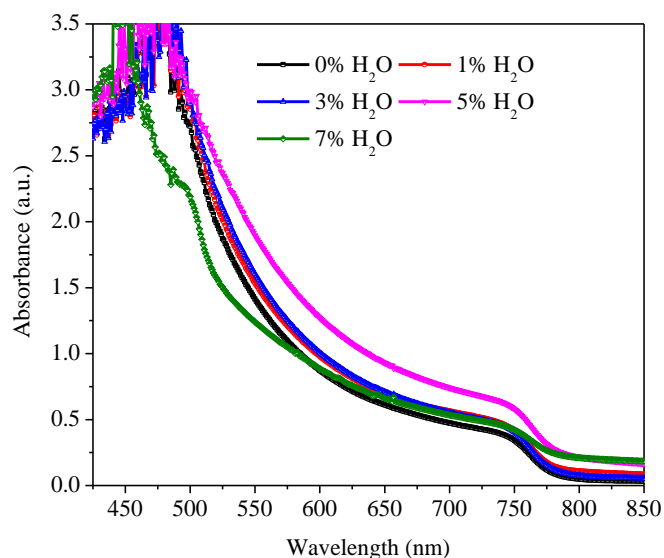


Figure 4. 14 UV-Vis spectra of annealed perovskite films prepared from 0%, 1%, 3%, 5%, and 7% water in MAI solution, respectively.

#### 4.2.2 SEM images of Perovskite film

Figure 4.15 shows SEM images of perovskite films prepared from 0%, 1%, 3%, 5% and 7% water in MAI solution from sequential deposition method. The SEM images clearly shows that the perovskite film prepared from 5% volume of water by IPA has the largest grain size. The increase in grain size reduces the overall grain boundary area suppressing the recombination within the bulk of the materials. These SEM results are in agreement with AFM, XRD and UV-VIS spectrum.

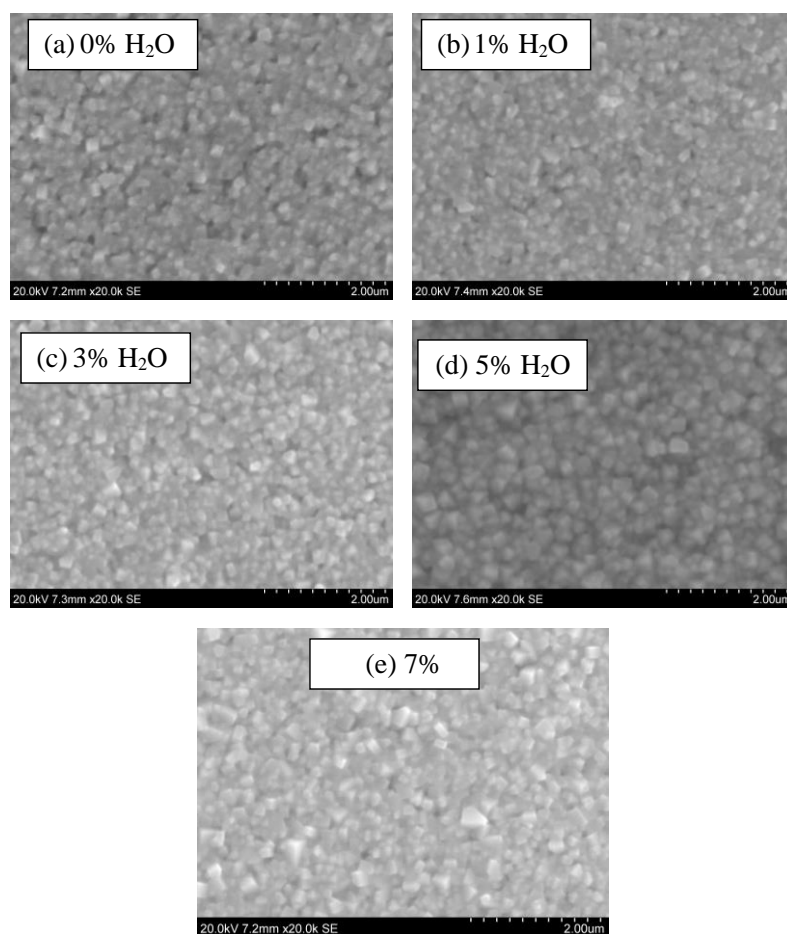


Figure 4. 15 SEM images of Perovskite film prepared from 0%, 1%, 3%, 5% and 7% water in MAI solution from sequential deposition method

### 4.2.3 XRD spectra of annealed Perovskite films

The perovskite crystal structure can be described by the general formula  $ABX_3$  where A and B are cations and X is an anion. The perovskite crystal structure discussed here is  $CH_3NH_3PbI_3$  where A =  $CH_3NH_3$ , B = Pb and X = I. These crystals are held together by ionic interactions between organic and inorganic part and by hydrogen bond [2, 92]. XRD patterns were recorded to understand the effect of water in the MAI solution. Dip coating was done outside the glove box with a relative humidity of 40%. Figures 4.16 and 4.17 show XRD patterns of annealed and unannealed perovskite films prepared from 0%, 1%, 3%, 5%, and 7% water in the MAI solution. The XRD samples were prepared in the same conditions as for UV-Vis absorption measurements. The strong Bragg peaks at  $14.08^\circ$ ,  $28.41^\circ$ ,  $31.85^\circ$ , and  $43.19^\circ$  are assigned to (110), (220), (310), and (330) of  $CH_3NH_3PbI_3$ . These structures correspond to tetragonal  $I4cm$  crystal structure of halide perovskite with high crystallinity [7, 87]. The peak at  $12.12^\circ$  is assigned to (001) of  $PbI_2$  and corresponds to incomplete conversion of  $PbI_2$  to perovskite. This  $PbI_2$  phase was previously reported from the sequential deposition method [7, 10, 45].

Remarkably, the diffractograms (figure 4.16) do not show significant increase in  $PbI_2$  phase for perovskite films when prepared with water content increasing from 0%, 1%, 3%, to 5% in the MAI solution. However, a strong  $PbI_2$  peak was observed with perovskite film prepared from the 7% water in the MAI solution. Methylammonium lead iodide perovskite film is formed with the intercalation of methylammonium ions into the lattice space of  $PbI_2$ . If the film is exposed to excess water, dissolution of the polar organic  $CH_3NH_3^+$  in the perovskite structure occurs that results in dissociation of

perovskite into  $\text{PbI}_2$  and  $\text{CH}_3\text{NH}_3\text{I}$  [93]. The XRD peaks of annealed perovskite films prepared from 1%, 3% and 5% water are higher than those in the 0% water in MAI solution. Crystallinity of perovskite increases after increasing the water concentration up to 5% in the MAI solution. The (110) peak of perovskite phase prepared from 5% water increases to 2.82 (table 4.6) from 2.02 corresponds to 0% water in MAI solution. This shows that an optimum amount of water facilitates crystallization of perovskite films in the (110) plane. It is shown that the interaction between  $\text{MAPbI}_3$  and water is critical as moisture has been shown to affect the crystallization dynamics and growth of perovskite films [47, 94-96]. It was found that crystallinity of perovskite increased when the perovskite films were exposed to water molecules under high humidity conditions. Water molecules can penetrate across the perovskite structure to form a partly reactive phases  $[\text{CH}_3\text{NH}_3\text{PbI}_3 \cdot \text{H}_2\text{O}$  and  $(\text{CH}_3\text{NH}_3)_4\text{PbI}_6 \cdot 2\text{H}_2\text{O}]$ . These reactive phases are metastable form that spontaneously dehydrates in air forming perovskite phases. These hydrated phases are formed due to water incorporation into the perovskite lattice by the formation of hydrogen bonds between water molecules and lattice iodides, as well as from hydrogen bonding interaction between MA cations and water molecules. Thus, adding water as additives expanded the volume of Perovskite films[43]. Water can improve the growth of Perovskite films from the interaction between  $\text{H}_2\text{O}$  and  $\text{MAPbI}_3$ , such as hydrogen bonding interaction. This is also supported from AFM topography images discussed later which show increase in roughness of films prepared by adding water in MAI solution suggesting volume expansion leading to formation of large grains of perovskite.

In addition, lower boiling point and higher vapor pressure of water speeds up the crystallization of perovskite with larger crystals[97]. The XRD pattern show that the

perovskite film formation is facilitated by adding 5% water in MAI solution. However, with higher percentage ( $> 5\%$ ) of water in MAI solution retards the perovskite formation. It is also found that when the water concentration is increased beyond 10%, the film is completely covered with  $\text{PbI}_2$ . Therefore, the water helps to speed up the formation of perovskite crystallization with the largest grains while adding 5% water in MAI solution. However, it slows the formation of perovskite with adding water beyond 5% in MAI solution for sequential deposition method.

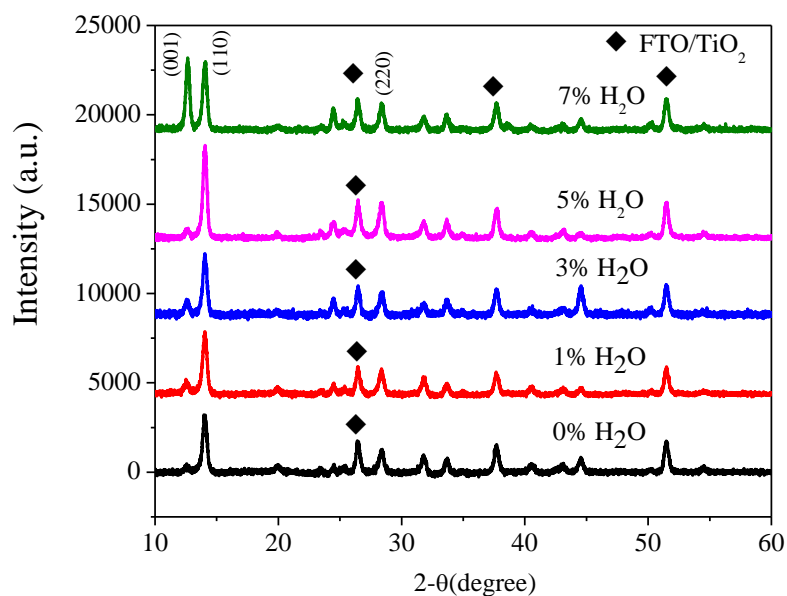


Figure 4. 16 XRD spectra of annealed perovskite films prepared from 0%, 1%, 3%, 5%, and 7% water in the MAI solution

When there is sufficient amount of water molecules in the solution, the perovskite readily forms bonding with single molecule of water which crystallizes upon exposure to air. The FTO peak intensity was taken as reference. Therefore, the absolute peak intensity of (110) plane corresponds to perovskite with reference to FTO can be compared. By comparing the FWHM of (110) peak of perovskite phase in table 4.6, it can be seen that

the perovskite film prepared with 5% water in MAI solution has the narrowest FWHM value (0.379) indicating the highest crystallinity of perovskite phase in the (110) plane. However, the FWHM of (220) phase of perovskite does not change significantly because of the higher surface and interfacial energy in the (220) plane [98].

Table 4.6 Full width half maximum (FWHM) and peak intensity of annealed perovskite films prepared from 0%, 1%, 3%, 5%, and 7% water in the MAI solution obtained from XRD spectra.

Sample	FWHM		Peak Intensity		Peak Intensity (Reference)	Ratio of Perovskite peaks with FTO
	(110) peak	(220) peak	(110) peak	(220) peak	FTO at $2\theta=26.43^\circ$	
0% H <sub>2</sub> O	0.412	0.463	3187	1260	1576.98	2.02
1% H <sub>2</sub> O	0.428	0.483	3498	1332	1523.78	2.29
3% H <sub>2</sub> O	0.409	0.447	3411	1364	1379.35	2.47
5% H <sub>2</sub> O	0.379	0.455	5175	1980	1833.25	2.82
7% H <sub>2</sub> O	0.415	0.440	3809	1487	1451.10	2.62

#### 4.2.4 XRD pattern of unannealed Perovskite films

To further understand the role of adding water in the MAI solution on perovskite crystallization, XRD pattern were measured on unannealed perovskite films made by dipping PbI<sub>2</sub> films in 0%, 1%, 3%, 5%, and 7% water in the MAI solution. The XRD measurements of unannealed samples were performed to exclude the annealing effects on crystallization and investigate only the effects of adding water into the MAI solution on the perovskite crystallization. Figure 4.17 shows that there is no observable change in XRD spectra by increasing the water concentration from 0% to 3% in the MAI solution.



However, the perovskite phase (110) increases with increasing water content from 3% to 5% and 7% in MAI solution. This is in agreement with the full width at half maximum (FWHM) of (110) peak as shown in Table 4.7. The FWHM of perovskite phase is the lowest for perovskite film prepared from 5% (FWHM=0.394) and 7% (FWHM=0.391) water content in the MAI solution.

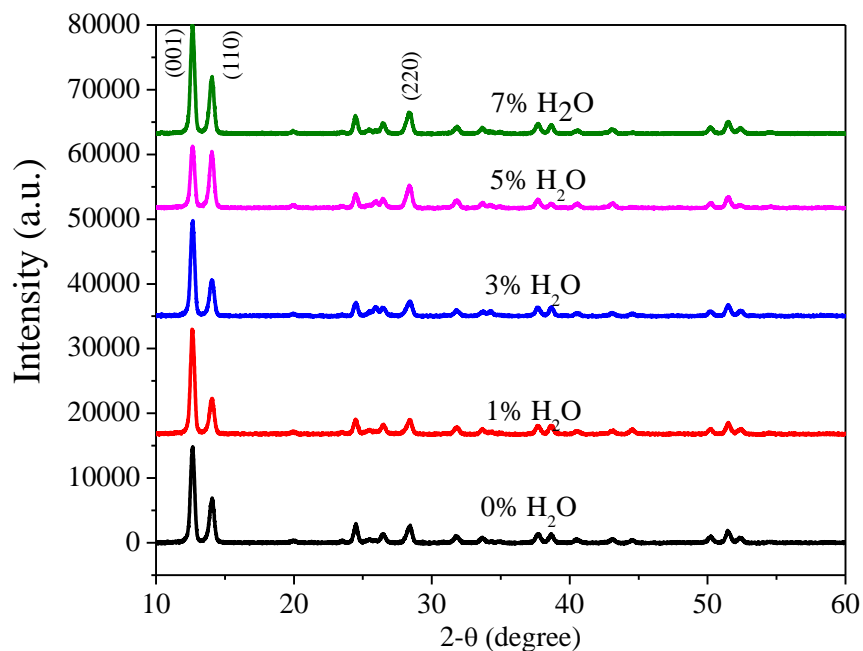


Figure 4.17 XRD pattern of unannealed perovskite films prepared from 0%, 1%, 3%, 5%, and 7% water in MAI solution

The perovskite phase (110) /  $\text{PbI}_2$  crystallinity (001) ratio for 5% water content is higher than that of 7% water content. Therefore, the perovskite film prepared from 5% water content in the MAI solution has the highest (0.93) perovskite/ $\text{PbI}_2$  crystallinity ratio, indicating that the most amount of  $\text{PbI}_2$  is converted into perovskite phase with 5% water content. This is similar to the increase in crystallinity of annealed perovskite film prepared from 5% water in the MAI solution. The addition of 5% water can facilitate reaction between  $\text{PbI}_2$  phase and methyl ammonium iodide and form metastable

monohydrate phase that instantaneously converts to perovskite when exposed to air [10, 29]. When the water content was further increased from 5% to 7% in the MAI solution, the  $\text{PbI}_2$  (001) peak also increases significantly. This is due to the dissolution of the perovskite with excess water present in the MAI solution. Therefore, XRD spectra of unannealed and annealed perovskite films demonstrate that 5% is an optimal amount of water that can help to crystallize perovskite phase in the (110) plane. The ratio between the peaks of (110) and (220) in perovskite increases with higher content of water in the MAI solution. The higher value in (110) plane suggests more grain growth in the (110) plane. This may be due to lower surface and interfacial energy in the (110) plane [99].

Table 4.7 Full width half maximum (FWHM) and peak intensity of unannealed perovskite films prepared from 0%, 1%, 3%, 5% and 7% water in the MAI solution obtained from XRD.

Sample	FWHM		Peak Intensity			Ratio of Perovskite : $\text{PbI}_2$ peak
	(110) peak	(220) peak	(001) peak	(110) peak	(220) peak	
0% $\text{H}_2\text{O}$	0.401	0.453	14791	6909	2694	0.46
1% $\text{H}_2\text{O}$	0.404	0.459	15241	5497	2227	0.36
3% $\text{H}_2\text{O}$	0.406	0.504	14722	5522	2265	0.37
5% $\text{H}_2\text{O}$	0.394	0.486	9355	8733	3443	0.93
7% $\text{H}_2\text{O}$	0.391	0.476	16834	8792	3294	0.19

#### 4.2.5 AFM topographic images of annealed Perovskite films

To further study the effects of dipping  $\text{PbI}_2$  film in the MAI solution with 0%, 1%, 3%, 5% and 7% water concentrations and understand distinct changes in absorption spectra and XRD patterns, morphology of such films were measured using atomic force microscopy (AFM). All AFM samples were prepared in the same processing conditions as the UV-Vis and XRD measurements. Figures 4.18(a-e) show AFM images of annealed

perovskite films prepared from 0%, 1%, 3%, 5%, and 7% water in the MAI solution. The AFM images show that the grain size of perovskite films increases from 171 nm for 0% water (Fig. 4.18a) to 630 nm for 5% water (Fig. 4.18d) in the MAI solution.

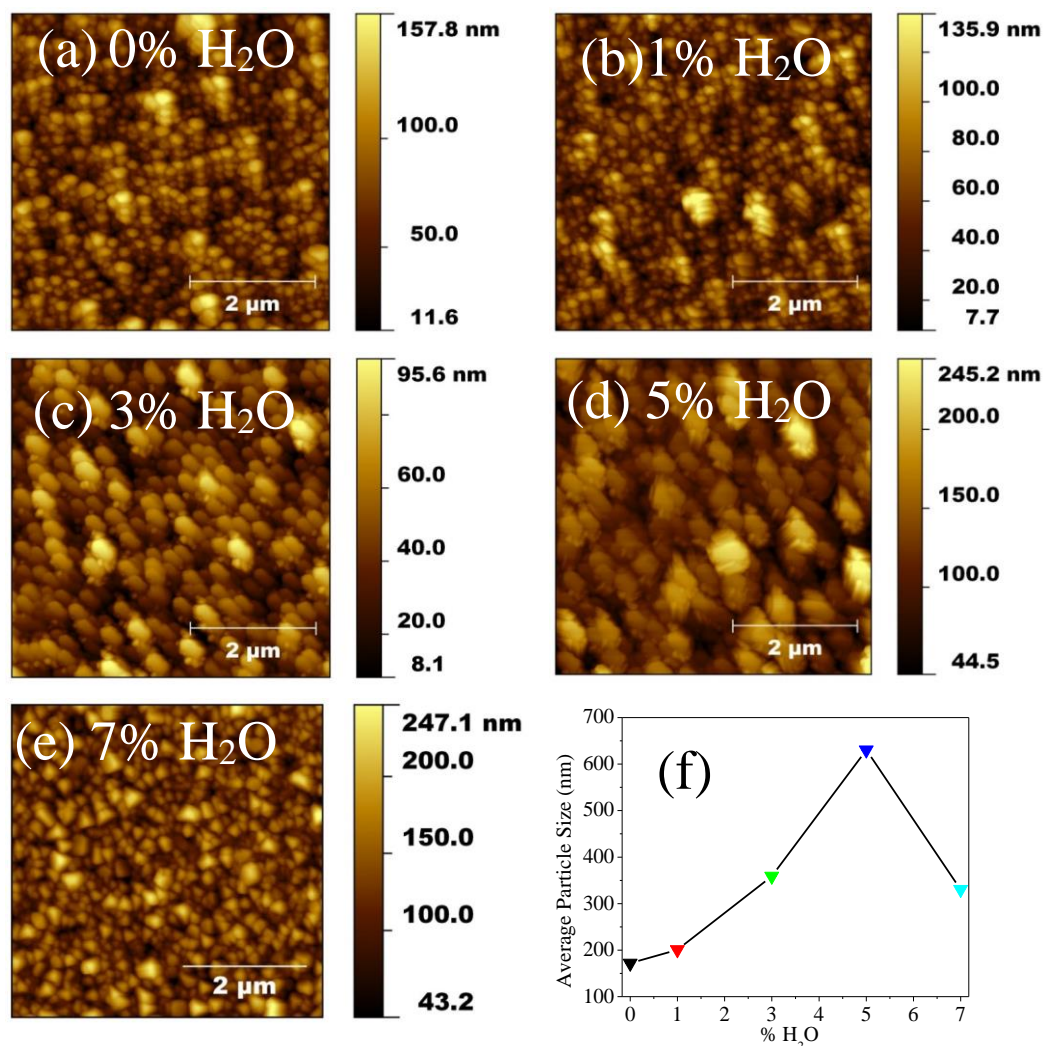


Figure 4.18 AFM images of annealed Perovskite films prepared from (a) 0%, (b) 1%, (c) 3%, (d) 5%, and (e) 7% water in the MAI solution; and (f) average particle size vs water concentration.

This is further confirmed by the topography line profile (Fig. 4.19). However, further increase of water concentration to 7% (Fig. 4.18e) provides excess water that

causes dissolution of large crystals, leading to an average grain size of 330 nm. There is a slight increase of grain size in perovskite films made from 0% water (171 nm, Fig. 4.18a) to 1% water (200 nm, Fig. 4b). After increasing the water concentration to 3% (fig. 4.18c), the grain size increases to 358 nm, which can be seen in fig. 4.18f with average particle size calculated using Pico View software and plotted against water concentration. Increase in grain size with higher water concentration may be due to combined effects of crystallization of perovskite film by water molecule and annealing [91, 94].

During crystallization of perovskite films, the average size of remaining grains (fig. 4.18d) increases by the motion of grain boundaries resulting in shrinkage and elimination of small grains, which reduces the total grain boundary area[42, 100]. This is most clearly seen for perovskite films prepared by dipping  $\text{PbI}_2$  layer in the 5% water MAI solution. The perovskite phase undergoes a crystallization process with large grain size and volume expansion after increasing the water concentration to 5% in the MAI solution, which is similar to the crystallization of  $\text{CH}_3\text{NH}_3\text{PbI}_3$  under 90% RH reported by Jeffrey et al. [2]

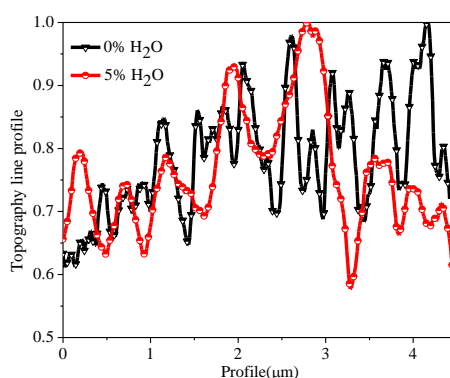


Figure 4.19 Topography line profile of annealed perovskite film prepared from 0% and 5% water in MAI solution from sequential deposition method

This will decrease in total number of trap sites and defect density along the grain boundary and reduce the recombination of photogenerated charge carriers, which will be

demonstrated using transient photovoltage measurement later. Figure 4.19 shows the topography line profile of annealed perovskite film prepared from 0% and 5% water in MAI solution. The line profile shows that the grain size of perovskite film prepared from 5% water in MAI solution is higher than the grain size of perovskite film prepared from 0% water in MAI solution.

#### 4.2.6 AFM topographic images of unannealed Perovskite film

AFM images of unannealed perovskite films were also measured to understand the role of water in the MAI solution on the formation of perovskite. Figure 4.20 shows AFM topography images of unannealed perovskite films prepared from 0%, 1%, 3%, 5%, and 7% water in the MAI solution. The reason for measuring the morphology of unannealed perovskite films is to exclude the effect of annealing on the grain size but only study the effect of adding water in the MAI solution. The grain size of perovskite film increases from 108 nm for 0% (Fig. 4.20a) to 148 nm for 1% (Fig. 4.20b) and to 220 nm for 3% (Fig. 4.20c) water. This is further confirmed by the topography line profile shown in Fig 4.21. However, it increases significantly when the water concentration increases from 3% to 5% and 7%. The grain size of perovskite films increases from 220 nm for 3% (Fig. 4.20c) water to 391 nm for 5% (Fig. 4.20d) water, but decreased to 346 nm for 7% (Fig. 4.20e) water in the MAI solution. Figure 4.20f further confirms the increase of the average grain size with higher water content up to 5% but decreased when water content reached 7%.

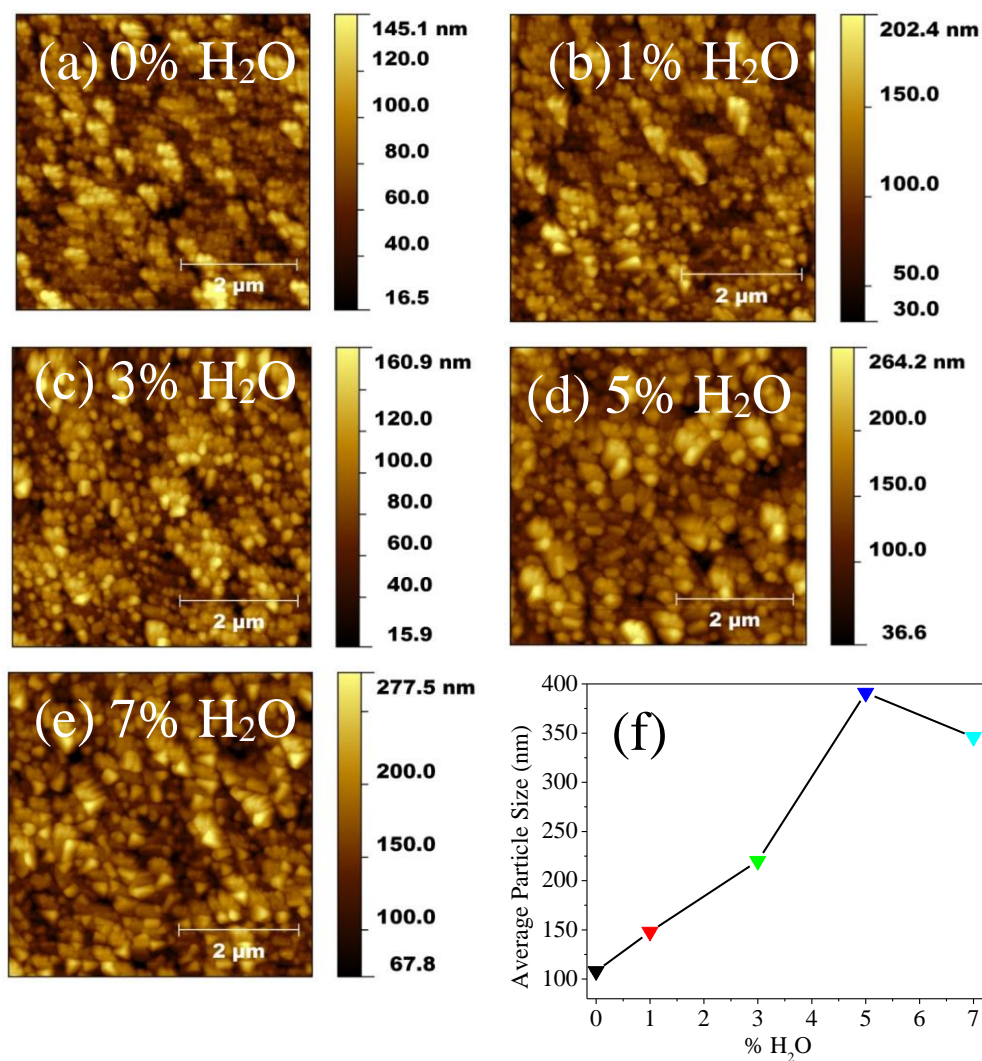


Figure 4.20 (a) – (e) AFM images of unannealed perovskite films prepared from 0%, 1%, 3%, 5% and 7% water in the MAI solution, (f) average particle size vs water concentration in the MAI solution.

The increase in grain size compared to the 0% water perovskite film may be due to the volume expansion during the crystal growth from  $\text{PbI}_2$  to perovskite by the intercalation of  $\text{CH}_3\text{NH}_3^+$  as well as rearrangement of aggregated structure of  $\text{PbI}_2$  driven by minimizing the grain boundary energy[42, 94]. Similar results have been obtained with SEM images shown in Fig. 4.15. The SEM images show that perovskite films have the largest grain size after adding 5% water in MAI solution. The morphology of

perovskite films with 0% H<sub>2</sub>O and 1% H<sub>2</sub>O in MAI looks similar except for more visible gaps in the perovskite film from 0% H<sub>2</sub>O in MAI solution.

After increasing the water concentration to 3% H<sub>2</sub>O in MAI solution, the grain size of perovskite film was found to increase. Such an improvement in morphology has also been shown using different additives [36, 101, 102].

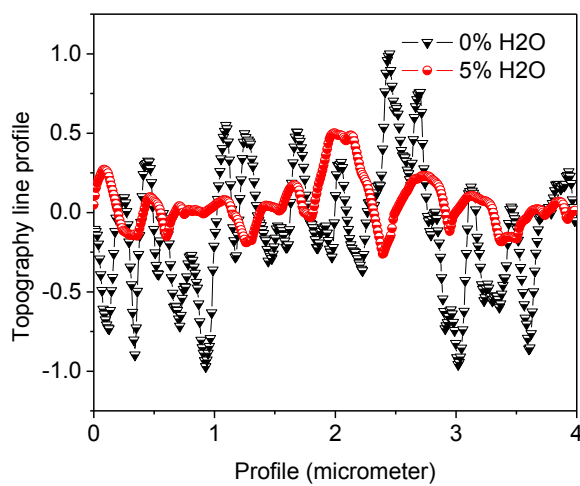


Figure 4. 21 Topography line profile of unannealed perovskite film prepared from 0% and 5% water in MAI solution from sequential deposition method

The grain size reached the largest at 5% water, and then decreased with 7% water in MAI solution. Figure 4.21 shows the topography line profile of unannealed perovskite film prepared from 0% and 5% water in MAI solution. The line profile shows that the grain size of perovskite film prepared from 5% water in MAI solution is higher than the grain size of perovskite film prepared from 0% water in MAI solution.

#### 4.2.7 Surface potential distribution of annealed Perovskite film

Figure 4.22 shows the nanoscale surface potential distribution of perovskite films prepared from 0%, 1%, 3%, 5%, and 7% water content in the MAI solution. The surface potential distributions were acquired from KPFM images shown in Fig. 4.23. The surface

potential of perovskite films prepared from 1%, 3%, 5%, and 7% water content in the MAI solution were higher compared to 0% water in MAI solution. The average surface potential of perovskite films increases with increasing the amount of H<sub>2</sub>O in MAI solution till 5% and decreases with increasing beyond 5% H<sub>2</sub>O in MAI solution. This is due to the reduced surface defects which act as traps for electrons caused by dangling bonds. This may be due to doping of water during perovskite film formation which helps for reconstruction of the perovskite surface reducing structural defects in the surface.

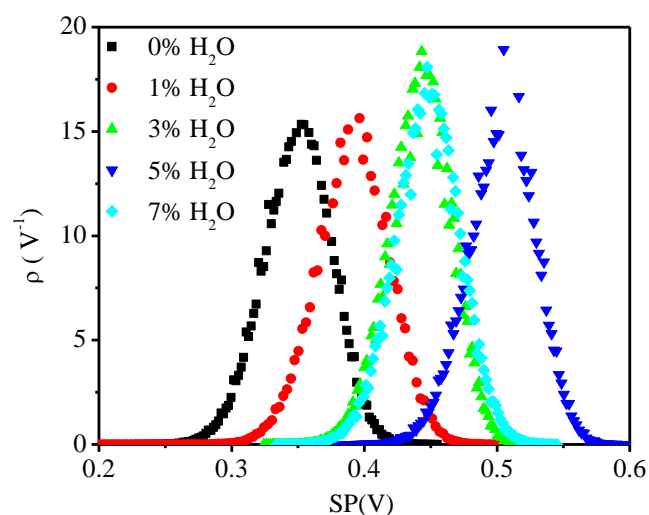


Figure 4.22 Nanoscale surface potential distribution of Perovskite films prepared from 0%, 1%, 3%, 5%, and 7% water in the MAI solution



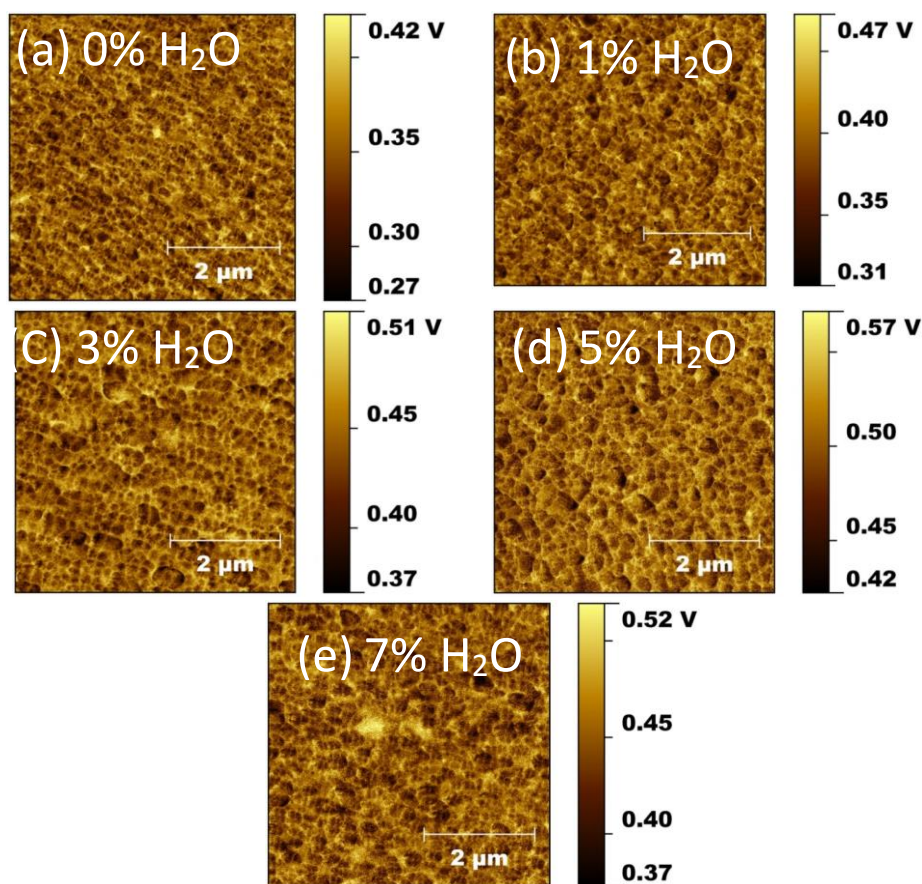


Figure 4.23 Surface potential images of perovskite films prepared from 0%, 1%, 3%, 5% and 7% water in MAI solution from sequential deposition method.

It was previously reported that the origin of dangling bonds is due to the exposed iodine atoms in perovskite film[13, 14]. Figure 4.23 shows Kelvin probe force microscopy (KPFM) images of Perovskite films prepared from 0%, 1%, 3%, 5% and 7% water in MAI solution from sequential deposition method. KPFM images of perovskite films demonstrates higher surface potential at the grain boundaries (GBs) than within grains giving downward band bending in the energy band diagram leading to the minority carrier electrons in p-type absorber layer to be attracted towards GBs. Average potential

of the perovskite solar cells prepared from 5% water in MAI solution gives highest surface potential showing reduced surface defects in the prepared perovskite films.

#### 4.2.8 Current density-voltage (J-V) curves of Perovskite Solar Cells

Figure 4.24 shows current density-voltage (J-V) curves of perovskite solar cells with device structure of FTO/c-TiO<sub>2</sub>mesoporous-TiO<sub>2</sub>/CH<sub>3</sub>NH<sub>3</sub>PbI<sub>3</sub>/Ag using 0%, 1%, 3%, 5%, and 7% water content in the MAI solution. The perovskite films were deposited by two step method: first PbI<sub>2</sub> film was spin coated and dried. Second, the films were dipped in 10 mg/ml MAI solution which contained different concentration (0 - 7 %) of water by IPA volume. Device performance of prepared cells were measured under 100 mW/cm<sup>2</sup> AM 1.5 simulated solar irradiation with a humidity of 40%. The scan rate was kept constant for all devices with 0.5 V/sec. The cells were characterized both in forward and reverse scan (fig. 4.25) due to the JV hysteresis and degradation of the devices while switching the voltage [88].

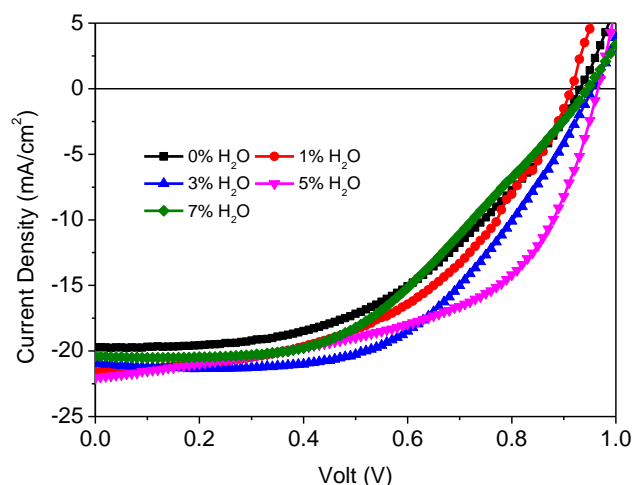


Figure 4.24 Current density-voltage (J-V) characteristics of annealed perovskite solar cells prepared from 0%, 1%, 3%, 5%, and 7% water in the MAI solution

Figure 4.25 JV curves of perovskite solar cells prepared from 0%, 1%, 3%, 5% and 7% water in MAI solution from sequential deposition method in forward and reverse scan. All solar cells with area  $0.16 \text{ cm}^2$  were characterized in the same conditions with  $0.5 \text{ V/sec}$  scan rate in both forward and reverse scan sweeping from 0 to 1V at a relative humidity of 40% in ambient conditions. It can be seen that the efficiency increased when the water concentration increased from 0% to 5% in the MAI solution and decreased when 7% of water was added to the MAI solution. A number of devices were prepared and similar efficiencies were found. Water can weakly bind to methylammonium molecules and form reversible hydrated phase within perovskite, which quickly forms dehydrated perovskite upon exposure to air [2]. An optimal amount of water can solubilize the methylammonium and other components, providing them higher mobility and allowing excess methylammonium to be removed, healing the perovskite structure and fulfilling the deficits and any trap states [91, 94]. Decrease in the trap states results in less non-radiative trap-mediated recombination [2]. Hence, adding an optimal amount of water to the MAI solution leads to improved  $V_{oc}$ , FF and hence overall device performance. The decrease in performance by excess water content is caused by the dissolution of perovskite phase to  $\text{PbI}_2$  and  $\text{CH}_3\text{NH}_3\text{I}$ .

As shown in table 4.8, after adding 1%, 3% and 5% water in the MAI solution, the average photovoltaic efficiencies were improved and reached the highest at 12.42% and 11.74% from forward and reverse scan, respectively, at 5% water based devices. The value of short circuit current density matches closely with integrated  $J_{sc}$  value obtained from external quantum efficiency (EQE) measurement.

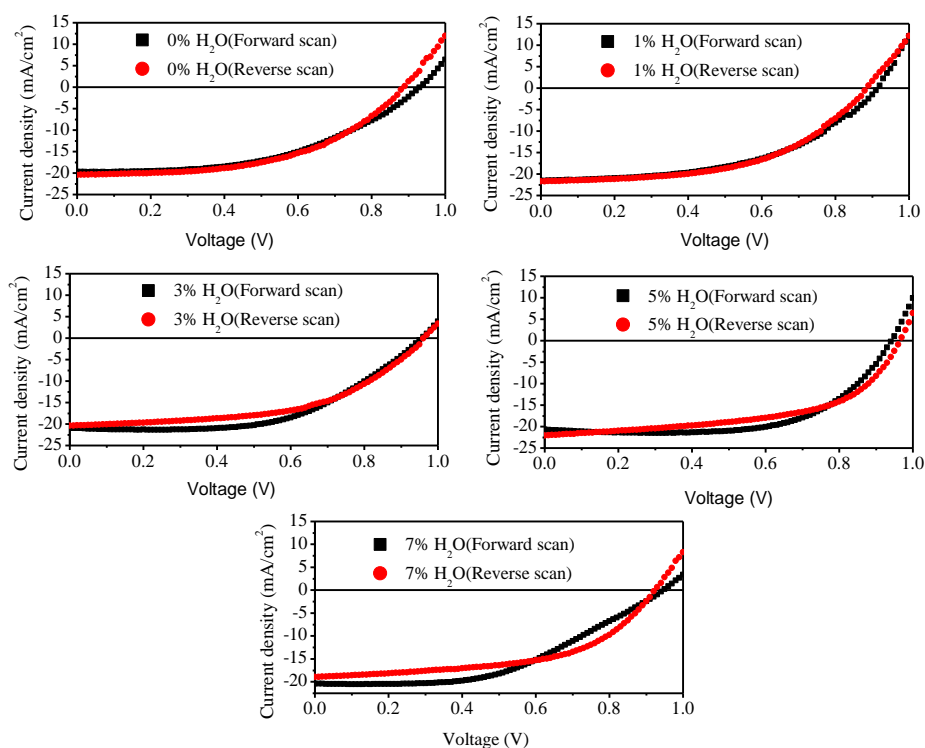


Figure 4.25 JV curves of perovskite solar cells prepared from 0%, 1%, 3%, 5% and 7% water in MAI solution in forward and reverse scan from sequential deposition method.

This is higher than the average efficiencies at 9.04% and 9.25% for perovskite films prepared from 0% water in the MAI solution from forward and reverse scan, respectively. The improvements in short circuit current density ( $J_{sc}$ ) in table 4.8 are due to the increase in absorbance (Fig. 4.14). Increase in fill factor (FF) is due to the formation of high quality film with large grain size.

The increase in open circuit voltage ( $V_{oc}$ ) is caused by the increase in grain size and crystallinity of the perovskite film which reduces the recombination by decreasing trap states and defects within the grain boundary. This is consistent with the charge carrier lifetime obtained from transient photovoltage measurements in fig. 4.27. Such an

increase in  $V_{oc}$  was also observed by Eperon et al. by exposing the perovskite film to humidity for post moisture treatment [91]. Perovskite devices prepared from 1%, 3%, 5% and 7% water in the MAI solution shows increased photovoltaic performance compared to that prepared from 0% water in the MAI solution.

Table 4.8 Photovoltaic parameters for annealed perovskite solar cells made under different concentration of water in the MAI solution

device	$J_{sc}$		$V_{oc}$		FF		$\eta\%$	
	Fwd	Rev	Fwd	Rev	Fwd	Rev	Fwd	Rev
0% H <sub>2</sub> O	19.72	20.41	0.93	0.89	0.49	0.50	9.04	9.25
1% H <sub>2</sub> O	21.57	21.74	0.91	0.89	0.50	0.51	9.87	10.01
3% H <sub>2</sub> O	20.88	20.39	0.96	0.97	0.55	0.52	11.12	10.35
5% H <sub>2</sub> O	20.65	22.06	0.94	0.97	0.64	0.54	12.42	11.74
7% H <sub>2</sub> O	20.38	18.91	0.95	0.93	0.47	0.54	9.29	9.53

#### 4.2.9 Charge carrier lifetime and charge transport time

Figure 4.26 shows transient photocurrent (TPC) measurements of perovskite solar cells prepared from 0%, 1%, 3%, 5% and 7% water in the MAI solution from sequential deposition method. The short lived photocurrent is generated by a nanosecond pulse of a dye laser incident on solar cells under short circuit conditions (by a very low resistor at 20  $\Omega$ ). No background light was applied when measuring TPC. This is the reason when the pulse laser was off, the TPC decays reach to zero for all samples. Charge transport time was obtained by fitting the decay function with mono-exponential equation  $\Delta I_0 \exp(-t/\tau)$  where  $\tau$  is the charge carrier life time. It was found that the values of charge transport time (table 4.9) of 1.39  $\mu\text{sec}$ , 1.54  $\mu\text{sec}$ , 1.64  $\mu\text{sec}$ , 0.998  $\mu\text{sec}$  and 1.88  $\mu\text{sec}$  for perovskite solar cells prepared from 0%, 1%, 3%, 5% and 7% water in the MAI solution, respectively.

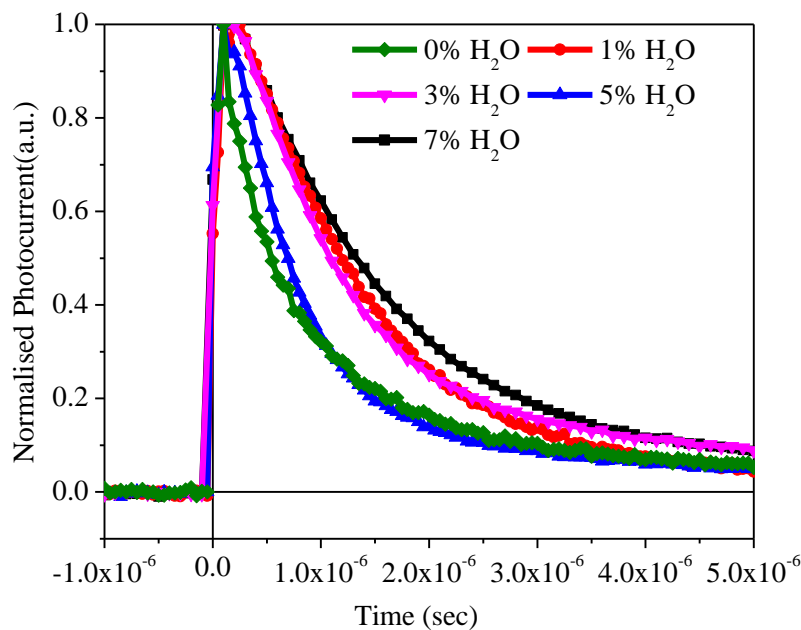


Figure 4.26 Transient photocurrent of annealed perovskite solar cells prepared from 0%, 1%, 3%, 5% and 7% water in the MAI solution.

The charge transport time of perovskite film prepared from 5% water in MAI solution is faster than 0% water in MAI solution showing efficient charge extraction. This is in agreement with the increase in fill factor as shown in table 4.8. However, when the water concentration is increased to 7%, the charge transport time becomes longer which may be caused by the dissociation of  $\text{CH}_3\text{NH}_3\text{PbI}_3$  into  $\text{PbI}_2$  and  $\text{CH}_3\text{NH}_3\text{I}$ . All the devices show shorter charge transport time than charge carrier life time (recombination time) that will be discussed below, making efficient charge extraction in the prepared perovskite solar cells [103].

Table 4.9 Charge transport time for annealed perovskite solar cells made under different concentration of water in the MAI solution.

Device	Charge transport time
0% H <sub>2</sub> O	1.39 $\mu$ sec
1% H <sub>2</sub> O	1.54 $\mu$ sec
3% H <sub>2</sub> O	1.64 $\mu$ sec
5% H <sub>2</sub> O	0.99 $\mu$ sec
7% H <sub>2</sub> O	1.88 $\mu$ sec

Figure 4.27 shows transient photovoltage (TPV) measurements of perovskite solar cells prepared from 0%, 1%, 3%, 5% and 7% water in the MAI solution from sequential deposition method. The cells were kept under open circuit conditions using high input impedance (1 M $\Omega$ ) to approximate open circuit. The cells were constantly illuminated by the background light with intensity of 1.5 suns from an external halogen lamp source. As the background light intensity is at steady state at 1.5 suns, the TPV decay does not fall to zero level as shown in Fig. 4.27. In addition, TPV curves do not decay to the same level in Fig 4.27 as different solar cells have different open circuit voltage at steady state conditions.

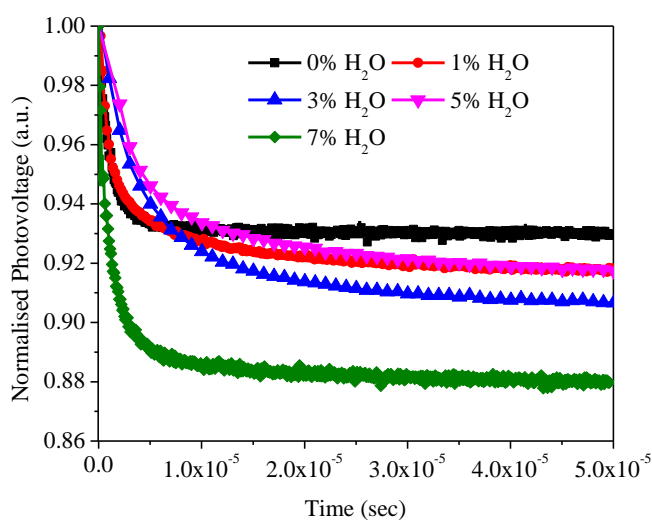


Figure 4. 27 Transient photovoltage of annealed perovskite solar cells prepared from 0%, 1%, 3%, 5% and 7% water in the MAI solution.

Charge carrier life times (table 4.10) of 1.51  $\mu\text{sec}$ , 4.36  $\mu\text{sec}$ , 7.63  $\mu\text{sec}$ , 11.60  $\mu\text{sec}$  and 1.83  $\mu\text{sec}$  were found for perovskite solar cells prepared from 0%, 1%, 3%, 5% and 7% water in the MAI solution, respectively. Charge carrier lifetime was obtained by fitting the decay function with mono-exponential equation  $\Delta V_0 \exp(-t/\tau)$  where  $\tau$  is the charge carrier life time [87, 92, 104-106].

Table 4.10 Charge transport time for annealed perovskite solar cells made under different concentrations of water in the MAI solution.

Device	Charge carrier life time
0% H <sub>2</sub> O	1.51 $\mu\text{sec}$
1% H <sub>2</sub> O	4.36 $\mu\text{sec}$
3% H <sub>2</sub> O	7.63 $\mu\text{sec}$
5% H <sub>2</sub> O	11.60 $\mu\text{sec}$
7% H <sub>2</sub> O	1.83 $\mu\text{sec}$

The highest charge carrier life time of 11.6  $\mu\text{sec}$  was found for 5% water in MAI solution. This is consistent with the increase in  $V_{OC}$  for 5% water in MAI solution in comparison to without water in MAI solution as shown in JV curves. The longest carrier life time of perovskite solar cell prepared from 5% water in MAI solution may be due to the formation of large grain size that reduces the trap charge density by reducing the total grain boundary area [2].

### 4.3 Effect of humidity on the performance of Perovskite Solar Cells

#### 4.3.1 UV-VIS spectrum of Perovskite film

Figure 4.28 shows UV-Vis spectra of perovskite film exposed to 25%, 45%, 55%, 65%, 75% humidity and inside glove box (0% RH). The films of lead iodide (PbI<sub>2</sub>) were coated onto a ca. 600 nm thick mesoporous TiO<sub>2</sub> layer from 462 mg/ml solution of PbI<sub>2</sub> in DMF. The PbI<sub>2</sub> coated films were dried at 70 °C for 30 min on a hot plate. After this,



the films were dipped in a MAI solution (10 mg/ml) for 50 sec. The as-casted films were annealed at 100 °C for 15 min. All the films were prepared with exactly the same condition as followed during the device fabrication. These films were exposed to 25%, 45%, 55%, 65%, 75% humidity for 5 hrs. The  $\text{CH}_3\text{NH}_3\text{PbI}_3$  film shows a broad absorption across the visible region with two prominent peaks at 470 nm and 790 nm in absorption spectra. The absorbance of perovskite film decreases with increasing humidity level to 45%, 55%, 65%, 75% humidity for 5 hrs with respect to sample inside the glove box and 25% RH. This could be attributed to the dissolution of perovskite phase due to water induced from increasing humidity. The reason is that the excess humidity induces more water in perovskite film which dissociates  $\text{CH}_3\text{NH}_3\text{PbI}_3$  into  $\text{PbI}_2$  and  $\text{CH}_3\text{NH}_3\text{I}$ . This  $\text{CH}_3\text{NH}_3\text{I}$  further breaks down into methylamine ( $\text{CH}_3\text{NH}_2$ ) and hydrogen iodide (HI), with the formation of  $\text{I}_2$ (solid) and  $\text{H}_2$ (gas) after exposure to oxygen and light. This is further confirmed by the measurements of XRD, KPFM and Cs-AFM that will be discussed later.

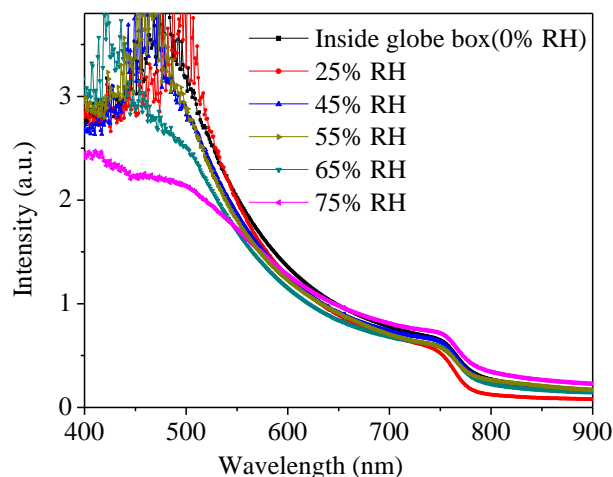


Figure 4.28 UV-VIS spectrum of perovskite film inside the glove box (0% RH) and exposed to 25%, 45%, 55%, 65% and 75% RH for 5 hrs

#### 4.3.2 XRD spectrum of Perovskite film

The perovskite crystal structure studied is given by  $ABI_3$  where A and B are cations and I is an anion. The perovskite crystal structure discussed here is  $CH_3NH_3PbI_3$  where A =  $CH_3NH_3$ , B = Pb. Ionic interactions between organic and inorganic part and hydrogen bond holds these crystal structures [42, 52]. XRD patterns were recorded to understand the effect of exposing perovskite film to different humidity level. Figure 4.29 shows XRD patterns of perovskite films exposed to 25%, 45%, 55%, 65%, 75% RH and inside the glove box. The XRD samples were prepared in the same conditions as for UV-Vis absorption measurements. The strong Bragg peaks at  $14.08^\circ$ ,  $28.41^\circ$ ,  $31.85^\circ$ , and  $43.19^\circ$  are assigned to (110), (220), (310), and (330) of  $CH_3NH_3PbI_3$ . These structures correspond to tetragonal  $I4cm$  crystal structure of halide perovskite with high crystallinity [19, 87]. The peak (001) at  $12.12^\circ$  corresponds to  $PbI_2$  and results from incomplete conversion of  $PbI_2$  to perovskite [10, 19, 45].

Remarkably, the diffractograms (Fig. 4.29) show increase in  $PbI_2$  phase for perovskite films by increasing humidity level to 45%, 55%, 65%, 75% humidity for 5 hrs with respect to sample inside the glove box and 25% RH exposed perovskite film. However, complete conversion to perovskite phase very small amount of  $PbI_2$  phase was found for perovskite film exposed to 25% RH for 5 hrs. The interaction between  $MAPbI_3$  and  $H_2O$  induced from moisture in controlled humidity is critical as  $H_2O$  affects the crystallization dynamics, growth of perovskite and the defects in grain boundary of the perovskite films [14, 46, 47, 106]. Water molecules can penetrate across the perovskite structure to form a partly reactive monohydrate ( $CH_3NH_3PbI_3 \cdot H_2O$ ) and dihydrate ( $(CH_3NH_3)_4PbI_6 \cdot 2H_2O$ ) phases [47]. These hydrated phases are formed due to water

incorporation into the perovskite lattice by the formation of hydrogen bonds between water molecules and lattice iodides, as well as from hydrogen bonding interaction between MA cations and water molecules. Moisture can improve the growth of perovskite films from the interaction between H<sub>2</sub>O and MAPbI<sub>3</sub>, such as hydrogen bonding interaction [43].

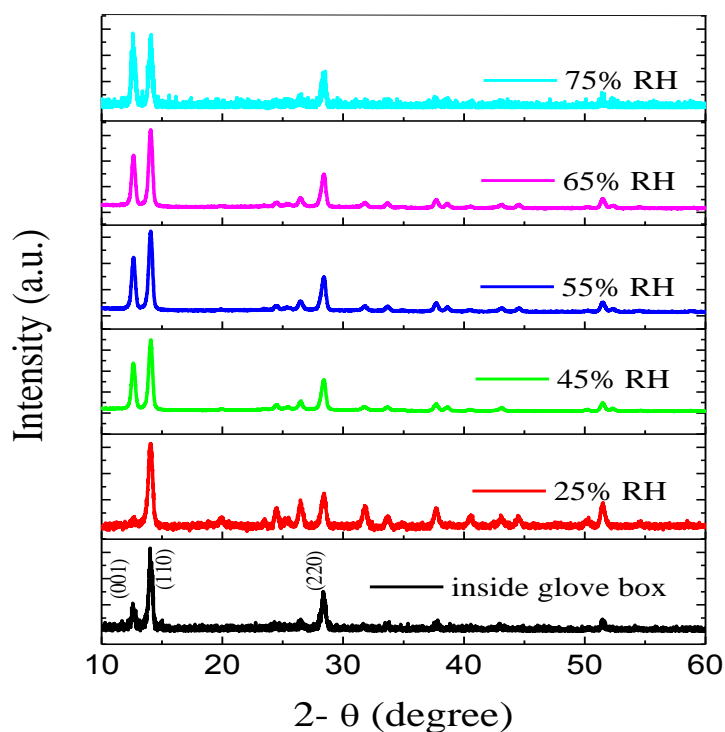


Figure 4.29 XRD spectrum of perovskite film inside the glove box and exposed to 25%, 45%, 55%, 65% and 75% RH for 5 hrs

The degradation of perovskite to PbI<sub>2</sub> and CH<sub>3</sub>NH<sub>3</sub>I was found after increasing RH beyond 25% RH. The degradation becomes prominent and converts 50% perovskite phases into PbI<sub>2</sub> when the perovskite film was exposed to 75% humidity for 5 hrs. If the film is exposed to excess humidity, dissolution of the polar organic CH<sub>3</sub>NH<sub>3</sub><sup>+</sup> in the

perovskite structure occurs that results in dissociation of perovskite into  $\text{PbI}_2$  and  $\text{CH}_3\text{NH}_3\text{I}$  due to water induced from moisture [20]. The dissociation of the perovskite into  $\text{PbI}_2$  and formation of hydrated phases affects the grain boundary potential and subsequently the charge transport in perovskite film which is discussed in following section with surface potential (SP) and Cs-AFM measurements.

#### 4.3.3 Topography and KPFM images of Perovskite film

Fig. 4.30. shows AFM Topography (a - f) of perovskite film exposed to 25%, 45%, 55%, 65% and 75% RH for 5 hrs and prepared inside the glove box. Topography image shows that the prepared perovskite film has grain size varying from 120 nm to 500 nm. However, voids are seen in the film while increasing the humidity to 75%. The variation in height of perovskite film exposed to 25% RH (0 -184 nm) is minimum compared to all other conditions inside glove box, 45%, 55%, 65% and 75% RH. The perovskite film kept at 75% humidity level for 5 hrs shows larger grains (~500 nm) compared to perovskite film inside glove box with some grains between 120 nm -300 nm) and 25% RH. This may be due to the dissolution of the smaller grains leaving larger grains which can be assigned to lead iodide. The water induced from the high humidity dissociates perovskite to lead iodide [20]. Figure 4.30 (g-l) show 2D surface potential maps of perovskite films exposed to 25%, 45%, 55%, 65% and 75% RH for 5 hrs and inside the glove box. KPFM of perovskite films demonstrates higher surface potential at the grain boundaries (GBs) than within grains. This corresponds to a downward band bending in the energy band diagram leading to the minority carrier electrons in p-type absorber layer to be attracted towards GBs which is consistent with the previous literatures [71].

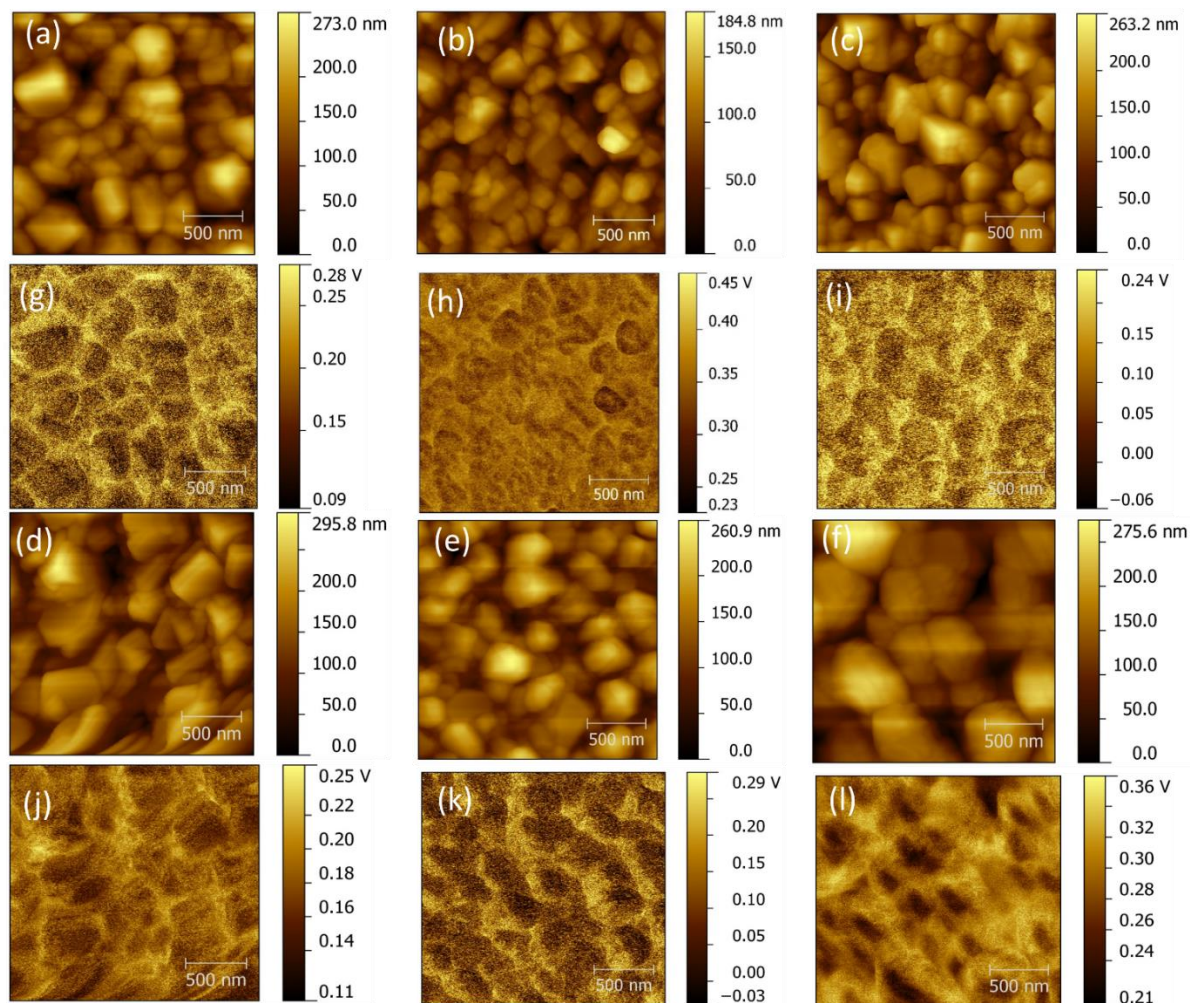


Figure 4.30 AFM topography (a - f) and surface potential images (g - l) of perovskite films inside the glove box (a & g) and exposed to 25% (b & h), 45% (c & i), 55% (d & j), 65% (e & f) and 75% (f&k) RH for 5 hrs, respectively.

It is worth noting that the grain boundary potential is not same for all the humidity level suggesting that the electrical properties of grain boundary strongly depends on the neighboring grains. It can be noted that the constant surface potential is found for perovskite film prepared at 25% RH throughout the film (Fig 4.30h). This may be the reason for higher performance device obtained in this case which will be discussed in detail in next section. The grain boundary width increases with increases humidity level

and is maximum for perovskite film exposed to 75% RH level (Fig 4.30l). This is due to the formation of defects and traps due to hydration of grain boundaries that may results dissociation of perovskite in to lead iodide and hydrated phase as shown in XRD spectrum (Fig 4.29). The grain boundary potential increases with increasing humidity level which is shown in surface potential line profile obtained in Fig 4.31.

#### 4.3.4 Surface potential line profile of Perovskite film

Figure 4.31 shows surface potential line scanning of perovskite film inside the glove box and exposed to 25%, 45%, 55%, 65% and 75% RH for 5 hrs. The grain boundary potential increases from 35 meV (Fig 4a & 3a) to 82 meV (Fig 4.31f & 4.31l) for perovskite film kept inside glove box to perovskite film exposed to 75% RH. This may be due to formation of additional phase of  $\text{PbI}_2$  as seen from XRD spectrum (Fig. 4.29) and other stable hydrated phase due to exposure to high humidity conditions. KPFM measures the contact potential difference between tip and sample which is the difference between the work function of tip and sample. Therefore, the change in electrical barrier due to  $\text{PbI}_2$  and other hydrated phase can be determined.

Average surface potential of perovskite film increases due to formation of  $\text{PbI}_2$  phase whose VB lies below the perovskite VB. The grain boundary potential is minimum for perovskite film exposed to 25% RH which contains very small amount of lead iodide (Fig 4.29). However, the grain boundary potential does not changes significantly while changing humidity from 45% RH (Fig 4.31c & 4.31i) to 55% RH (Fig 4.31d & Fig 4.31j). Similarly, there was no any significant change in grain boundary potential by increasing humidity from 65% RH (Fig 4.31e & 4.31k) to 75% RH (Fig 4.31f & 4.31l). Grain boundary potential of 50 meV and 80 meV are obtained for 45% RH and 65% RH.

The increase in grain boundary potential reduces charge transport within the grains of the perovskite film and decreases the device performance.

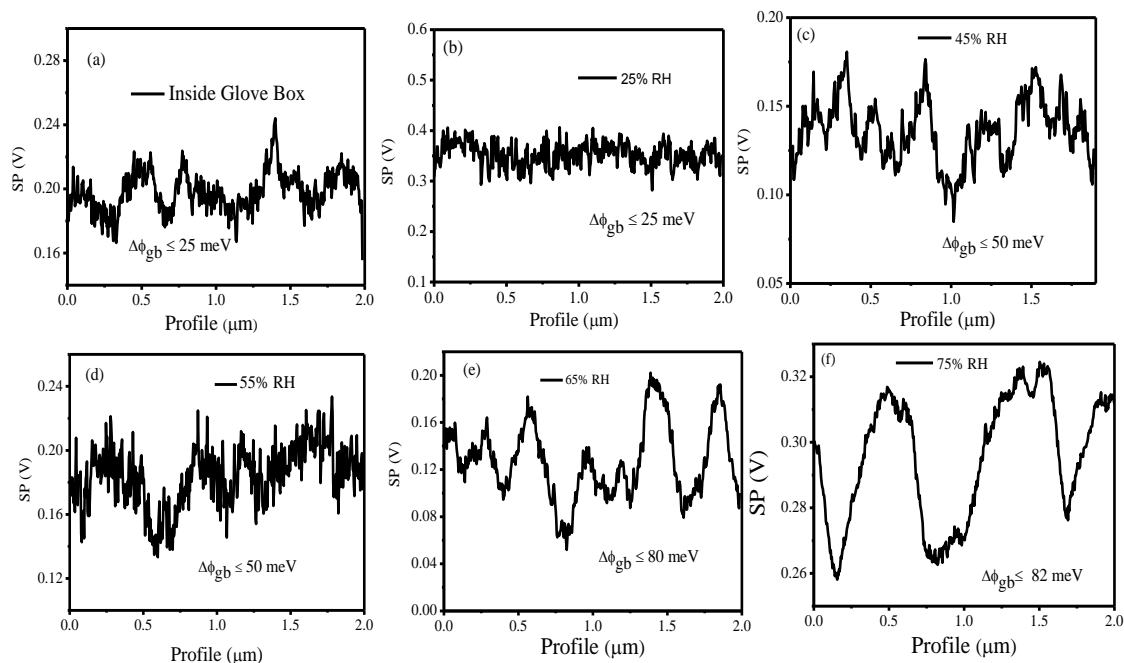


Figure 4.31 Surface potential line scanning of Perovskite film (a) inside the glove box and exposed to (b) 25%, (c) 45%, (d) 55%, (e) 65% RH and (f) 75% RH for 5 hrs

#### 4.3.5 Current sensing AFM imaging of Perovskite film

To further understand the role of humidity on carrier transportation in perovskite solar cells, Cs-AFM was used to measure the local current on grains and GBs and thus determine the surface conductivity of perovskite film. First, Cs-AFM of perovskite film exposed to different humidity conditions was measured. Fig. 4.32 shows CS-AFM imaging of perovskite film prepared inside the glove box and exposed to 25%, 45%, 55%, 65% and 75% RH for 5 hrs. Cs-AFM of grain boundary and grain of perovskite film gives the fundamental conduction mechanism in the device. Grain boundaries

consists of defects and dislocations and acts as trap states for the photo generated charge carriers.

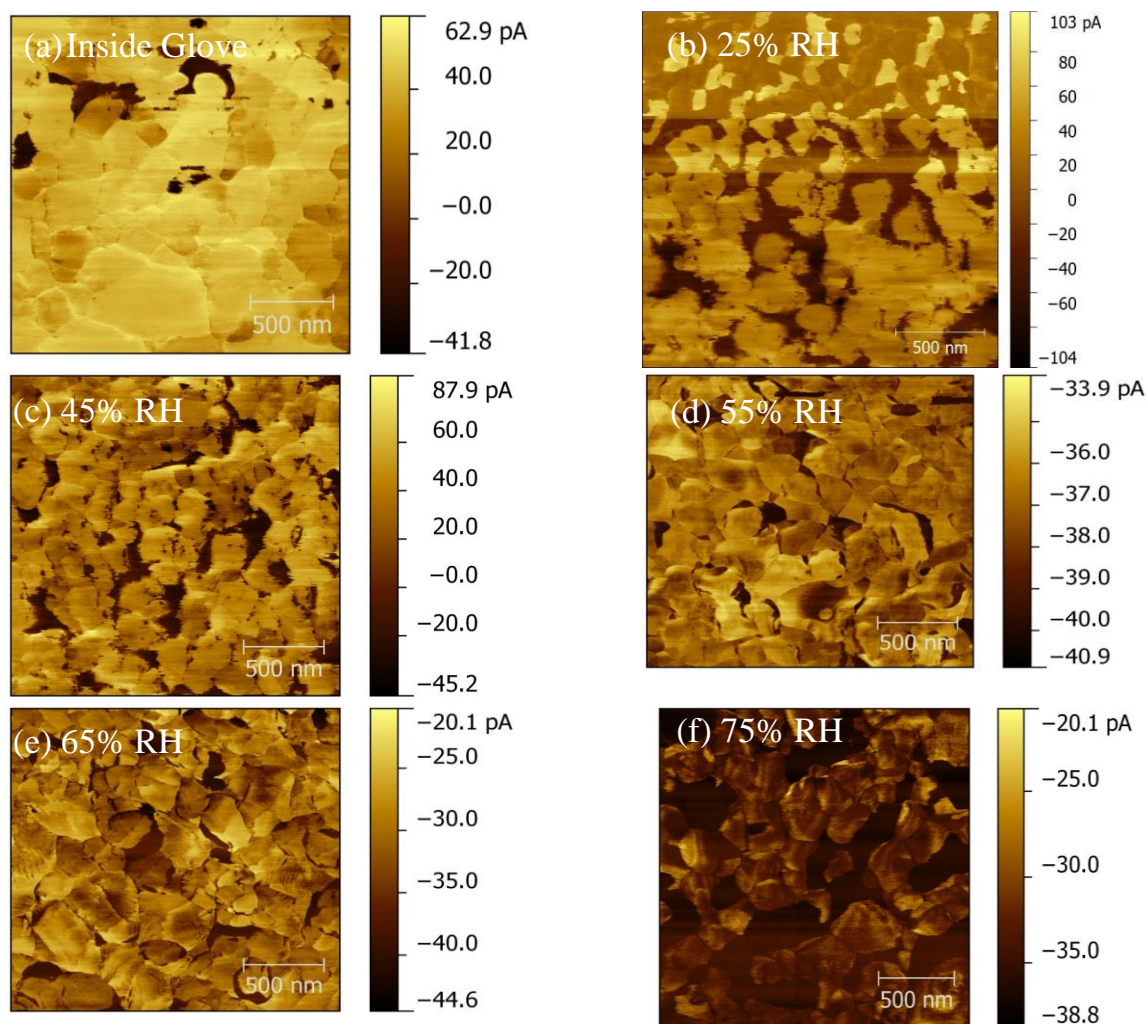


Figure 4. 32 CS-AFM imaging of perovskite film (a) inside the glove box and exposed to (b) 25 %, (c) 45 %, (d) 55 %, (e) 65 % RH for 5 hrs; and (f) 75 % RH

Therefore, there is different electronic behavior of electron and holes within grains and on grain boundary and the understanding of the conduction process inside the device is needed. The perovskite film demonstrate higher surface potentials (Fig.4.30) at the GBs compared to the surface of the grains. A higher positive potential at the grain



boundaries would correspond to a downward band-bending in the energy band diagram. This leads to minority carriers, electrons in p-type perovskite absorbers, to be attracted into the grain boundary, and majority carriers, holes, to be repelled away from the grain boundary. The average grain boundary potential of perovskite film increases by 57 meV while increasing the humidity level from 0% RH to 75% RH respectively [3, 7, 50]. This downward band bending acts as barrier for holes and creates an additional built in barrier for charges to flow. This barrier needs to be overcome in order to transport the carriers effectively. The highest current of 103 pA (Fig 4.32b) was found for perovskite film exposed to 25% RH conditions and the current decreases with increasing humidity to 75% which is 38.8 pA (Fig 4.32f).

#### 4.3.6 Current density-voltage (J-V) curves of Perovskite Solar Cells

Figure 4.33 shows current density-voltage (J-V) curves of perovskite solar cells with device structure of FTO/c-TiO<sub>2</sub>/mesoporous-TiO<sub>2</sub>/CH<sub>3</sub>NH<sub>3</sub>PbI<sub>3</sub>/Ag prepared inside the glove box and exposed to 25%, 45%, 55%, 65% and 75% RH. The perovskite films were prepared from sequential deposition method where PbI<sub>2</sub> film was spin coated and dried first. Finally, the films were dipped in 10 mg/ml MAI solution. Device performance of prepared cells were measured under 100 mW/cm<sup>2</sup> AM 1.5 simulated solar irradiation with a humidity of 40%. The scan rate was kept constant for all devices with 0.5 V/sec. The cells were characterized both in forward and reverse scan due to the JV hysteresis and degradation of the devices while switching the voltage [88].

As shown in table 4.11, after increasing the humidity level to 25%, the average efficiency was found to increase and then decreases with increasing humidity to 45%, 55%, 65% and 75%. The photovoltaic efficiencies were found to increase from 9.27% and

11.47% in forward and reverse scan to 13.04% and 14.09% in forward and reverse scan, respectively. This increase in efficiency is mainly due to increase in open circuit voltage and short circuit current density. This is due to increase in local current due to decrease in grain boundary potential within the grains. This helps to increase charge transport by decreasing the barrier. After, increasing the humidity level to 45%, 55%, 65% and 75% RH, the device efficiency was found to decrease. The forward and reverse bias efficiency corresponds to 75% RH was found to be 5.18% and 7.37%. Decrease in open circuit voltage ( $V_{OC}$ ) is caused by the recombination of the electrons and holes within the grain boundary due to increase in charge trap states and defects within the grain boundary as shown in table 4.12. The decrease in short circuit current density ( $J_{sc}$ ) is due to the decrease in local current as shown in Fig. 4.32 by CS-AFM measurements and also due to decrease in absorbance (Fig.4.28).

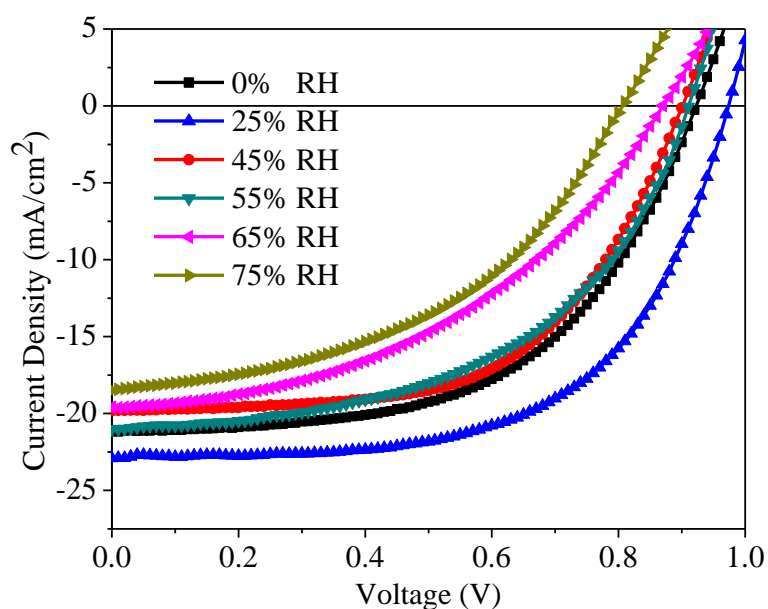


Figure 4. 33 Current density-voltage (J-V) characteristics of perovskite solar cells prepared from perovskite film inside the glove box and exposed to 45%, 55%, 65% and 75% RH for 5 hrs

It can be seen that the device efficiency increased when the humidity was increased from inside glove box to 25% and decreased when increased to 45%, 55%, 65% and 75% RH. A number of devices were prepared and similar efficiencies were found. H<sub>2</sub>O induced from moisture with suitable controlled humidity can weakly bind to methylammonium molecules and form reversible hydrated phase within perovskite, which quickly forms dehydrated perovskite upon exposure to air [2].

Table 4.11 Photovoltaic parameters for perovskite solar cells exposed to different humidity

Device	J <sub>sc</sub>		V <sub>oc</sub>		FF		η%	
	Forward	Reverse	Forward	Reverse	Forward	Reverse	Forward	Reverse
0% RH	19.93	21.18	0.91	0.93	0.51	0.58	9.27	11.47
25% RH	22.99	22.90	0.95	0.98	0.60	0.63	13.04	14.09
45% RH	21.26	19.82	0.92	0.91	0.45	0.57	8.86	10.32
55% RH	21.13	21.02	0.9	0.92	0.50	0.54	9.32	10.50
65% RH	19.80	19.6	0.87	0.87	0.43	0.47	7.44	8.014
75% RH	17.78	18.49	0.75	0.81	0.39	0.49	5.18	7.37

Optimum exposure of perovskite film to control humidity results in optimal H<sub>2</sub>O which can dissolve the methylammonium and other components, providing them higher mobility and allowing excess methylammonium to be removed, healing the perovskite structure and fulfilling the deficits and any trap states [91, 94]. Thus, decrease in the trap states results in less non-radiative trap-mediated recombination [2]. Hence, exposing perovskite film to 25% RH leads to improved V<sub>oc</sub>, FF and hence overall device performance. The decrease in performance of perovskite solar cell prepared by exposing it to higher humidity conditions is due to excess H<sub>2</sub>O content which dissolute perovskite phase to PbI<sub>2</sub> and CH<sub>3</sub>NH<sub>3</sub>I.

#### 4.3.7 Grain boundary model of Perovskite Solar Cells

Figure 4.34 shows the schematic of surface potential and band bending at grain boundary with width of grain boundary and grain boundary potential. The charge carrier concentration is calculated using a grain boundary model from surface potential images obtained using KPFM (Fig 4.30). In this model, a grain boundary corresponds to a surface with surface charge, therefore the net doping  $P_{\text{net}}$  of perovskite can be calculated from the size of band bending [45]. The doping density in this case is given by  $P_{\text{net}} = \frac{2\epsilon_0 \epsilon \Delta\phi gb}{e^2 w^2}$  where  $\Delta\phi$  is the grain boundary potential and  $w$  is the width of the grain boundary which is obtained from surface potential line profile (Fig. 4.31).

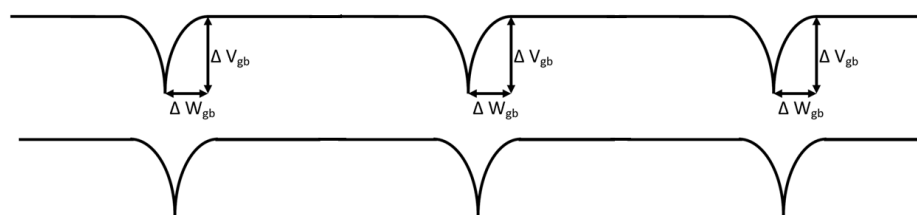


Figure 4.34 Schematic diagram of nanoscale potential distribution around grain boundary in Perovskite solar cell

The doping density shows that the perovskite is self-doped. It is reported that the perovskite has ambipolar properties and study shows that the perovskite behaves as p-type conductivity due to self-doping with  $\text{TiO}_2$  as interfacial layer. KPFM measures the change in work function between tip and sample [48]. In this experimental measurements, It has been found that the GB potential and width, dopant density, and density of charged trap states, as shown in Table 4.13. It is found that the defect density increases from  $4.12 \times 10^{17} / \text{cm}^3$  to  $7.75 \times 10^{17} / \text{cm}^3$  on increasing the humidity level from inside globe box to 65% RH.

Table 4.12 Dopant density and density of charged trap states of Perovskite film inside the glove box and exposed to 45% and 65% for 5 hrs

Conditions	GB Potential	Dopant density (/cm <sup>3</sup> )	Density of charged trap states
Inside GB	35 meV	$4.12 \times 10^{17}$	$1.12 \times 10^{13}$
45% RH	50meV	$5.57 \times 10^{17}$	$1.56 \times 10^{13}$
65% RH	80 meV	$7.75 \times 10^{17}$	$2.34 \times 10^{13}$

#### 4.3.8 Transient photoconductivity measurement

Figure 4.35 shows Transient photocurrent decay (TPC) of perovskite solar cells prepared from perovskite film inside the glove box and exposed to 45%, 55%, 65% and 75% RH for 5 hrs. The short lived photocurrent is generated by a nanosecond pulse of a dye laser incident on solar cells under short circuit conditions (by a very low resistor at 20  $\Omega$ ). No background light was applied when measuring TPC. This is the reason when the pulse laser was off, the TPC decays reach to zero for all samples. Charge transport time was obtained by fitting the decay function with mono-exponential equation  $\Delta I_0 \exp(-t/\tau)$  where  $\tau$  is the charge carrier life time. The transient current has been normalized in order to clearly visualize the charge transport decay which is the central part of this experiment. It was found that the values of charge transport time (table 2) of 3.36  $\mu\text{sec}$ , 0.58  $\mu\text{sec}$ , 4.72  $\mu\text{sec}$ , 4.29  $\mu\text{sec}$ , 5.23  $\mu\text{sec}$  and 5.98  $\mu\text{sec}$  for perovskite solar cells prepared from perovskite film kept inside glove box and exposed to 45%, 55%, 65% and 75% RH for 5 hrs respectively. The charge transport time of perovskite film prepared by exposing to 25% RH for 5 hrs is fastest showing efficient charge extraction [103]. These results are in agreement with CS-AFM, KPFM and JV characteristics where enhanced local current, minimum grain boundary potential and highest device efficiency was

found. But, the charge transport time becomes longer (5.98  $\mu\text{sec}$ ) for sample exposed to 75% which may be caused by the dissociation of  $\text{CH}_3\text{NH}_3\text{PbI}_3$  into  $\text{PbI}_2$  and  $\text{CH}_3\text{NH}_3\text{I}$  due to degradation from high humidity conditions.

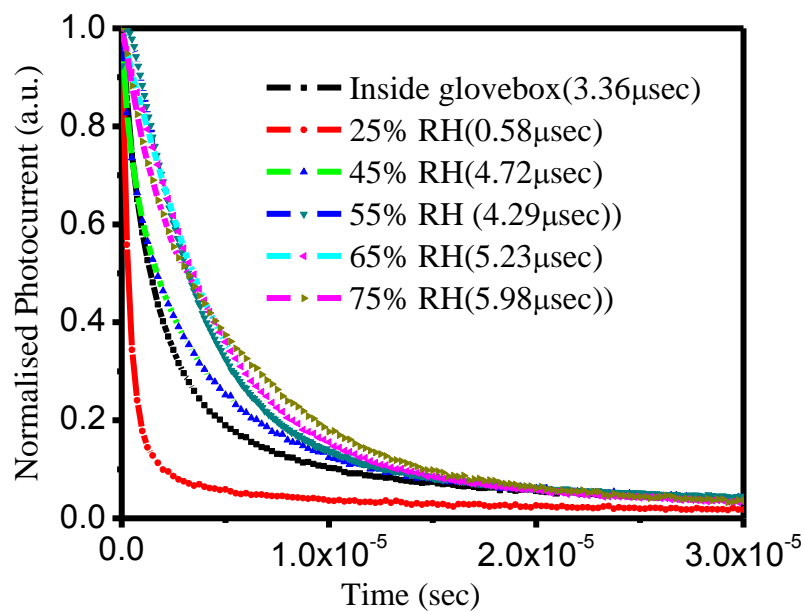


Figure 4.35 Transient photocurrent decay of perovskite solar cells prepared from perovskite film inside the glove box and exposed to 45%, 55%, 65% and 75% RH for 5 hrs.

## Chapter 5 Summary and Conclusions

### 5.1 Summary

Humanity has already faced consequences of wide use of non-renewable natural resources affecting the environment in an irreversible way for example air pollution, soil erosions and ozone layer depletion. This clearly highlights the need of a pollution free, renewable source of energy to minimize the adverse impacts to the environments. Sun provides 6700 times the annual world primary energy consumption per year. Therefore, harvesting the energy supplied by sun in easy means is a key approach to produce sustainable energy. The silicon solar cell has huge market which is over 95% of all the solar cells produced worldwide. However, c-Si cell technology requires high temperature and high vacuum processes which are costly. Also, c-Si requires a few hundred microns thick film to absorb sufficient light due to its relatively poor light absorbance. Due to the low cost advantages, perovskite solar cells have generated wide interest as a potential replacement for silicon solar cells.

First perovskite solar cell was fabricated with an efficiency of 3.8% by Miyasaka et al. in 2009. However, the liquid electrolyte dissolved the perovskite film and the film was not stable for longer time operation. Then in 2012, Park et al. reported a long term stable perovskite solar cell with efficiency up to 9.7%. In 2015, Yang et al. achieved an efficiency of 20.2 % using formamidinium lead iodide (FAPbI<sub>3</sub>) which has broad absorption compared to conventional methyl ammonium lead iodide. In 2016 Saliba et al. showed stabilized efficiency of 21.1% and 18% after 250 hours under standard operational conditions.

The commercial use of the organo lead halide perovskite based solar cell is challenging because of its poor stability with moisture and temperature despite its promising efficiency. The degradation mechanism is open for debate in the field of perovskite solar cells. Therefore, understanding degradation mechanism is critical to provide materials design principles and engineering strategies to achieve long-term stability in perovskite solar cells. The charge transport in perovskite solar cell strongly depends on humidity and annealing conditions. Previous reports showed that contact potential difference (CPD) of GBs in perovskite films is higher than within the grains and decreases after illumination. In addition, the crystallization of perovskite film can be increased by directly adding water in methyl ammonium iodide solution. Previous reports shows that optimum amount of lead iodide helps to passivate the perovskite film.

There is a strong need for stable, low cost and highly efficient organic-inorganic perovskite solar cells. The objective of this work is to develop high performance perovskite solar cell with efficiency greater than 20% and to study the nanoscale charge transport with annealing conditions and humidity. Another goal of the project is to study the crystallization of perovskite film by adding water directly in methyl ammonium iodide solution during perovskite film formation.

Kelvin probe force microscopy (KPFM) is a method to study the nanoscale potential distribution along grain and grain boundary. Cs-AFM in conjugation with kelvin probe force microscopy can be used to study the local charge transport properties in perovskite solar cells. Hence, KPFM determines interface energetics, which can be used to study the role of interfacial layer on the recombination of high performance devices.



Perovskite solar cells were prepared from single step and sequential deposition method. The prepared perovskite films were annealed at 100 °C for various durations to suppress the back recombination of electrons from TiO<sub>2</sub> and holes from perovskite. The perovskite films were also prepared by adding varying amount of water (1%-7% by volume of IPA) in methyl ammonium iodide solution. In addition, some of the perovskite films were exposed to different humidity conditions (25% to 75%). The prepared films were then characterized using UV-vis spectroscopy, XRD and KPFM. Current density voltage characteristics were measured using an Agilent 4155C semiconductor parameter analyzer integrated with a Newport xenon lamp (67005) as solar simulator (AM 1.5). Transient photoconductivity was measured using nitrogen coupled dye laser with pulse duration less than 1 nsec.

Nanoscale kelvin probe force microscopy (KPFM) measurement shows that charge transport in perovskite solar cell critically depends upon annealing conditions, humidity and doping with water during perovskite film formation. The KPFM results of single step and sequential deposited films show that the increase in potential barrier suppresses the back recombination between electrons in TiO<sub>2</sub> and holes in perovskite due to formation of optimal amount of lead iodide formed from annealing. An optimal amount of water (5%) added to the Methyl ammonium Iodide solution in isopropyl alcohol helps perovskite crystallization and leads to larger grain size. The grain boundary potential increases with increasing humidity level from sample kept inside glove box (0% RH) to 75% RH and affects the nanoscale charge transport. The degradation of perovskite solar cell is mainly associated with hydration of the grain boundaries with the formation of hydrated phases and increase of PbI<sub>2</sub> phase with increase in humidity level beyond

25% RH. Minimum grain boundary potential ( $<25$  meV) was found for 25% humidity exposed perovskite film. Device performances of the solar cells were found to increase from 9.27% to 13.04% in forward scan and 11.47% to 14.09% in reverse scan on increasing humidity level from inside glove box to 25% RH.

Future work includes fabrication and optimization of perovskite solar cells in controlled humidity with optimal amount of water in methyl ammonium iodide solution to obtain efficiency up to 20% and to understand the ambipolar properties of perovskite solar cell using kelvin probe force microscopy.

## 5.2 Conclusions

The effect of annealing conditions, humidity and addition of water during perovskite film formation has been studied successfully. The quantitative measurement of grain-boundary (GB) potential and  $\text{TiO}_2$ -perovskite interface surface potential in perovskite solar cells has been shown. KPFM measurement shows that charge transport in perovskite solar cell depends upon annealing conditions. The KPFM results of single step and sequential deposited films show that the barrier increases due to the formation of  $\text{PbI}_2$  that suppresses the back recombination between electrons in  $\text{TiO}_2$  and holes in perovskite. XRD results confirm the formation of perovskite and lead iodide phase upon annealing. Nanoscale CS-AFM images show that charge transport in perovskite solar cells strongly depends in humidity level. It was found that an increase in humidity level resulted in the dissolution of perovskite phase in to lead iodide. Grain boundary potential barriers were found to increase from  $\sim 35$  meV for 0% humidity in glove box to 82 meV for perovskite film exposed to 75% RH level. The minimum grain boundary potential was found for films exposed to 25% RH. Water is an important factor in perovskite film

formation with dual roles: 1) assisting perovskite crystallization with optimum amount 2) dissociates perovskite in to lead iodide and methyl ammonium iodide. 5% by volume was found as an optimal amount of water for crystallizing the perovskite film in the (110) plane that increased the grain size three times of that prepared without water in the MAI solution. The increase in grain size and crystallinity of perovskite film helps to reduce the recombination of charge carriers by decreasing the total grain boundary area. Average performance of solar cells were found to increases from 10.37% to 13.57% when humidity level is increased from 0% inside glove box to 25% RH.

## References

- [1] (07-29-2016). *Best solar cell efficiencies* Available:  
[http://www.nrel.gov/ncpv/images/efficiency\\_chart.jpg](http://www.nrel.gov/ncpv/images/efficiency_chart.jpg)
- [2] T. Glatzel, D. F. Marrón, T. Schedel-Niedrig, S. Sadewasser, and M. C. Lux-Steiner, "CuGaSe 2 solar cell cross section studied by Kelvin probe force microscopy in ultrahigh vacuum," *Applied physics letters*, vol. 81, pp. 2017-2019, 2002.
- [3] J. B. Li, V. Chawla, and B. M. Clemens, "Investigating the role of grain boundaries in CZTS and CZTSSe thin film solar cells with scanning probe microscopy," *Advanced Materials*, vol. 24, pp. 720-723, 2012.
- [4] W. J. Yin, T. Shi, and Y. Yan, "Unique properties of halide perovskites as possible origins of the superior solar cell performance," *Advanced Materials*, vol. 26, pp. 4653-4658, 2014.
- [5] E. Edri, S. Kirmayer, A. Henning, S. Mukhopadhyay, K. Gartsman, Y. Rosenwaks, *et al.*, "Why lead methylammonium tri-iodide perovskite-based solar cells require a mesoporous electron transporting scaffold (but not necessarily a hole conductor)," *Nano letters*, vol. 14, pp. 1000-1004, 2014.
- [6] Q. Chen, H. Zhou, T.-B. Song, S. Luo, Z. Hong, H.-S. Duan, *et al.*, "Controllable self-induced passivation of hybrid lead iodide perovskites toward high performance solar cells," *Nano letters*, vol. 14, pp. 4158-4163, 2014.
- [7] J. S. Yun, A. Ho-Baillie, S. Huang, S. H. Woo, Y. Heo, J. Seidel, *et al.*, "Benefit of Grain Boundaries in Organic–Inorganic Halide Planar Perovskite Solar Cells," *The Journal of Physical Chemistry Letters*, vol. 6, pp. 875-880, 2015/03/05 2015.

- [8] M. A. Green, K. Emery, Y. Hishikawa, W. Warta, and E. D. Dunlop, "Solar cell efficiency tables (Version 45)," *Progress in photovoltaics: research and applications*, vol. 23, pp. 1-9, 2015.
- [9] V. W. Bergmann, S. A. Weber, F. J. Ramos, M. K. Nazeeruddin, M. Grätzel, D. Li, *et al.*, "Real-space observation of unbalanced charge distribution inside a perovskite-sensitized solar cell," *Nature communications*, vol. 5, 2014.
- [10] C.-S. Jiang, M. Yang, Y. Zhou, B. To, S. U. Nanayakkara, J. M. Luther, *et al.*, "Carrier separation and transport in perovskite solar cells studied by nanometre-scale profiling of electrical potential," *Nature communications*, vol. 6, 2015.
- [11] Q. Chen, H. Zhou, Z. Hong, S. Luo, H.-S. Duan, H.-H. Wang, *et al.*, "Planar heterojunction perovskite solar cells via vapor-assisted solution process," *Journal of the American Chemical Society*, vol. 136, pp. 622-625, 2013.
- [12] N. J. Jeon, J. H. Noh, W. S. Yang, Y. C. Kim, S. Ryu, J. Seo, *et al.*, "Compositional engineering of perovskite materials for high-performance solar cells," *Nature*, 2015.
- [13] P. Cui, P. Fu, D. Wei, M. Li, D. Song, X. Yue, *et al.*, "Reduced surface defects of organometallic perovskite by thermal annealing for highly efficient perovskite solar cells," *RSC Advances*, vol. 5, pp. 75622-75629, 2015.
- [14] W.-J. Yin, T. Shi, and Y. Yan, "Unusual defect physics in CH<sub>3</sub>NH<sub>3</sub>PbI<sub>3</sub> perovskite solar cell absorber," *Applied Physics Letters*, vol. 104, p. 063903, 2014.

- [15] Y. Rong, Z. Tang, Y. Zhao, X. Zhong, S. Venkatesan, H. Graham, *et al.*, "Solvent engineering towards controlled grain growth in perovskite planar heterojunction solar cells," *Nanoscale*, vol. 7, pp. 10595-10599, 2015.
- [16] N. Adhikari, A. Dubey, E. A. Gaml, B. Vaagensmith, K. M. Reza, S. A. A. Mabrouk, *et al.*, "Crystallization of a perovskite film for higher performance solar cells by controlling water concentration in methyl ammonium iodide precursor solution," *Nanoscale*, vol. 8, pp. 2693-2703, 2016.
- [17] H. J. Snaith, "How should you measure your excitonic solar cells?," *Energy & Environmental Science*, vol. 5, pp. 6513-6520, 2012.
- [18] H. J. Snaith, A. Abate, J. M. Ball, G. E. Eperon, T. Leijtens, N. K. Noel, *et al.*, "Anomalous Hysteresis in Perovskite Solar Cells," *The Journal of Physical Chemistry Letters*, vol. 5, pp. 1511-1515, 2014/05/01 2014.
- [19] W. Tress, N. Marinova, T. Moehl, S. M. Zakeeruddin, M. K. Nazeeruddin, and M. Gratzel, "Understanding the rate-dependent J-V hysteresis, slow time component, and aging in CH<sub>3</sub>NH<sub>3</sub>PbI<sub>3</sub> perovskite solar cells: the role of a compensated electric field," *Energy & Environmental Science*, vol. 8, pp. 995-1004, 2015.
- [20] E. L. Unger, E. T. Hoke, C. D. Bailie, W. H. Nguyen, A. R. Bowring, T. Heumuller, *et al.*, "Hysteresis and transient behavior in current-voltage measurements of hybrid-perovskite absorber solar cells," *Energy & Environmental Science*, vol. 7, pp. 3690-3698, 2014.
- [21] S. Sigdel, A. Dubey, H. Elbohy, A. Aboagye, D. Galipeau, L. Zhang, *et al.*, "Dye-Sensitized Solar Cells Based on Spray-coated Carbon Nanofibers/TiO<sub>2</sub>

- Nanoparticles Composite Counter Electrodes," *Journal of Materials Chemistry A*, 2014.
- [22] P. P. Maharjan, Q. Chen, L. Zhang, O. Adebajo, N. Adhikari, S. Venkatesan, *et al.*, "Photovoltaic devices and characterization of a dodecyloxybenzothiadiazole-based copolymer," *Physical Chemistry Chemical Physics*, vol. 15, pp. 6856-6863, 2013.
- [23] J. Lee, H. Jun, and J. Kim, "Polydiacetylene–liposome microarrays for selective and sensitive mercury (II) detection," *Advanced Materials*, vol. 21, pp. 3674-3677, 2009.
- [24] S. Seo, J. Lee, E. J. Choi, E. J. Kim, J. Y. Song, and J. Kim, "Polydiacetylene Liposome Microarray Toward Influenza A Virus Detection: Effect of Target Size on Turn-On Signaling," *Macromolecular rapid communications*, vol. 34, pp. 743-748, 2013.
- [25] N. J. Jeon, J. H. Noh, Y. C. Kim, W. S. Yang, S. Ryu, and S. I. Seok, "Solvent engineering for high-performance inorganic–organic hybrid perovskite solar cells," *Nat Mater*, vol. 13, pp. 897-903, 09//print 2014.
- [26] J. H. Noh, S. H. Im, J. H. Heo, T. N. Mandal, and S. I. Seok, "Chemical management for colorful, efficient, and stable inorganic–organic hybrid nanostructured solar cells," *Nano letters*, vol. 13, pp. 1764-1769, 2013.
- [27] A. Kojima, K. Teshima, Y. Shirai, and T. Miyasaka, "Organometal halide perovskites as visible-light sensitizers for photovoltaic cells," *Journal of the American Chemical Society*, vol. 131, pp. 6050-6051, 2009.

- [28] D. Nanova, A. K. Kast, M. Pfannmöller, C. Müller, L. Veith, I. Wacker, *et al.*, "Unraveling the Nanoscale Morphologies of Mesoporous Perovskite Solar Cells and Their Correlation to Device Performance," *Nano letters*, vol. 14, pp. 2735-2740, 2014.
- [29] J.-H. Im, I.-H. Jang, N. Pellet, M. Grätzel, and N.-G. Park, "Growth of CH<sub>3</sub>NH<sub>3</sub>PbI<sub>3</sub> cuboids with controlled size for high-efficiency perovskite solar cells," *Nature nanotechnology*, vol. 9, pp. 927-932, 2014.
- [30] W. Dong, J. Luo, H. He, and L. Jiang, "A reinforced composite structure composed of polydiacetylene assemblies deposited on polystyrene microspheres and its application to H5N1 virus detection," *International journal of nanomedicine*, vol. 8, p. 221, 2013.
- [31] M. Grätzel, "The light and shade of perovskite solar cells," *Nature materials*, vol. 13, pp. 838-842, 2014.
- [32] N. S. An, Y. N. Shi, J. Q. Feng, D. P. Li, J. Gao, Y. L. Chen, *et al.*, "N-channel organic thin-film transistors based on a soluble cyclized perylene tetracarboxylic diimide dimer," *Organic Electronics*, vol. 14, pp. 1197-1203, Apr 2013.
- [33] C.-G. Wu, C.-H. Chiang, Z.-L. Tseng, M. K. Nazeeruddin, A. Hagfeldt, and M. Grätzel, "High efficiency stable inverted perovskite solar cells without current hysteresis," *Energy & Environmental Science*, 2015.
- [34] J. You, Y. M. Yang, Z. Hong, T.-B. Song, L. Meng, Y. Liu, *et al.*, "Moisture assisted perovskite film growth for high performance solar cells," *Applied Physics Letters*, vol. 105, p. 183902, 2014.



- [35] S. Pathak, A. Sepe, A. Sadhanala, F. Deschler, A. Haghighirad, N. Sakai, *et al.*, "Atmospheric Influence upon Crystallization and Electronic Disorder and Its Impact on the Photophysical Properties of Organic–Inorganic Perovskite Solar Cells," *ACS nano*, vol. 9, pp. 2311-2320, 2015.
- [36] A. F. Mitul, L. Mohammad, B. Vaagensmith, D. Khatiwada, A. Dubey, and Q. Qiao, "Optimization of interfacial layer for double and triple junction polymer solar cell," in *SPIE Organic Photonics+ Electronics*, 2015, pp. 95671R-95671R-3.
- [37] G. E. Eperon, S. N. Habisreutinger, T. Leijtens, B. J. Bruijnaers, J. J. van Franeker, D. W. deQuilettes, *et al.*, "The Importance of Moisture in Hybrid Lead Halide Perovskite Thin Film Fabrication," *ACS nano*, 2015.
- [38] A. I. M. Leguy, Y. Hu, M. Campoy-Quiles, M. I. Alonso, O. J. Weber, P. Azarhoosh, *et al.*, "Reversible Hydration of CH<sub>3</sub>NH<sub>3</sub>PbI<sub>3</sub> in Films, Single Crystals, and Solar Cells," *Chemistry of Materials*, vol. 27, pp. 3397-3407, 2015.
- [39] J. H. Kim, S. T. Williams, N. Cho, C. C. Chueh, and A. K. Y. Jen, "Enhanced Environmental Stability of Planar Heterojunction Perovskite Solar Cells Based on Blade-Coating," *Advanced Energy Materials*, vol. 5, 2015.
- [40] K.-F. Lin, S. H. Chang, K.-H. Wang, H.-M. Cheng, K. Y. Chiu, K.-M. Lee, *et al.*, "Unraveling the high performance of tri-iodide perovskite absorber based photovoltaics with a non-polar solvent washing treatment," *Solar Energy Materials and Solar Cells*, vol. 141, pp. 309-314, 2015.

- [41] J. Yang, B. D. Siempelkamp, D. Liu, and T. L. Kelly, "Investigation of CH<sub>3</sub>NH<sub>3</sub>PbI<sub>3</sub> Degradation Rates and Mechanisms in Controlled Humidity Environments Using in Situ Techniques," *ACS nano*, vol. 9, pp. 1955-1963, 2015.
- [42] B. Hailegnaw, S. Kirmayer, E. Edri, G. Hodes, and D. Cahen, "Rain on Methylammonium Lead Iodide Based Perovskites: Possible Environmental Effects of Perovskite Solar Cells," *The Journal of Physical Chemistry Letters*, vol. 6, pp. 1543-1547, 2015.
- [43] K. K. Bass, R. E. McAnally, S. Zhou, P. I. Djurovich, M. E. Thompson, and B. C. Melot, "Influence of moisture on the preparation, crystal structure, and photophysical properties of organohalide perovskites," *Chemical Communications*, vol. 50, pp. 15819-15822, 2014.
- [44] L. K. Ono, S. R. Raga, M. Remeika, A. J. Winchester, A. Gabe, and Y. Qi, "Pinhole-free hole transport layers significantly improve the stability of MAPbI<sub>3</sub>-based perovskite solar cells under operating conditions," *Journal of Materials Chemistry A*, vol. 3, pp. 15451-15456, 2015.
- [45] A. Dymshits, A. Henning, G. Segev, Y. Rosenwaks, and L. Etgar, "The electronic structure of metal oxide/organo metal halide perovskite junctions in perovskite based solar cells," *Scientific reports*, vol. 5, 2015.
- [46] J. Yang, B. D. Siempelkamp, E. Mosconi, F. De Angelis, and T. L. Kelly, "Origin of the Thermal Instability in CH<sub>3</sub>NH<sub>3</sub>PbI<sub>3</sub> Thin Films Deposited on ZnO," *Chemistry of Materials*.
- [47] J. A. Christians, P. A. Miranda Herrera, and P. V. Kamat, "Transformation of the Excited State and Photovoltaic Efficiency of CH<sub>3</sub>NH<sub>3</sub>PbI<sub>3</sub> Perovskite upon

- Controlled Exposure to Humidified Air," *Journal of the American Chemical Society*, vol. 137, pp. 1530-1538, 2015.
- [48] M. K. Siddiki, S. Venkatesan, D. Galipeau, and Q. Qiao, "Kelvin probe force microscopic imaging of the energy barrier and energetically favorable offset of interfaces in double-junction organic solar cells," *ACS applied materials & interfaces*, vol. 5, pp. 1279-1286, 2013.
- [49] A. Dubey, N. Adhikari, S. Venkatesan, S. Gu, D. Khatiwada, Q. Wang, *et al.*, "Solution processed pristine PDPP3T polymer as hole transport layer for efficient perovskite solar cells with slower degradation," *Solar Energy Materials and Solar Cells*, 2015.
- [50] N. Adhikari, A. Dubey, D. Khatiwada, A. F. Mitul, Q. Wang, S. Venkatesan, *et al.*, "Interfacial study to suppress charge carrier recombination for high efficiency Perovskite solar cells," *ACS applied materials & interfaces*, 2015.
- [51] N. Z. Koocher, D. Saldana-Greco, F. Wang, S. Liu, and A. M. Rappe, "Polarization Dependence of Water Adsorption to CH<sub>3</sub>NH<sub>3</sub>PbI<sub>3</sub> (001) Surfaces," *The journal of physical chemistry letters*, vol. 6, pp. 4371-4378, 2015.
- [52] Y. Yuan, J. Chae, Y. Shao, Q. Wang, Z. Xiao, A. Centrone, *et al.*, "Photovoltaic switching mechanism in lateral structure hybrid perovskite solar cells," *Advanced Energy Materials*, vol. 5, 2015.
- [53] G. Niu, X. Guo, and L. Wang, "Review of recent progress in chemical stability of perovskite solar cells," *Journal of Materials Chemistry A*, vol. 3, pp. 8970-8980, 2015.

- [54] A. E. Becquerel, "Recherches sur les effets de la radiation chimique de la lumiere solaire au moyen des courants electriques " *Comptes Rendus de L'Academie des Sciences*, vol. 9, pp. 145-149, 1839.
- [55] D. M. Chapin, C. S. Fuller, and G. L. Pearson, "A new silicon p-n junction photocell for converting solar radiation into electrical power," *Journal of Applied Physics*, vol. 25, p. 676, 1954.
- [56] R. Gereth, "Contribution to Silicon Solar Cell Technology " *Energy Conversion*, vol. 12, pp. 103-107, 1972.
- [57] C. W. Tang, "Two-layer organic photovoltaic cell," *Applied Physics Letters*, vol. 48, pp. 183-185, 1986.
- [58] H. Spanggaard and F. C. Krebs, "A brief history of the development of organic and polymeric photovoltaics," *Solar Energy Materials and Solar Cells*, vol. 83, pp. 125-146, 2004.
- [59] G. Yu, J. Gao, J. C. Hummelen, F. Wudl, and A. J. Heeger, "Polymer photovoltaic cells: enhanced efficiencies via a network of internal donor-acceptor heterojunctions," *Science-AAAS-Weekly Paper Edition*, vol. 270, pp. 1789-1790, 1995.
- [60] S. E. Shaheen, C. J. Brabec, N. S. Sariciftci, F. Padinger, T. Fromherz, and J. C. Hummelen, "2.5% efficient organic plastic solar cells," *Applied Physics Letters*, vol. 78, pp. 841-843, 2001.
- [61] Z. He, C. Zhong, S. Su, M. Xu, H. Wu, and Y. Cao, "Enhanced power-conversion efficiency in polymer solar cells using an inverted device structure," *Nature Photonics*, vol. 6, pp. 591-595, 2012.

- [62] J. You, L. Dou, K. Yoshimura, T. Kato, K. Ohya, T. Moriarty, *et al.*, "A polymer tandem solar cell with 10.6% power conversion efficiency," *Nature communications*, vol. 4, p. 1446, 2013.
- [63] B. O'regan and M. Grätzel, "A low-cost, high-efficiency solar cell based on dye-sensitized," *nature*, vol. 353, pp. 737-740, 1991.
- [64] M. A. Green, A. Ho-Baillie, and H. J. Snaith, "The emergence of perovskite solar cells," *Nature Photonics*, vol. 8, pp. 506-514, 2014.
- [65] M. Liu, M. B. Johnston, and H. J. Snaith, "Efficient planar heterojunction perovskite solar cells by vapour deposition," *Nature*, vol. 501, pp. 395-398, 2013.
- [66] M. M. Lee, J. Teuscher, T. Miyasaka, T. N. Murakami, and H. J. Snaith, "Efficient hybrid solar cells based on meso-superstructured organometal halide perovskites," *Science*, vol. 338, pp. 643-647, 2012.
- [67] A. Mei, X. Li, L. Liu, Z. Ku, T. Liu, Y. Rong, *et al.*, "A hole-conductor-free, fully printable mesoscopic perovskite solar cell with high stability," *Science*, vol. 345, pp. 295-298, 2014.
- [68] H.-S. Kim, C.-R. Lee, J.-H. Im, K.-B. Lee, T. Moehl, A. Marchioro, *et al.*, "Lead iodide perovskite sensitized all-solid-state submicron thin film mesoscopic solar cell with efficiency exceeding 9%," *Scientific reports*, vol. 2, 2012.
- [69] H. Zhou, Q. Chen, G. Li, S. Luo, T.-b. Song, H.-S. Duan, *et al.*, "Interface engineering of highly efficient perovskite solar cells," *Science*, vol. 345, pp. 542-546, 2014.

- [70] W. S. Yang, J. H. Noh, N. J. Jeon, Y. C. Kim, S. Ryu, J. Seo, *et al.*, "High-performance photovoltaic perovskite layers fabricated through intramolecular exchange," *Science*, vol. 348, pp. 1234-1237, 2015-06-12 00:00:00 2015.
- [71] H. J. Snaith, "The perils of solar cell efficiency measurements," *Nat Photon*, vol. 6, pp. 337-340, 06//print 2012.
- [72] J.-J. Li, J.-Y. Ma, Q.-Q. Ge, J.-S. Hu, D. Wang, and L.-J. Wan, "Microscopic Investigation of Grain Boundaries in Organolead Halide Perovskite Solar Cells," *ACS Applied Materials & Interfaces*, vol. 7, pp. 28518-28523, 2015/12/30 2015.
- [73] D. Wang, M. Wright, N. K. Elumalai, and A. Uddin, "Stability of perovskite solar cells," *Solar Energy Materials and Solar Cells*, vol. 147, pp. 255-275, 2016.
- [74] J. Nelson, *The Physics of Solar Cells*. London: Imperial College Press, 2003.
- [75] ElectronicsTutorials. (February 2, 2015). *PN Junction Theory*. Available: [http://www.electronics-tutorials.ws/diode/diode\\_2.html](http://www.electronics-tutorials.ws/diode/diode_2.html)
- [76] S. B. C. Honsberg. (February 3, 2015). *Quantum Efficiency*. Available: <http://pveducation.org/pvcdrom/solar-cell-operation/quantum-efficiency>
- [77] M. I. Ahmed, A. Habib, and S. S. Javaid, "Perovskite Solar Cells: Potentials, Challenges, and Opportunities," *International Journal of Photoenergy*, vol. 2015, p. 13, 2015.
- [78] Y.-C. Hsiao, T. Wu, M. Li, Q. Liu, W. Qin, and B. Hu, "Fundamental Physics behind High-Efficiency Organo-Metal Halide Perovskite Solar Cells," *Journal of Materials Chemistry A*, 2015.
- [79] S. D. Stranks and H. J. Snaith, "Metal-halide perovskites for photovoltaic and light-emitting devices," *Nature nanotechnology*, vol. 10, pp. 391-402, 2015.

- [80] Q. Qiao EE560. Class Lecture Topic, "Sensors and Measurement," *South Dakota State University*, 2013.
- [81] (7-29-2016). *AFM manual*. Available:  
[http://www.charfac.umn.edu/instruments/5500\\_Users\\_Guide.pdf](http://www.charfac.umn.edu/instruments/5500_Users_Guide.pdf)
- [82] L. Kelvin, "V. Contact electricity of metals," *The London, Edinburgh, and Dublin Philosophical Magazine and Journal of Science*, vol. 46, pp. 82-120, 1898.
- [83] W. Melitz, J. Shen, A. C. Kummel, and S. Lee, "Kelvin probe force microscopy and its application," *Surface Science Reports*, vol. 66, pp. 1-27, 2011.
- [84] R. Reifenberger. ME597/PHYS5700. Class Lecture Topic, "Fundamentals of Atomic Force Microscopy," *Purdue University*, 2010.
- [85] (7-29-2016). *Application note on advanced atomic force microscopy*. Available:  
<http://literature.cdn.keysight.com/litweb/pdf/5989-9740EN.pdf>
- [86] S. Sadewasser and T. Glatzel, *Kelvin probe force microscopy*: Springer, 2012.
- [87] S. Venkatesan, N. Adhikari, J. Chen, E. C. Ngo, A. Dubey, D. W. Galipeau, *et al.*, "Interplay of nanoscale domain purity and size on charge transport and recombination dynamics in polymer solar cells," *Nanoscale*, vol. 6, pp. 1011-1019, 2014.
- [88] D. T. Moore, K. W. Tan, H. Sai, K. P. Barteau, U. Wiesner, and L. A. Estroff, "Direct Crystallization Route to Methylammonium Lead Iodide Perovskite from an Ionic Liquid," *Chemistry of Materials*, 2015.
- [89] J. Y. Seto, "The electrical properties of polycrystalline silicon films," *Journal of Applied Physics*, vol. 46, pp. 5247-5254, 1975.

- [90] M. Kumar, A. Dubey, N. Adhikari, S. Venkatesan, and Q. Qiao, "Strategic review of secondary phases, defects and defect-complexes in kesterite CZTS–Se solar cells," *Energy & Environmental Science*, vol. 8, pp. 3134-3159, 2015.
- [91] A. Dubey, P. Saini, and Q. Qiao, "Conjugated Polymers-Based Blends, Composites and Copolymers for Photovoltaics," in *Fundamentals of Conjugated Polymer Blends, Copolymers and Composites*, ed: John Wiley & Sons, Inc., 2015, pp. 281-338.
- [92] S. Venkatesan, E. C. Ngo, Q. Chen, A. Dubey, L. Mohammad, N. Adhikari, *et al.*, "Benzothiadiazole-based polymer for single and double junction solar cells with high open circuit voltage," *Nanoscale*, vol. 6, pp. 7093-7100, 2014.
- [93] J. Gong, H. Qiao, S. Sigdel, H. Elbohy, N. Adhikari, Z. Zhou, *et al.*, "Characteristics of SnO<sub>2</sub> nanofiber/TiO<sub>2</sub> nanoparticle composite for dye-sensitized solar cells," *AIP Advances*, vol. 5, p. 067134, 2015.
- [94] C.-C. Chueh, C.-Y. Liao, F. Zuo, S. T. Williams, P.-W. Liang, and A. K.-Y. Jen, "The roles of alkyl halide additives in enhancing perovskite solar cell performance," *Journal of Materials Chemistry A*, vol. 3, pp. 9058-9062, 2015.
- [95] D. Khatiwada, S. Venkatesan, N. Adhikari, A. Dubey, A. F. Mitul, L. Mohammad, *et al.*, "Efficient Perovskite Solar Cells by Temperature Control in Single and Mixed Halide Precursor Solutions and Films," *The Journal of Physical Chemistry C*, 2015.
- [96] G. Grancini, V. D'Innocenzo, E. Dohner, N. Martino, A. S. Kandada, E. Mosconi, *et al.*, "CH<sub>3</sub>NH<sub>3</sub>PbI<sub>3</sub> perovskite single crystals: surface photophysics and their interaction with the environment," *Chemical Science*, 2015.



- [97] X. Gong, M. Li, X. B. Shi, H. Ma, Z. K. Wang, and L. S. Liao, "Controllable Perovskite Crystallization by Water Additive for High-Performance Solar Cells," *Advanced Functional Materials*, 2015.
- [98] Q. Dong, Y. Yuan, Y. Shao, Y. Fang, Q. Wang, and J. Huang, "Abnormal crystal growth in  $\text{CH}_3\text{NH}_3\text{PbI}_{3-x}\text{Cl}_x$  using a multi-cycle solution coating process," *Energy & Environmental Science*, vol. 8, pp. 2464-2470, 2015.
- [99] X. Song, W. Wang, P. Sun, W. Ma, and Z.-K. Chen, "Additive to regulate the perovskite crystal film growth in planar heterojunction solar cells," *Applied Physics Letters*, vol. 106, p. 033901, 2015.
- [100] D. T. Moore, H. Sai, K. W. Tan, D.-M. Smilgies, W. Zhang, H. J. Snaith, *et al.*, "Crystallization Kinetics of Organic-Inorganic Trihalide Perovskites and the Role of the Lead Anion in Crystal Growth," *Journal of the American Chemical Society*, vol. 137, pp. 2350-2358, 2015.
- [101] C.-G. Wu, C.-H. Chiang, Z.-L. Tseng, M. K. Nazeeruddin, A. Hagfeldt, and M. Grätzel, "High efficiency stable inverted perovskite solar cells without current hysteresis," *Energy & Environmental Science*, vol. 8, pp. 2725-2733, 2015.
- [102] H. Zhang, J. Mao, H. He, D. Zhang, H. L. Zhu, F. Xie, *et al.*, "A Smooth  $\text{CH}_3\text{NH}_3\text{PbI}_3$  Film via a New Approach for Forming the  $\text{PbI}_2$  Nanostructure Together with Strategically High  $\text{CH}_3\text{NH}_3\text{I}$  Concentration for High Efficient Planar-Heterojunction Solar Cells," *Advanced Energy Materials*, 2015.
- [103] J. M. Ball, M. M. Lee, A. Hey, and H. J. Snaith, "Low-temperature processed meso-superstructured to thin-film perovskite solar cells," *Energy & Environmental Science*, vol. 6, pp. 1739-1743, 2013.

- [104] A. F. Mitul, L. Mohammad, S. Venkatesan, N. Adhikari, S. Sigdel, Q. Wang, *et al.*, "Low temperature efficient interconnecting layer for tandem polymer solar cells," *Nano Energy*, vol. 11, pp. 56-63, 2015.
- [105] S. Venkatesan, J. Chen, E. C. Ngo, A. Dubey, D. Khatiwada, C. Zhang, *et al.*, "Critical role of domain crystallinity, domain purity and domain interface sharpness for reduced bimolecular recombination in polymer solar cells," *Nano Energy*, vol. 12, pp. 457-467, 2015.
- [106] P. Adhikary, S. Venkatesan, N. Adhikari, P. P. Maharjan, O. Adebajo, J. Chen, *et al.*, "Enhanced charge transport and photovoltaic performance of PBDTTT-CT/PC 70 BM solar cells via UV–ozone treatment," *Nanoscale*, vol. 5, pp. 10007-10013, 2013.